

ResearchOnline@JCU

This file is part of the following reference:

Walter, Rhys (2015) *Understanding and improving the degradation behaviour of magnesium-based biomaterials.* PhD thesis, James Cook University.

Access to this file is available from:

<http://researchonline.jcu.edu.au/46520/>

The author has certified to JCU that they have made a reasonable effort to gain permission and acknowledge the owner of any third party copyright material included in this document. If you believe that this is not the case, please contact

*ResearchOnline@jcu.edu.au and quote
<http://researchonline.jcu.edu.au/46520/>*

**Understanding and improving the degradation behaviour of
magnesium-based biomaterials**

Thesis submitted

by

Rhys Walter

November 2015

For the degree of Doctor of Philosophy

College of Science, Technology and Engineering

James Cook University, Australia

Acknowledgements

First and foremost, I wish to thank my supervisor, Bobby Mathan. Without your continued support, none of this would be possible. Your unwavering drive to produce only the highest quality work has helped me become the researcher I am today.

I'm also grateful for the support of my co-supervisors, Prof. Yinghe He and Prof. Andrew Sandham. Thank you also to Dr. Carsten Blawert for providing the PEO samples.

Thank you to everyone that has worked in the BEM lab during my time here. I've been fortunate enough to be able to work with a large number of people, but in particular I'd like to thank Raymond Kazum and Alyaa Alabbasi. The lab would be a lonely place without you all.

A huge thank you to all of the JCU academic and support staff that have assisted me over the years. There are far too many to list, but most notably, the school lab manager Ruilan Liu, the academic services officer Melissa Norton, and all of the staff at the AAC. I can't imagine how much more difficult my study would be without the fantastic work everyone here does.

Thank you for all the friends I've been lucky enough to make over the years, for keeping me relatively sane.

Most importantly, thank you to my family. Without your unconditional support and encouragement, none of this would be possible.

Statement on the Contributions from Others

This thesis included the following contributions of others:

Supervisory Team: A/Prof. Bobby Mathan (College of Science, Technology and Engineering, James Cook University)

Prof. Yinghe He (College of Science, Technology and Engineering, James Cook University)

Prof. Andrew Sandham (College of Medicine and Dentistry, James Cook University)

Editorial assistance: Assistance was provided by A/Prof. Bobby Mathan and Katharine J. Fowler.

Experimental assistance: AFM and XRD measurements were conducted by Dr. Shane Askew at the Advanced Analytical Centre (AAC) at James Cook University.

PEO coatings were produced by Dr. Carsten Blawert (Institute of Materials Research, HZG Forschungszentrum Geesthacht GmbH, Geesthacht D21502, Germany).

Abstract

In recent years, there has been a growing interest in the development of biodegradable implants for bone fracture repair. Magnesium (Mg) is a promising candidate for these applications, due to its good biocompatibility, biodegradability and favourable mechanical properties. However, pure Mg degrades too rapidly under physiological conditions. There has been a large amount of research done recently to mitigate the degradation rate of Mg in order to make it a viable biomaterial. This is done primarily through the use of either alloying with other metals, or through a protective coating that degrades at a more favourable rate. To date, there has been limited success in achieving acceptable degradation behaviour through either alloying or coatings. This work was concentrated on two areas: (i) mechanistic understanding of the degradation of Mg-based alloys in physiological conditions, and (ii) utilising partially protective coatings to improve the degradation behaviour of Mg-based alloys. This work culminated in further understanding of the effects of surface roughness and microgalvanic effects of degradation behaviour of Mg alloys, and a novel coating that provided a significantly improved degradation rate for Mg-based alloys.

The influence of surface roughness on the passivation and pitting degradation behaviour of AZ91 Mg alloy in chloride-containing and simulated body fluid (SBF) environments was found to play a critical role on the initial breakdown of the passive layer and the subsequent localised pitting attack. In chloride environment, potentiodynamic polarisation and electrochemical impedance spectroscopy tests suggested that the passivation behaviour of the alloy was affected by increasing the surface roughness. Similarly, in SBF the polarisation resistance (R_p) of the rough surface alloy immersed in SBF for 3 h was ~30% lower as compared to that of the smooth surface alloy. After 12 h immersion in SBF, the R_p values for both the surface finishes decreased and were also similar. However, localised degradation occurred sooner, and to a noticeably higher severity in the rough surface alloy as compared to the smooth surface alloy. Thus the study suggests that the surface roughness plays a critical role in the passivation behaviour of the alloy and hence the pitting tendency.

Microgalvanic effects between the primary matrix and secondary phases are known to influence degradation behaviour. However, there had previously been some concern in

regards to the perceived high stability of secondary precipitates under physiological conditions. This work was able to show that after galvanic coupling between the primary (α) and secondary (β) phases was removed, the long term degradation resistance of the β -phase approached that of pure magnesium. Galvanic coupling of β -phase ($\text{Mg}_{17}\text{Al}_{12}$) with pure Mg in simulated body fluid resulted in the formation of carbonated calcium phosphate on the β -phase. While the calcium phosphate layer initially increased the degradation resistance of the β -phase, the layer rapidly degraded once the galvanic coupling was removed. Within 48 h immersion in SBF, the degradation resistance of the β -phase began to approach that of pure Mg. The results suggest that under long-term immersion period in SBF, the degradation resistance of the β -phase will decrease and eventually the β -phase will dissolve in body fluid as the micro-galvanic effects are reduced due to complete dissolution of the Mg matrix around the β -phase.

This work produced three coatings on Mg-based substrates: a single layer CaP, a dual layer PEO/CaP, and a triple layer PEO/CaP/PLLA. The single layer CaP coating was electrochemically deposited on an Mg-Ca substrate using a pulse potential waveform. EIS testing showed an initial increase in the R_p of ~ 15 times when compared to the bare alloy. Following 72 h immersion in SBF, only ~ 70 % higher than that of the bare alloy. CaPs have a significantly lower dissolution rate than Mg alloys, which suggests that the rapid deterioration of the coating was instead caused by penetration of the electrolyte through the CaP layer. Open circuit potential measurements showed a constant ~ 100 mV difference between the coated and uncoated samples across the entire immersion period, which suggests that the coating remained largely unchanged. This work also investigated whether the cathodic activity of the underlying Mg alloy substrate plays a significant role on the electrochemical deposition of such a coating, calcium phosphate (CaP). CaP was deposited electrochemically on two Mg alloys, i.e., magnesium-calcium (Mg-Ca) and magnesium-aluminium-zinc (AZ91), with different electrochemical degradation behaviour. The in vitro degradation behaviour of the CaP coated samples was evaluated using electrochemical impedance spectroscopy (EIS) in SBF. The R_p of the CaP coated Mg-Ca alloy was ~ 85 % lower than that of the CaP coated AZ91 alloy. Fourier transform infrared (FTIR) analysis showed no difference in the chemical nature of the coatings. However, scanning electron microscopy (SEM) analysis revealed that the coating particles on Mg-Ca alloy were less densely packed

than that on the AZ91 alloy. This can be attributed to the higher dissolution rate of Mg-Ca alloy as compared to AZ91 alloy. As a result, the former exhibited higher cathodic charge density which produced higher hydrogen evolution, and thereby affecting the coating process.

In order to reduce the rate of penetration of electrolyte through the coating layer, a dual layer coating was employed. A porous PEO layer first produced on pure Mg as the first layer. This PEO layer acted as a scaffold for previously discussed CaP layer. This dual layer coating produced a much more tightly packed layer that showed a much higher degradation resistance than either layer did separately. The single PEO layer improved the R_p of the pure Mg by an order of magnitude, and the addition of the second CaP layer added another order of magnitude. This improvement can be attributed to the PEO layer acting as a scaffold for the CaP, allowing for a more tightly packed structure and thereby reducing the porosity. A third, PLLA layer was then added to further improve the pore resistance of the coating. The PLLA layer was able to improve the R_p by a third order of magnitude for low immersion times. Interestingly, by 72 h immersion, the triple layer coating displayed an average R_p lower than that of the dual layer. During the immersion period, the electrolyte was able to penetrate the highly porous polymer layer, allowing for the bulk erosion to take place. The subsequent release of the acidic products damaged the underlying ceramic layer, which reduced the overall degradation resistance.

List of Publications

Walter, R. & Kannan, M. B. Influence of surface roughness on the corrosion behaviour of magnesium alloy, *Materials & Design*, 2011, 32, 2350-2354

Walter, R.; Kannan, M. B.; He, Y. & Sandham, A. Effect of surface roughness on the in vitro degradation behaviour of a biodegradable magnesium-based alloy, *Applied Surface Science*, 2013, 279, 343-348.

Walter, R. & Kannan, M. B. A mechanistic in vitro study of the microgalvanic degradation of secondary phase particles in magnesium alloys *Journal of Biomedical Materials Research Part A*, 2015, 103, 990-1000.

Walter, R.; Kannan, M. B.; He, Y. & Sandham, A. Influence of the cathodic activity of magnesium alloys on the electrochemical deposition of calcium phosphate, *Applied Surface Science*, 2014, *Materials Letters*, 130, 184-187.

Kannan, M. B.; Walter, R.; Yamamoto, A. Biocompatibility and in vitro degradation behaviour of magnesium-calcium alloy coated with calcium phosphate using an unconventional electrolyte. Article under review, *ACS Biomaterials Science & Engineering*.

Kannan, M. B.; Walter, R.; Yamamoto, A.; Blawert, C. Biocompatibility and in vitro degradation behaviour of dual layer PEO/CaP coating on a magnesium substrate. (Article in preparation).

Walter, R.; Kannan, M. B.; Blawert, C. Controlling the in vitro degradation of magnesium using a novel multilayer coating. (Article in preparation).

Table of Contents

Acknowledgements	i
Statement on the Contributions from Others	ii
Abstract	iii
List of Publications	vi
Table of Contents	vii
List of Tables	x
List of Figures	xi
List of Plates	xiv
List of Symbols	xv
Chapter. 1 Introduction	1
1.1 Background and Rational	1
1.2 Research Objectives	3
1.2 Document Organisation and Publications	3
Chapter. 2 Literature Review	6
2.1 Introduction	6
2.2 Fundamentals of Mg Degradation	8
2.2.1 Degradation Mechanism.....	8
2.2.2 Environmental Influences.....	9
2.3 Material Effects	10
2.3.1 Alloying.....	10
2.3.2 Secondary Phases and Microgalvanic Degradation	13
2.4 Biodegradable Coatings	16
2.4.1 Calcium phosphate (CaP)	17
2.4.2 Plasma Electrolytic Oxidation (PEO).....	22

2.4.3	Organic Polymer Coatings	27
Chapter. 3	Materials and Methodology	32
3.1	Introduction	32
3.2	In-vitro Degradation and Electrochemical Degradation Techniques.....	32
3.2.1	Potentiodynamic Polarisation.....	35
3.2.2	Electrochemical Impedance Spectroscopy (EIS)	35
3.2.3	Galvanic coupling.....	38
3.3	Materials Characterisation	39
3.4	Coatings.....	40
Chapter. 4	Influence of Surface Roughness on the Degradation and Passivation Behaviour of Mg Alloys.....	41
4.1	Introduction	41
4.2	Materials and Methods	42
4.3	Results and Discussion	42
4.3.1	Influence of surface roughness in 3.5 % NaCl.....	42
4.3.2	Influence of surface roughness in SBF.....	49
4.4	Conclusions	57
Chapter. 5	A Mechanistic in Vitro Study of the Micro- galvanic Degradation of Secondary Phase Particles in Mg Alloys	58
5.1	Introduction	58
5.2	Materials and Methods	58
5.3	Results.....	59
5.4	Discussion	69
5.5	Conclusions	74
Chapter. 6	Multilayer Coatings on pure Mg	75
6.1	Introduction	75

6.2	Materials and Methods	76
6.3	Results and Discussion	77
6.3.1	Single layer CaP coating	77
6.3.2	Dual Layer PEO/CaP coating	90
6.3.3	Triple layer PEO/CaP/PLLA coating	96
6.4	Conclusions	102
Chapter. 7 Conclusions and Recommendations		104
7.1	Outcomes	104
7.1.1	Influence of surface roughness	104
7.1.2	Influence of the microgalvanic effect	104
7.1.3	Degradation behavior of single layer CaP coatings	105
7.1.4	Influence of the cathodic activity of Mg alloys on the electrochemical deposition of calcium phosphate	105
7.1.5	Degradation behaviour of multilayer coatings on Mg.....	105
7.2	Recommendations for Future Work	106
References		107

List of Tables

<i>Table 2.1 Physical and mechanical properties of natural bone, Mg and other implant materials (Staiger et al., 2006).</i>	7
<i>Table 2.2 Solubility limits of the most commonly used alloying elements in Mg (Chen et al., 2014).</i>	10
<i>Table 2.3 In vitro and in vivo studies of Mg alloys and their secondary particles.</i>	15
<i>Table 2.4 Typical corrosion potentials for Mg and common secondary phases in 5 % NaCl (Song and Atrens, 2003).</i>	16
<i>Table 2.5 Common CaP phases used for coating orthopaedic devices (Shadanbaz and Dias, 2012).</i>	17
<i>Table 2.6 Examples of PEO coatings on Mg alloys.</i>	25
<i>Table 2.7 Polymer abbreviations (Middleton and Tipton, 2000).</i>	27
<i>Table 2.8 Commercial polymer biodegradable devices (Middleton and Tipton, 2000).</i>	28
<i>Table 3.1 Composition of the SBF (Oyane, 2003).</i>	34
<i>Table 4.1 Chemical composition (wt. %) of the AZ91 alloy tested in 3.5 % w/v NaCl.</i>	42
<i>Table 4.2 Surface roughness (Sa) of AZ91 Mg alloy with different surface finish (N=3).</i>	43
<i>Table 4.3 Electrochemical degradation parameters of AZ91 alloy (with different surface roughness) obtained from potentiodynamic polarisation curves (N=3).</i>	46
<i>Table 4.4 Surface roughness (Sa) data for AZ91 Mg alloy (N=3).</i>	50
<i>Table 5.1 Chemical composition (wt. %) of pure Mg and β-precipitate.</i>	59
<i>Table 6.2 Modelling data from the EIS plots of bare alloy and CaP coated alloy (N=2).</i>	82
<i>Table 6.3 Electrochemical degradation parameters of Mg and its alloys obtained from potentiodynamic polarisation curves (N=2).</i>	93

List of Figures

<i>Figure 3.1 Outline of the methods used to fully describe degradation behaviour.</i>	33
<i>Figure 3.2 Experimental setup of the electrochemical degradation techniques.</i>	34
<i>Figure 3.3 Ideal Potentiodynamic polarisation curve with marked points of importance.</i>	35
<i>Figure 3.4 Typical Nyquist plot.</i>	37
<i>Figure 3.5 Typical Bode plot.</i>	37
<i>Figure 3.3 Experimental setup of the galvanic coupling.</i>	39
<i>Figure 4.1 Surface topography of AZ91 Mg alloy ground/polished up to (a) 320 grit SiC; (b) 600 grit SiC; (c) 1200 grit SiC; and (d) 3μm diamond paste.</i>	43
<i>Figure 4.2 Nyquist plots of AZ91 Mg alloy, with different surface roughness, tested in 0.5 wt. % NaCl.</i>	45
<i>Figure 4.3 Potentiodynamic polarisation curves of AZ91 alloy, with different surface roughness, tested in 0.5 wt. % NaCl.</i>	46
<i>Figure 4.4 AFM images of AZ91 Mg alloy under two different surface finishes: (a) ground with 120 grit SiC paper, and (b) polished with 3 μm diamond paste.</i>	50
<i>Figure 4.5 EIS plots for AZ91 Mg alloy immersed in SBF for varied immersion times.</i>	51
<i>Figure 4.6 Polarisation resistance vs. time for AZ91 Mg alloy immersed in SBF, and the applied equivalent circuit model.</i>	52
<i>Figure 4.7 Phenomenological model of the localised degradation behaviour of a rough surface and a smooth surface of AZ91 Mg alloy.</i>	56
<i>Figure 5.1 XRD pattern of the Mg₁₇Al₁₂ (β-phase).</i>	59
<i>Figure 5.2 Nyquist and Bode plots of the pure Mg and β-phase immersed in SBF for (a) 2 h, (b) 4 h, (c) 8 h and (d) 24 h.</i>	61
<i>Figure 5.3 Polarisation resistance (R_p) vs. time for the pure Mg and β-phase ($N=3$).</i> ..	62
<i>Figure 5.4 (a) Mixed potential of the pure Mg and β-phase during the galvanic coupling and (b) current vs. time during the galvanic coupling.</i>	63
<i>Figure 5.5 FTIR spectrum of the coating deposited on the β-phase.</i>	64
<i>Figure 5.6 XRD pattern of the coating deposited on the β-phase.</i>	64

<i>Figure 5.7 Open circuit potential (OCP) for the pure Mg and β-phase during immersion in SBF (a) prior to galvanic coupling and (b) following galvanic coupling.</i>	66
<i>Figure 5.8 Post-coupled Nyquist and Bode plots of the pure Mg and β-phase immersed in SBF for (a) 2 h, (b) 12 h, (c) 24 h and (d) 48 h.</i>	67
<i>Figure 5.9 Post-coupled R_P vs. time for the pure Mg and β-phase ($N=3$).</i>	68
<i>Figure 5.10 Phenomenological model describing the micro-galvanic effects in an Mg alloy.</i>	72
<i>Figure 6.1 (a) FTIR and (b) XRD spectra of the CaP coating on Mg-Ca alloy.</i>	77
<i>Figure 6.2 Potentiodynamic polarisation curves for the bare alloy and CaP coated Mg-Ca alloy in SBF.</i>	78
<i>Figure 6.3 EIS plots for: (a) bare alloy, and (b) CaP coated Mg-Ca alloy over the 72 h immersion period in SBF.</i>	80
<i>Figure 6.4 Polarisation resistance (R_P) vs. time from EIS data of bare alloy and CaP coated Mg-Ca alloy in SBF ($N=2$).</i>	81
<i>Figure 6.5 Open-circuit potential (OCP) measurements of the bare alloy and CaP coated Mg-Ca alloy during immersion in SBF.</i>	81
<i>Figure 6.6 (a) FTIR and (b) XRD spectra of the CaP coated Mg-Ca alloy following 72 h immersion in SBF.</i>	83
<i>Figure 6.7 FTIR spectra of the calcium phosphate coating on Mg-Ca and AZ91 alloys.</i>	86
<i>Figure 6.8 EIS plots of: (a) bare metals and (b) CaP coated metals; and (c) polarisation resistance (R_P) from EIS modelling ($N=2$).</i>	88
<i>Figure 6.9 Cathodic current density recorded during the calcium phosphate coating on (a) Mg-Ca alloy, and (b) AZ91 alloy; and (c) average charge density for both the alloys during the coating process ($N=2$).</i>	89
<i>Figure 6.10 FTIR spectra of the PEO and PEO/CaP dual layers.</i>	91
<i>Figure 6.11 Potentiodynamic polarisation curves for bare Mg, PEO and PEO/CaP dual layer coatings.</i>	93
<i>Figure 6.12 EIS plots over a 72 h immersion period in SBF for (a) PEO and (b) PEO/CaP dual layer coatings.</i>	94
<i>Figure 6.13 R_P vs. Time for bare Mg, PEO and PEO/CaP dual layers over a 72 h immersion period in SBF ($N=2$).</i>	94
<i>Figure 6.14 FTIR spectra of the PEO and PEO/CaP dual layers following 72 h immersion in SBF.</i>	95

Figure 6.15 Potentiodynamic polarisation curves for bare Mg, PEO, PEO/CaP dual layer, and triple layer hybrid coatings. 98

Figure 6.16 EIS plots over a 72 h immersion period in SBF for the triple layer hybrid coatings..... 100

Figure 6.17 R_P vs. Time for bare Mg, PEO, PEO/CaP dual layer, and triple layer hybrid coatings over a 72 h immersion period in SBF (=2). 100

List of Plates

<i>Plate 4.1 SEM images of AZ91 Mg alloy ground/polished (for different surface roughness) up to (a) 320 grit SiC; (b) 600 grit SiC; (c) 1200 grit SiC; and (d) 3μm diamond-paste, and immersed in 0.5 wt. % NaCl for 24 h.</i>	<i>48</i>
<i>Plate 4.2 SEM images of AZ91 Mg alloy ground/polished up to (a) 320 grit SiC; (b) 600 grit SiC; (c) 1200 grit SiC; and (d) 3μm diamond-paste, after galvanostatic testing.</i>	<i>48</i>
<i>Plate 4.3 SEM images of the AZ91 Mg alloy immersed in SBF for 2, 6 and 12 hours. .</i>	<i>53</i>
<i>Plate 5.1 SEM images after 24 h immersion in SBF for (a, b) pure Mg and (c, d) β-phase.</i>	<i>62</i>
<i>Plate 5.2 SEM images of the coating after 4 h galvanic coupling in SBF at (a) low magnification, showing pores and (b) high magnification showing particles.</i>	<i>65</i>
<i>Plate 5.3 SEM images of the coating after 4 h immersion in SBF, (a) showing calcium phosphate coating degradation, and (b) the same sample with the remaining calcium phosphate particles removed.</i>	<i>68</i>
<i>Plate 6.1 SEM images of the CaP coating on Mg-Ca alloy: (a) low magnification shows complete coverage of the base material, and (b) high magnification shows large, flat and irregularly oriented particles.</i>	<i>77</i>
<i>Plate 6.2 SEM images of: (a, b) CaP coated alloy, and (c, d) bare Mg-Ca alloy following 72 h immersion in SBF.</i>	<i>84</i>
<i>Plate 6.3 SEM images of the calcium phosphate coating on: (a, b) Mg-Ca alloy, and (c, d) AZ91 alloy.</i>	<i>86</i>
<i>Plate 6.4 SEM images of the (a, b) PEO and (c, d) PEO/CaP dual layers.</i>	<i>92</i>
<i>Plate 6.5 SEM images of the (a, b) PEO and (c, d) PEO/CaP dual layers following 72 h immersion in SBF.</i>	<i>96</i>
<i>Plate 6.6 SEM images of the triple layer hybrid coatings.</i>	<i>98</i>
<i>Plate 6.7 SEM images of the triple layer hybrid coatings following 72 h immersion in SBF.</i>	<i>101</i>

List of Symbols

AFM	=	Atomic force microscopy
CaP	=	Calcium Phosphate
C_f, C_{dl}	=	Film capacitance, double layer capacitance
E_{corr}	=	Corrosion potential
EIS	=	Electrochemical impedance spectroscopy
FTIR	=	Fourier transform infrared spectroscopy
i_{corr}	=	Corrosion current density
OCP	=	Open circuit potential
PEO	=	Plasma electrolytic oxidation
PLLA	=	Poly (L-lactic acid)
R_s, R_f, R_{ct}	=	Resistance due to solution, film and charge transfer
R_p	=	Polarisation resistance
SBF	=	Simulated body fluid
SEM	=	Scanning electron microscope
SiC	=	Silicon-carbide
Wt. %	=	Weight in percentage
XRD	=	X-ray diffraction
$ Z $	=	Absolute impedance
Z'	=	Real impedance
Z''	=	Imaginary impedance
α	=	Primary matrix of an Mg alloy
β	=	Mg ₁₇ Al ₁₂ secondary phase of AZ91 Mg alloy
ρ	=	Density of the metal in g/cm ³
φ	=	Phase shift between current and potential

Chapter. 1 Introduction

1.1 Background and Rational

Biomedical implants are used by surgeons in order to replace or support damaged biological structures. These implants can be roughly divided into two categories: The first is permanent implants, where the implant is required to perform its function indefinitely, such as full hip replacements. The second, is temporary implants. These implants are typically used for bone fracture repair, and remain inert in the body, but are no longer required once the bone is fully healed. These implants are designed to rigidly hold bone in place during the healing process. A subset of temporary implants are biodegradable implants, such as sutures, which are designed to degrade naturally over time. Biodegradable materials have typically been limited to polymeric materials. These polymers, such as polylactide, polyglycolide and their copolymers are both biocompatible and biodegradable. Unfortunately, their mechanical properties are quite poor as you can see, which limits their use to non-load bearing applications, such as sutures, maxilla fractures and paediatric mandibular fractures.

Non-biodegradable implants for bone fracture repair are primarily metallic; stainless steel, chromium/cobalt alloys and most commonly, titanium. However, the mechanical properties of these materials are not well matched with those of bone. In particular, the elastic modulus of these materials is significantly higher than that of bone. This can cause an effect known as stress shielding. Stress shielding is a phenomenon that occurs due to the fact that bone is constantly being resorbed and regrown. The rate at which this occurs is proportional to the load that that bone undergoes. So if the majority of the load is being borne by the implant due to its high elastic modulus, the bone will grow back significantly weaker and more porous, increasing the likelihood of refracture. In addition to this, the implants increase the likelihood of complications due to foreign body reactions and infections caused by long term exposure. Often, surgeons have to do a secondary surgery to remove the implant if such a complication does arise. This secondary surgery is highly undesirable due to additional costs and increased risks associated with extra surgery.

A promising candidate for biodegradable implants is Mg based biomaterials. Like the polymeric materials, it is both biocompatible and biodegradable. In fact, Mg is one of the most common ions in the human body, and due to the efficient excretion of the degradation products, cases of hyper-Mg are almost non-existent. Furthermore its mechanical properties are more closely matched to that of bone. This considerably reduces the major issues of both stress shielding and the need for secondary surgery.

However, there are currently some limitations that inhibit the use of Mg as a biodegradable material. Firstly, pure Mg degrades too rapidly under physiological conditions. The degradation rate of approximately 22mm/year means that pure Mg would degrade far too rapidly to maintain mechanical integrity over the required implant service life. This rapid degradation would also cause issues with hydrogen gas build up in the body, which evolves too rapidly to be removed from the implant site.

There are two main ways that the degradation rate can be reduced. The first is via the use of alloying elements. There has been a large amount of research done into alloying Mg in order to improve the degradation resistance. The main alloying elements are aluminium, rare earths and calcium, which have all been shown to improve this property. Unfortunately, Mg alloys are particularly susceptible to localised attack. This is a form of degradation that heavily attacks particular sites on the alloy. This is even more of a concern than general degradation, since the pits that form create act as stress risers which allow the propagation of cracks due to stress corrosion cracking and hydrogen embrittlement. This could potentially cause the implant to fail prematurely. This thesis investigated two areas that hadn't been studied, namely the influence of surface roughness and microgalvanic effects on the localised degradation of Mg alloys.

The second method of improving degradation rates is to apply a partially protective coating to the Mg surface. The coating acts as a barrier to the substrate, such that the favourable mechanical properties are retained, but the degradation rate can be slowed to that of the coating. There has been a wide range of coatings utilised for this purpose, but to date none have been able to provide suitable long term resistance for implant applications. This work produced a novel, multilayer coating that showed good *in vitro* degradation behaviour.

1.2 Research Objectives

This work aimed to improve the understanding relating to *in vitro* Mg degradation in order to eventually produce Mg-based biodegradable biomaterials for bone fracture repair. To do this, the following research aims were developed:

- (1) To understand how surface roughness is related to localised pitting attack of Mg alloys under chloride-containing and physiological conditions.
- (2) Understanding of the role of microgalvanic degradation on the overall *in vitro* degradation behaviour of Mg alloys.
- (3) To identify whether substrate composition contributes significantly on the overall degradation behaviour of a coated Mg alloy.
- (4) To improve the *in vitro* degradation behaviour of Mg by developing a partially protective, tailorable coating that is suitable for temporary implant applications.

Achieving these research goals has contributed directly to the field of Mg based biodegradable implants.

1.2 Document Organisation and Publications

This thesis is comprised of seven chapters, which address the background and work related to the research objectives outlined in the previous section. This chapter outlines the motivations and context surrounding the work approached in this thesis.

Chapter 2 provides a current review of the literature related to the work in the body of the thesis. It primarily focusses on the use of Mg as a biomaterial, as well as its degradation behaviour and previous attempts to improve this behaviour. In particular, it outlines the work necessary for a complete understanding of the body of the work outlined in the subsequent chapters.

Chapter 3 presents the methodology utilised in order to achieve the research objectives. It provides the details required to replicate any experimental data, as well as the fundamentals behind interpretation of the results.

Chapter 4 investigates how surface roughness influences Mg degradation in both pure chloride solution and under simulated body conditions. This work is reported in the following journals:

- *Walter, R. & Kannan, M. B. Influence of surface roughness on the corrosion behaviour of magnesium alloy, Materials & Design, 2011, 32, 2350-2354*
- *Walter, R.; Kannan, M. B.; He, Y. & Sandham, A. Effect of surface roughness on the in vitro degradation behaviour of a biodegradable magnesium-based alloy, Applied Surface Science, 2013, 279, 343-348.*

Chapter 5 is a study on the significance of the microgalvanic effect on the degradation of secondary particles in Mg alloys. This work has been published in the following journal:

- *Walter, R. & Kannan, M. B. A mechanistic in vitro study of the microgalvanic degradation of secondary phase particles in magnesium alloys Journal of Biomedical Materials Research Part A, 2015, 103, 990-1000.*

Chapter 6 presents the research done to develop a partially protective coating to improve the degradation behaviour of Mg substrates. It also looks at the influence of the substrate composition on coating performance. The results in this chapter are reported in a number of papers:

- *Walter, R.; Kannan, M. B.; He, Y. & Sandham, A. Influence of the cathodic activity of magnesium alloys on the electrochemical deposition of calcium phosphate, Applied Surface Science, 2014, Materials Letters, 130, 184-187.*

This work was also presented as a poster at the 5th International Symposium of Surface and Interface of Biomaterials (ISSIB) held in conjunction with the 24th Annual Conference of the Australasian Society for Biomaterials and Tissue Engineering (ASBTE).

The following papers are currently in preparation:

- *Kannan, M. B.; Walter, R.; Yamamoto, A. Biocompatibility and in vitro degradation behaviour of magnesium-calcium alloy coated with calcium phosphate using an unconventional electrolyte. Article under review, ACS Biomaterials Science & Engineering.*
- *Kannan, M. B.; Walter, R.; Yamamoto, A.; Blawert, C. Biocompatibility and in vitro degradation behaviour of dual layer PEO/CaP coating on a magnesium substrate. (Article in preparation).*
- *Walter, R.; Kannan, M. B.; Blawert, C. Controlling the in vitro degradation of magnesium using a novel multilayer coating. (Article in preparation).*

Chapter 7 presents the concluding remarks of the thesis, as well as recommendations of possible research direction for future work. The key findings of Chapters 4-6 are summarised in this section.

Chapter. 2 Literature Review

2.1 Introduction

Metallic materials have played an essential role as biomaterials in the orthopaedic field to replace or repair damaged bone tissue. Traditionally, inert materials such as stainless steel, titanium and chromium-cobalt alloys have been used over ceramic and polymeric materials in load bearing applications due to their high mechanical strength and fracture toughness (Staiger et al., 2006). However, these permanent implants have two major limitations. Firstly, degradation and wear can sometimes lead to the release of toxic metallic ions and particles (Jacobs et al., 1998; Jacobs et al., 2003), resulting in inflammation and tissue loss (Wang et al., 1996; Bi et al., 2001; Niki et al., 2003). In severe cases, a secondary surgery is required to remove the implant, increasing the risk of patient morbidity and potentially resulting in re-fracture due to voids in the bone at the implant site. Secondly, the elastic moduli of these materials are not well matched with that of natural bone resulting in stress shielding effects. This leads to reduced bone regrowth and remodelling, decreasing implant stability (Nagels et al., 2003).

Mg is an attractive potential biomaterial to replace current temporary implants. It is exceptionally lightweight, and has a high strength to weight ratio. It has a higher fracture toughness than ceramic materials such as hydroxyapatite, but maintains an elastic modulus much closer to natural bone than other currently used metals, considerably reducing stress shielding effects. Table 2.1 compares the key mechanical properties of natural bone, Mg and commonly used implant materials. Furthermore, Mg degrades naturally under physiological conditions, and has been shown to be highly biocompatible. Mg is required for a large number of physiological processes (Saris et al., 2000; Hartwig, 2001; Okuma, 2001; Vormann, 2003), and there is evidence to suggest that ionic Mg can accelerate bone growth. While hyper-Mg occurs at concentrations in excess of 1.05 mmol/L (Saris et al., 2000), cases are rare since it is excreted efficiently through the urine (Saris et al., 2000; Vormann, 2003).

However, the degradation rate of pure Mg in the body is too high to be suitable for implant applications (Witte, et al., 2008). To combat this, many researchers have attempted to improve the degradation resistance through alloying and the application of

partially protective coatings to produce a material that can maintain structural integrity over the expected lifetime of the implant.

Table 2.1
Physical and mechanical properties of natural bone, Mg and other implant materials (Staiger et al., 2006).

Material	Density (g/cm³)	Elastic modulus (GPa)	Compressive yield strength (MPa)	Fracture toughness (MPa.m^{1/2})
Natural bone	1.8-2.1	3-20	130-180	3-6
Mg	1.74-2.0	41-45	65-100	15-40
Ti alloys	4.4-4.5	110-117	758-1117	55-115
Co-Cr alloys	8.3-9.2	230	450-1000	N/A
Stainless steel	7.9-8.1	189-205	170-310	50-200
Hydroxyapatite	3.1	73-117	600	0.7

The first use of Mg-based biomaterials for orthopaedic use was in 1900 to improve joint motion (Staiger et al., 2006). Soon after, Lambotte implemented a pure Mg plate with gold plated nails to stabilise a lower leg fracture (Staiger et al., 2006). The implant was reported to have dissolved after on 8 days *in vivo*, and produced a large amount of hydrogen gas around the implant site. While there were a number of other studies that utilised Mg-based biomaterials, the rapid degradation rate paired with high amounts of hydrogen evolution was a consistent limitation of the materials (Witte, 2010). Recently, Mg has regained interest as a potential biodegradable biomaterial, and there has been a large amount of work done to eliminate the problems associated with its high rate of degradation.

This chapter provides an overview of the current literature relevant to this work. The scope of this thesis covered two distinct sections: the effects of certain properties of bare Mg, as well as the development of an effective coating. The following sections provide information relevant to the upcoming chapters. Although the degradation of Mg is heavily influenced by a large number of parameters, in this thesis, all experiments were run under physiological conditions (37 °C, pH 7.40, physiological

ion concentrations). As such, the effects of temperature, pH, and electrolyte composition will not be discussed in depth. The fundamentals of Mg degradation are provided for context, describing the general mechanisms as well as an examination of dominant influencing factors. Following this, an overview the current state of partially protective coatings is presented, with a particular focus on coatings similar to those presented in this work.

2.2 Fundamentals of Mg Degradation

2.2.1 Degradation Mechanism

The degradation mechanism of Mg in an aqueous environment is shown in the following reactions:



The production of the OH⁻ causes a pH increase, favouring the production of a passive hydroxide film, as shown in the following reaction:



This passive film has low solubility in aqueous environments, causing the pH of the solution to rise to ~10.5 in only a few hours of immersion (Atrens et al., 2015). During the degradation of most metals in acidic solutions, an increase in potential results in an increase in the anodic dissolution and a decrease in the cathodic hydrogen evolution. However, during the degradation of Mg, an increase in applied potential results in a hydrogen evolution increase along with higher anodic dissolution. This phenomenon is known as the negative difference effect (NDE). Researchers have attempted to explain this unusual behaviour through a number of mechanisms. Most recently, Song and Atrens (Song and Atrens, 1999) proposed that increasing applied potential results in an increase in the area free of surface film. In these areas, the anodic and cathodic partial reactions are able to occur more freely than on areas covered with surface film. As the

potential increases above the pitting potential, reaction 3 proceeds more rapidly due to the increased concentration of the available univalent Mg ions.

In cases where Cl^- concentration exceeds 30 mmol/L (physiological environment is ~ 150 mmol/L), the passive film produced in reaction 5 rapidly converts to the highly soluble MgCl_2 (Gu et al., 2014). This can be seen via the following reaction (Staiger et al., 2006):



As a result of the presence of the partially protective film, Mg tends to exhibit localised degradation, rather than general degradation. In fact, it is not uncommon for areas to remain unattacked after 24 h immersion in 3.5 % NaCl (Atrens et al., 2015). Localised degradation typically occurs via the formation of shallow pits at discrete sites, which then expand to cover the whole surface over time. As shown in reaction 2.5, the passive film is not very stable, and the free corrosion potential is higher than the pitting potential for both single and multi-phase Mg alloys. Unlike steels, the pitting behaviour of Mg spreads laterally, and has a low tendency toward the formation of deep pits. The reason for this is that the by-product of the cathodic reaction is the formation of OH^- ions, which result in a localised pH increase, as previously discussed. This allows for the stabilisation of the local passive film, and thus it can be said that the localised degradation of Mg is self-limiting (Atrens et al., 2015). However, while these pits are relatively shallow, they can over time link up and cause undermining.

2.2.2 *Environmental Influences*

The degradation rate of pure Mg is typically constant, apart from a transient period at low immersion times. Qiao et al. concluded a rate of 0.3 - 0.5 mm/yr for degradation of high purity Mg in 3.5 % NaCl solution (Qiao et al., 2012). However, the degradation behaviour is heavily influenced by a large number of parameters, including the electrolyte composition. In particular, the chloride composition plays a role on the rate of degradation. Ambat et al. (Ambat et al., 2000) reported that the degradation rate increased with increasing chloride ion concentration across all pH values. This is primarily due to the role of chloride on the passive layer breakdown as shown in reaction 6. Nakatsugawa et al. (Nakatsugawa et al., 2003) studied the degradation of

thixomoulded AZ91D alloy, and reported that the critical concentration of Cl^- was approximately 10 mol/m^3 , below which the degradation rate was relatively constant.

2.3 Material Effects

2.3.1 Alloying

Extensive research has been done on the selection of alloying elements, either to improve the degradation resistance or to improve mechanical or biological properties. Table 2.2 shows the solubility limits of the most common alloying elements in Mg. Initially, most of the alloys that were considered for biodegradable implant materials were alloys that had originally been developed for other commercial applications. While many alloying elements can improve the degradation resistance and/or mechanical properties, careful selection is required to produce an alloy that has minimal harmful effects on the body as metallic ions are released. The following sections describe the influences of common alloying elements on Mg, and their respective biocompatibility.

Table 2.2
Solubility limits of the most commonly used alloying elements in Mg (Chen et al., 2014).

Element	Solubility Limit (wt. %)	Element	Solubility Limit (wt. %)
Er	33.8	Zr	3.8
Gd	23.49	Mn	2.2
Sn	14.5	Ca	1.34
Al	12.70	Ce	0.74
Y	12.4	La	0.23
Zn	6.2	Sr	0.11
Nd	3.6	Si	~0

2.3.1.1 Influence of Aluminium

Aluminium (Al) is the most commonly used alloying element for modification of mechanical and degradation resistant properties. The addition of Al in the order of 1-5 % results in a significant refinement of grain size, with further additions having no effect (Lee et al., 2000). A small amount of the Al is dissolved in the primary α matrix, with the rest precipitating out as a secondary β phase of $Mg_{17}Al_{12}$ along the grain boundaries or a eutectic region along the dendrite boundaries. This takes the form of either a semi continuous network (Zhang et al., 2006) or lamellar growth (Nam et al., 2011). Higher concentrations of Al lead to a more continuous network of $Mg_{17}Al_{12}$. The influence of Al addition on the degradation resistance is related to the ratio of the primary to secondary phases. Higher volume fractions of the β phase result in improved degradation resistance, due to a more resistant passive layer forming across the surface, due to the continuous networks allowing for even distribution of the protective barrier. Conversely, lower volume fractions can lead to accelerated degradation due to galvanic coupling between the primary matrix and secondary $Mg_{17}Al_{12}$ phases.

While Al based alloys have shown a good improvement in degradation resistance, research on biodegradable Mg alloys has shifted away from Al containing alloys, due to concerns that Al is a risk for the development of Alzheimer's and other neurological diseases (Berthon, 2002).

2.3.1.2 Influence of Rare Earths

The rare earth elements (REs) refer to the fifteen lanthanides, as well as scandium and yttrium. The most commonly alloyed elements with Mg from this group are Cerium (Ce), Erbium (Er), Gadolinium (Gd), Lanthanum (La), Neodymium (Nd) and Yttrium (Y). REs were originally used to improve the creep resistance of Mg (Sanchez et al., 1996), but have also demonstrated improved degradation resistance through grain refinement and the formation of secondary phases (Kannan et al., 2008; Chang et al., 2008; Gu et al., 2010a).

Walter and Kannan (Walter and Kannan, 2011) studied WE54 (1.58 Nd, 4.85 Y, 0.28 Zr, 0.08 Ce, 0.13 Gd, 0.16 Er, 0.13 Yb) alloy in SBF, and reported a marginal increase in the degradation resistance when compared to pure Mg, although the resistance was still inferior to that of AZ91. Conversely, WE43 has been reported to show improved

degradation resistance in 3.5 % NaCl (Arrabal et al., 2008) and 1M NaCl (Zucchi et al., 2006), even higher than AZ91 for longer immersion times. Interestingly, Rosalbino et al. (Rosalbino et al., 2005; Rosalbino et al., 2006) suggested that the addition of Er can have a synergistic effect with Al by producing $Mg_{95}Al_3Er_2$ and $Mg_{95}Al_2Er_3$, which inhibit degradation through enhanced passivation. Similarly, Mg-Al-Ce alloys show good degradation resistance since the $Al_{11}Ce_3$ phase around the grain boundaries can reduce microgalvanic effects (Liu et al., 2009). However, it is important to note that it can be difficult and costly to purify a specific rare earth, there are very few studies on binary Mg-RE alloys (Chia et al., 2009). Thus, it can be difficult to determine which form the secondary phases will precipitate as (Chia et al., 2009).

2.3.1.3 Influence of Calcium

Concerns over the biocompatibility of other alloying elements has led researchers to investigate Mg-Ca alloys, since Calcium (Ca) is a major component of bone in the form of hydroxyapatite (HA). As such, Mg-Ca alloys have been shown to exhibit good biocompatibility (Li et al., 2008; Erdmann et al., 2011).

The inclusion of Ca reduces the density closer to natural bone (Li et al., 2008), further reducing the potential problems with stress shielding effects. Ca also shows a high level of grain refinement in Mg alloys up to additions of 0.5 % (Ding et al., 2014). Further addition of Ca results in a slight decrease in the grain refinement. The secondary phases of binary Mg-Ca alloys are Mg_2Ca , which are distributed along the grain boundaries (Ding et al., 2014). Mg_2Ca reduces ductility on account of its brittleness, and increasing the volume fraction reduces the degradation resistance due to the formation of microgalvanic cells (Kim et al., 2011). For these reasons, it has been suggested that the optimal concentration of Ca is ≤ 1.0 %. However, Mg-Ca alloys show a mixture of both $Mg(OH)_2$ and HA films precipitating on the surface during degradation, which may be beneficial in the inhibition of further degradation (Li et al., 2008).

2.3.1.4 Influence of Manganese and Zinc

Manganese (Mn) is widely used as a secondary alloying element in Mg alloys. Mn itself does not react with Mg, and does not directly improve degradation resistance, but is often included to improve mechanical properties. Increasing Mn in Mg-Al-Mn alloys, for instance, produces improved grain refinement up to concentrations of 0.4 % Mn

(Avedesian et al., 1999). Furthermore, the addition of Mn in the AZ series alloys transforms Fe and other materials into more harmless intermetallics. While these intermetallics still produce microgalvanic cells (thereby increasing the overall degradation rate), the difference in activity is reduced, resulting in a much smaller effect. It has been suggested by multiple authors that the addition of 1 % Mn is beneficial in this regard (Gu et al., 2009; Nam et al., 2012).

Similarly, Zinc (Zn) transforms impurities into less harmful intermetallics. Zn is commonly used with Mg-Al alloys, due to the formation of these secondary phases, as well as improving grain refinement. Several studies have reported that Zn improves the degradation resistance of several ternary Mg alloys (Rosalbino et al., 2010; Gu et al., 2010). However, some studies contradict these results, and have suggested that the inclusion of Zn is detrimental to the degradation resistance of Mg alloys. Song et al. (Song et al., 2012) reported that the microgalvanic effects played a dominant role in the degradation behaviour of Mg-Zn alloys in 3.5 % NaCl, and suggested that the concentration of Zn should be less than 5.0 %.

2.3.2 Secondary Phases and Microgalvanic Degradation

Table 2.3 is a list of the widely studied Mg alloys under in vitro and/or in vivo conditions. All the studies have focussed on the overall degradation behaviour of Mg alloys. However, it can be noticed that the Mg alloys used in the studies contain secondary phase particles. Due to the difference in chemistry, these secondary phase particles will have different dissolution behaviour as compared to that of Mg matrix.

Galvanic degradation occurs when two or more metals are in contact with each other in the presence of an electrolyte, resulting in the preferential dissolution of the more active metal. When this process within a single alloy, due to differences in activity between the matrix and secondary phases, it is referred to as microgalvanic degradation. Table 2.4 shows the corrosion potentials for Mg and common secondary phases in 5 % Na Cl.

Secondary phase particles in Mg alloys are generally cathodic to the Mg matrix and are more degradation resistant than the Mg matrix (Song and Atrens, 1999; Ghali et al., 2004; Song and Atrens, 2007). In chloride-containing solution, the secondary phase particles play a dual role on the degradation behaviour of these alloys (Song et al.,

1998; Song et al., 1999). If the volume fraction of these secondary phase particles is relatively high, they improve the degradation resistance of the alloy by acting as a stable barrier against degradation, i.e., dissolution of the Mg matrix can leave behind a continuous network of the stable secondary phase particles. Conversely, if the volume fraction is low, the secondary phase particles act as cathodic sites for micro-galvanic degradation of the anodic Mg matrix and consequently increase the rate of dissolution of the Mg matrix (Song et al., 2012a).

Recently, Kannan (Kannan, 2010) studied the influence of microstructure on the in vitro corrosion behaviour of AZ91, and found that the β -phase ($\text{Mg}_{17}\text{Al}_{12}$) was stable in SBF as compared to the Mg matrix. The die-cast AZ91 alloy, which contains a large volume fraction of β -phase, clearly revealed a stable network of β -phase after potentiodynamic polarisation test. This stable network of secondary particles has been widely reported in AZ91 alloy immersed in chloride-containing solutions (Song et al., 1999; Ambat et al., 2000; Kannan and Singh, 2010; Jönsson and Persson, 2010). In a more recent study, Kannan et al. (Kannan et al., 2012) examined the short-term biodegradability of β -phase alone in SBF. It was found that the β -phase was noble to pure Mg by 680 mV, and the authors reported 80% higher degradation resistance for β -phase than that of pure Mg.

Since there is a significant difference in the electrochemical potential between β -phase and Mg, the Mg alloys containing β -phase would undergo micro-galvanic degradation. The effects of secondary phase distribution and refinement in AZ80 in 3.5 % NaCl were reported by Sun et al. (Sun et al., 2013), there has been no work on this form of degradation in physiological conditions. Recently, Kalb et al. (Kalb et al., 2012) reported deposits of $\text{Mg}(\text{OH})_2$ around micro-cathodes, i.e., zirconium and iron rich particles in WE43 alloy.

Table 2.3

In vitro and in vivo studies of Mg alloys and their secondary particles.

Alloy Group	Alloy	Composition (Wt. %) (Bal. Mg)	Secondary Particles	References
Mg-Al-Zn	AZ31	3 Al, 1 Zn	Mg ₁₇ Al ₁₂	Witte et al., 2005; Song et al., 2009; Zhang et al., 2012
	AZ63	6 Al, 3 Zn	Mg ₁₇ Al ₁₂	Liu et al., 2007
	AZ91	9 Al, 1 Zn	Mg ₁₇ Al ₁₂	Witte et al., 2006; Kannan, 2010; Zhou et al., 2010; Gu et al., 2010a; Abidin et al., 2011
Mg-RE	WE43	4 Y, 3 RE mischmetal: Nd, Zr, Yb, Er, Dy, Gd)	Mg ₁₂ YNd, Mg ₁₄ YNd ₂	Rettig and Virtanen, 2009; Hänzi et al., 2009; Kalb et al., 2012
	WE54	4.58 Y, 1.58 Nd, 0.28 Zr, trace Ce, Gd, Er and Yb	Mg and Y rich	Walter and Kannan, 2011
	Mg-Nd-Zn-Zr	3.09 Nd, 0.22 Zn, 0.44 Zr	Mg ₁₂ Nd	Zhang et al., 2012; Zong et al., 2012
Mg-Ca	Mg-xCa	(x = 0.5-10) Ca	Mg ₂ Ca	Wan et al., 2008; Rad et al., 2012
	Mg-Zn-Ca	4.0 Zn, 0.2Ca	As cast: Ca ₂ Mg ₆ Zn ₃ and Ca ₂ Mg ₅ Zn ₁₃ Extruded: Ca ₂ Mg ₆ Zn ₃	Sun et al., 2011; Sun et al., 2011a
	AZ61-Ca	6 Al, 1 Zn, 0.4 Ca	Mg ₁₇ Al ₁₂ , Al ₂ Ca	Kannan and Raman, 2008
	AZ91-Ca	9 Al, 1 Zn, 1 Ca		
	Mg-Zr-Ca-Sn-Sr	5 Zr, 1 Ca, 8 (Sn+Sr)	Mg ₂ Sn, another phase rich in Mg, Ca, Sr and Sn	Zhang et al., 2012a
Mg-Zn	ZE41	4 Zn, 1 RE (primarily Sr)	Mg ₇ Zn ₃ , Mg ₁₂ RE	Abidin et al., 2011
	Mg-Zn-Mn	2 Zn, 0.2 Mn	Mg ₇ Zn ₃	Zhang et al., 2009
	Mg-Zn-Mn	(1-3) Zn, 1Mn	Mg-(1,2)Zn-Mn: Al-Mn (ratio 4:5) Mg-(3)Zn-Mn: Al-Mn (ratio 4:5) and Mg ₇ Zn ₃	
Mg-Si	Mg-Si	0.6 Si	Mg ₂ Si	Zhang et al., 2010
	Mg-Si-Ca	0.6 Si, (0.2-0.4) Ca	Mg ₂ Si, CaMgSi	
	Mg-Si-Zn	0.6 Si, 1.5 Zn	Mg ₂ Si, MgZn	

Table 2.4

Typical corrosion potentials for Mg and common secondary phases in 5 % NaCl (Song and Atrens, 2003).

Metal	E_{corr} (V_{SCE})	Metal	E_{corr} (V_{SCE})
Mg	-1.65	Beta-Mn	-1.17
Mg ₂ Si	-1.65	Al ₄ Mn	-1.15
Al ₆ Mn	-1.52	Al ₆ Mn(Fe)	-1.10
Al ₄ Mn	-1.45	Al ₆ (MnFe)	-1.00
Al ₈ Mn ₅	-1.25	Al ₃ Fe(Mn)	-0.95
Mg ₁₇ Al ₁₂ (β)	-1.20	Al ₃ Fe	-0.74

The accelerated dissolution of the Mg matrix due to microgalvanic effects means that the degradation rate is highly dependent on impurity levels, most notably Fe, and to a lesser extent, Cu, Ni, and Co. The tolerance limit for Fe in as-cast Mg is 180 wt. ppm, corresponding to the eutectic composition in the Mg-Fe phase diagram (Liu et al., 2009a). The Fe rich phase that forms above this concentration allows the hydrogen evolution reaction to occur easily, thereby acting as an effective cathode. The inclusion of Fe is of practical concern, since Fe is readily incorporated into the material from steel containers during the casting process.

2.4 Biodegradable Coatings

While alloying with elements such as Al, Zn and REs can improve the degradation resistance (Song and Atrens, 2003; Witte et al., 2006; Walter and Kannan, 2011), localised degradation is still a major concern (Witte, et al., 2008). Pits caused by localised degradation act as stress risers, leading to the propagation of cracks from hydrogen embrittlement and/or stress corrosion cracking (Winzer et al., 2005; Winzer et al., 2007). For this reason, there has been a large amount of research aimed at developing a coating that provides a barrier for the Mg substrate that reduces localised

degradation, but is eventually resorbed by the body. There has been a wide range of coatings and surface modifications studied to this end, including surface treatment (Gu et al., 2009; Hwang et al., 2012), plasma electrolytic oxidation (Gu et al., 2012; Alabbasi et al., 2013), biodegradable polymers (Chen et al., 2011, Alabbssi et al., 2012), and calcium phosphate deposition (Kannan and Orr, 2011; Hornberger et al., 2012).

2.4.1 Calcium phosphate (CaP)

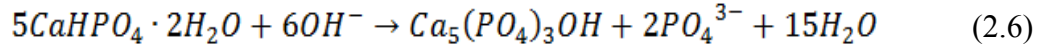
Calcium phosphate (CaP) coatings are known for their high bioactivity and biocompatibility, and have already been used on metallic implant materials such as titanium to improve osseointegration and osteoconductivity (Manso et al., 2000; Kuo and Yen, 2002; Liu et al., 2002; Le Guéhennec et al., 2007; Best et al., 2008). More recently, there has been research done to use these CaPs as a method of controlling the degradation rate of Mg and Mg alloys for implant applications. While these coatings have shown improvement in these degradation rates, issues with cracking, poor adherence and difficulties with phase formation are still cause for concern (Hornberger et al., 2012). Table 2.5 shows a summary of the most common CaP phases used for coating orthopaedic devices.

Table 2.5
Common CaP phases used for coating orthopaedic devices (Shadanbaz and Dias, 2012).

Name	Acronym	Formula	Ca/P ratio
Calcium phosphate dihydrate	DCP	$\text{CaHPO}_4 \cdot 2\text{H}_2\text{O}$	1.0
Anhydrous calcium phosphate	ADCP	CaHPO_4	1.0
Octocalcium phosphate	OCP	$\text{Ca}_8\text{H}_2(\text{PO}_4)_6 \cdot 5\text{H}_2\text{O}$	1.33
Tricalcium phosphate	TCP	$\text{Ca}_3(\text{PO}_4)_2$	1.5
Hydroxyapatite	HA	$\text{Ca}_{10}(\text{PO}_4)_6(\text{OH})_2$	1.67

2.4.1.1 Calcium phosphate dihydrate (DCP) and anhydrous calcium phosphate (ADCP)

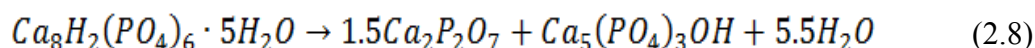
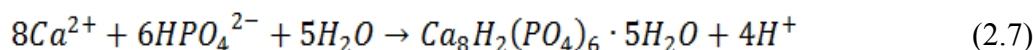
DCP is relatively inexpensive to produce and easy to coat onto metallic substrates (Narayanan et al., 2008). However, it exhibits greater solubility than most other CaP structures (LeGeros et al., 1988; Kumar et al., 1999; Dorozhkin and Epple, 2002). For this reason, it is sometimes used to promote osseointegration, since the higher solubility allows for a greater concentration of available Ca and P ions immediately near the bone (Kumar et al., 1999a). In terms of protective coatings, however, DCP is more widely used as a precursor to HA (Redepenning et al., 1996; Kumar et al., 1999; Xie et al., 2001). In pH greater than ~6-7, DCP transforms into the more thermodynamically favourable HA (Levinskas, and Neuman, 1955; Strates et al., 1957). The direct synthesis of HA via precipitation produces a tightly packed crystal structure, but the crystal size is difficult to control. A simple method to combat this is by precipitating DCP as an intermediary, since it is much easier to control the crystal size, and then transforming directly into HA by adjusting pH (Redepenning et al., 1996). The transformation of DCP to HA can be shown as follows:



ADCP has been studied much less than DCP, but shares many of the traits described above. The solubility is higher than that of DCP (Dorozhkin and Epple, 2002; Klammert et al., 2009), and as such can be used to promote osseointegration in a similar manner to DCP (Kumar et al., 1999a). ADCP is stable at relatively low pH values (~4-5) (Fujishiro et al., 1993; Fujishiro et al., 1995; Sivakumar et al., 1998), but transforms to HA at pH of ~6-7 (Fujishiro et al., 1993; Štulajterová, and Medveck, 2008).

2.4.1.2 Octacalcium phosphate (OCP)

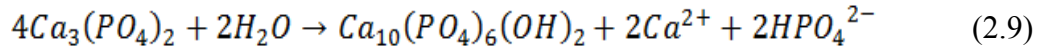
OCP is the most stable of the CaPs at physiological temperature and pH (Barrère et al., 2001; Barrère et al., 2003; Habibovic et al., 2005), and exists as alternating layers of apatite and hydrated layers (Barrère et al., 2006). It is most often observed as an intermediate structure during the precipitation of HA. The reaction can be shown by (Barrère et al., 1999; Brown et al., 1987):



Under more acidic conditions, OCP transforms into a more bone-like apatite (Reiner and Gotman, 2010; Barrere et al., 2003a), and is known to be a precursor to bone mineralisation (Barrère et al., 2001). For this reason, OCP has been suggested as a coating material to aid in bone healing, since inflammatory responses produce acidic conditions (Barrere et al., 2003a; Habibovic et al., 2004). OCP has demonstrated good biocompatibility in *in vitro* studies (Bogdanski et al., 2004; Socol et al., 2004; Bigi et al., 2005; Mihailescu et al., 2005; Shelton et al., 2006). However, most studies on an Mg substrate have been limited to biphasic coatings containing both HA and OCP (Cui et al., 2008; Xu et al., 2009; Ohtsu et al., 2013).

2.4.1.3 Tricalcium phosphate (TCP)

TCP most commonly crystallises as two phases, depending on sintering temperature: α -TCP, a monocyclic space group (Viswanath et al., 2008) and β -TCP, a rhombohedral space group (Dickens et al., 1974). α -TCP occurs at sintering temperatures above 1250 °C, whereas β -TCP is the dominant phase at temperatures below this (Drlesson et al., 1982; TenHuisen and Brown, 1998). TCP is most commonly studied as a biphasic coating alongside HA. Studies have shown that biocompatibility is improved for these biphasic coatings at higher HA:TCP ratios (Yamada et al., 1997), either due to the higher solubility of TCP compared to HA (Kokubo et al., 1990; Klein et al., 1994), or differences in porosity (Bigi et al., 2002). HA/TCP coatings on Ti implants have already been utilised in a clinical setting, and have demonstrated improved biocompatibility and decreased bone loss when compared to uncoated implants (Shimizaki and Mooney, 1985). Geng et al. (Geng et al., 2009) produced pure β -TCP, on an Mg substrate, and reported good cytocompatibility, and suggested that it may be viable to reduce the biodegradation of Mg at early stages of immersion. Notably, Geng et al. suggested that the degradation of β -TCP would continuously form HA and $CaPO_3(OH)$ (another HA precursor) on the surface, as shown by the following reactions (Geng et al., 2009):



2.4.1.4 Hydroxyapatite (HA)

HA has been widely studied as a biocompatible coating for implant applications on both Ti (Manso et al., 2000; Kuo and Yen, 2002; Dumelie et al., 2008) and Mg substrates (Song et al., 2010; Wang et al., 2010, Kannan and Orr, 2011). It is the major mineral component of natural bone and teeth, alongside the organic components (Shadanbaz and Dias, 2012). Non-stoichiometric HA is more common than the structure described in Table 2.4, as hydroxyl groups can be substituted with fluoride, chloride and carbonates (Shadanbaz and Dias, 2012). HA has demonstrated good biocompatibility (Guo et al., 2009; Sandeman et al., 2009), and multiple *in vivo* tests have reported apparent bone regeneration (Chu et al., 2002; Tamai et al., 2002). HA is typically deposited in a two-step method: First by depositing the precursor CaP (DCP, β -TCP or OCP), and then transforming it in a low pH environment as shown in reactions 2.6 - 2.9.

2.4.1.5 Coating Methods

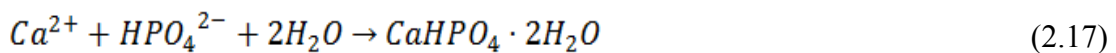
There are a number methods available for the coating of calcium phosphate onto a metallic substrate, such as sputtering (Ong et al., 1992; De Groot et al., 1998), plasma spraying (Tsui et al., 1998; Yang et al., 2005), and sol-gel techniques (Cai et al., 2009; Roy et al., 2011). However, these are often complicated or high temperature techniques, potentially resulting in a decomposition and non-uniformity of the coating when used on an Mg substrate. Low temperature chemical techniques can be used to easily precipitate CaP without damaging the Mg substrate. For example, the formation mechanism of β -TCP on Mg in the presence of Ca^{2+} and HPO_4^{2-} is given in reactions 2.11 – 2.13. The alkaline environment that occurs near the Mg surface allows for the transformation of HPO_4^{2-} to PO_4^{3-} , and subsequently to $Ca_3(PO_4)_2$ (Geng et al., 2009):





Similarly, biomimetic techniques precipitate out the desired coatings onto the substrate, and are performed in near physiological conditions (Kim, 2003). Rettig and Virtanen (Rettig and Virtanen, 2009) were able to biomimetically produce a number of surface coatings on an Mg alloy by adjusting the bath solutions. Rettig and Virtanen immersed the Mg-RE alloy in blood plasma, NaCl + additives, SBF, and SBF + albumin for a period of 5 days. The authors reported that the CaP layer formed in the SBF solutions was an amorphous carbonated CaP layer, with some Ca substituted with Mg. However, the results indicated significant localised grain boundary degradation, and it was suggested that the coating would not be viable where fatigue failure is possible (Rettig and Virtanen, 2009).

Another method is electrochemical precipitation, which can be done rapidly and at room temperature. Further, it is possible to coat materials with complex geometries, which is an essential characteristic for implants such as plates and screws. There has been some research done on the galvanostatic (Dumelie et al., 2008; Song et al., 2010) and potentiostatic (Song et al., 2008; Kannan and Orr, 2011) deposition of CaP. There has also been some work done showing that CaP coatings on Mg can improve the degradation resistance (Xu et al., 2009; Shadanbaz and Dias, 2012; Shadanbaz et al., 2013). However, a limitation of these techniques is that rapid deposition of CaP results in the evolution of large amounts of hydrogen gas, as shown in the following reactions describing the precipitation of DCP (Redepenning et al., 1996):



The hydrogen build-up on the surface eventually detaches and damages the CaP layer, resulting in a loosely packed and inhomogeneous structure. Further, in the case of potentiostatic deposition, a negatively charged layer forms across the surface, which impedes the adherence of ions (Chandrasekar et al., 2008). These issues can reportedly be overcome by utilising a pulsed-potential waveform (Chandrasekar et al., 2008). Kannan (Kannan and Wallipa, 2013) compared constant and pulsed-potential CaP coatings on AZ91 alloy. It was reported that the pulsed potential technique produced more densely packed coatings, which were able to provide significant improvements in the degradation performance when compared to potentiostatic deposition.

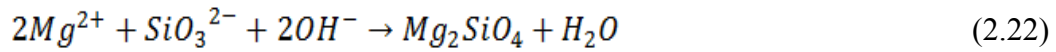
Another study by the same author utilised an unconventional electrolyte, which contained ethanol in addition to $\text{Ca}(\text{NO}_3)_2$ and $\text{NH}_4\text{H}_2\text{PO}_4$ (Kannan, 2013). It was reported that use of this unconventional electrolyte resulted in improvements in the degradation performance when compared to the conventional aqueous solution coating. A third study by the same author combined the pulsed-potential technique with the unconventional electrolyte, and reported that the synergistic effects of the two methods produced coatings with higher degradation resistance on AZ91 alloy than in previous work (Kannan, 2012). It should be noted, however, that none of these coatings have been able to provide the long term degradation resistance required for implant applications.

2.4.2 Plasma Electrolytic Oxidation (PEO)

Plasma electrolytic oxidation (PEO), or micro arc oxidation (MAO), is a chemical conversion technique similar to anodisation that produces an oxide layer through the use of high potentials. The PEO technique produces dense, hard and uniform layers that are resistant to abrasion and degradation (Krishna and Sundararajan, 2014). Furthermore, since PEO is a conversion coating, rather than a deposition, excellent adherence to the substrate is observed (Yerokhin et al., 1999). The formation of the PEO layer can be described via metal dissolution and resultant oxide formation (Walsh et al., 2009):



It should be noted that the layer will also have hydrates and other compounds alongside the oxides. For example, in a silicate-based electrolyte, both $Mg(OH)_2$ and Mg_2SiO_4 would form when the concentrations of Mg^{2+} , SiO_3^{2-} and OH^{-} reaches a critical value at the electrode/electrolyte interface (Duan et al., 2007):



The anodic currents also evolve oxygen, via the following reactions (Walsh et al., 2009):



Table 2.6 gives a summary of some of the studies done on PEO coatings on Mg alloys. The resultant structure is a dual layer coating. The layer adjacent to the substrate is a thin, highly compact layer, which has been shown to greatly contribute to the overall degradation resistance of the coating (Ghasemi et al., 2008; Liang et al., 2009). On top of this is a thicker, highly porous layer with a pore size range from $\sim 1 - 10 \mu m$ (Krishna and Sundararajan, 2014; Guo et al., 2006). This porous structure forms during the coating process due to the co-existence of molten oxide and gas bubbles (Yerokhin et al., 1999). Research suggests that the porous nature of the outer layer allows for penetration of electrolyte over time, reducing the effectiveness of the coating. Alabbasi et al. (Alabbasi et al., 2013) investigated the *in vitro* performance of a pulsed-potential phosphate-based PEO layer on Mg. The authors reported a 65 % reduction in the corrosion current and an order of magnitude increase in the polarisation resistance when compared to the bare metal. However, EIS modelling indicated that very little of

the overall resistance came from the porous layer, and was instead dominated by the compact, inner layer. Post-degradation analysis suggested that the porous outer layer did however play an important role on the stability of the inner layer.

The coating electrolyte is most commonly comprised of aqueous silicates, phosphates, aluminates and hydroxides, as can be seen in Table 2.6. In general, PEO coatings produced in a phosphate electrolyte contain more micropores than those produced in silicate electrolytes, which are typically more compact and uniform (Liang et al., 2007a). As a result, silicate-based PEO coatings are more degradation resistant than their phosphate-based counterparts (Liang et al., 2009). Liang et al. (Liang et al., 2009) suggests that even under identical pore morphology, silicate-PEO would produce a stable passive film (Mg_2SiO_4), whereas in the case of phosphate-PEO, degradation products ($\text{Mg}(\text{OH})_2$) would grow enough to damage the coating and expose the underlying substrate.

Table 2.6
Examples of PEO coatings on Mg alloys.

Substrate Alloy	Operational Conditions (Voltage, Current density, Coating time, Temperature)	Coating electrolyte	Thickness (μm)	Compounds in oxide layer	Reference
AM60 (6 % Al, 0.27 % Mn)	25 - 300 mA/cm ² , 2 - 10 min	Na ₅ P ₃ O ₁₀ , KOH, KF	2 – 10	N/A	Boinet et al., 2005
AZ91D (8.5-9.5 % Al, 0.5-0.9 % Zn)	550 V, 5 - 20 mA/cm ² , 40 min	NaAlO ₂ , KOH, KF	N/A	MgAl ₂ O ₄ , Al ₂ Mg	Guo et al., 2005
AM60B (5.6-6.4 % Al, 0.26-0.4 % Mn)	60 mA/cm ² , 30 min, 25 - 30 °C	Na ₂ SiO ₃ , KOH , KF	32 – 37	MgO, KMgF ₃ , Mg ₂ SiO ₄ , MgAl ₂ O ₄ , MgF ₂	Liang et al., 2005
MA2-1 (4.2 % Al, 1.2 % Zn, 0.5 % Mn)	5 - 12 mA/cm ² , 20 - 25 °C	Na ₅ P ₃ O ₁₀ , NaOH	50 – 88 μm	N/A	Timoshenko and Magurova, 2005
AZ91D (8.5-9.5 % Al, 0.5-0.9 % Zn)	470 V, 30 mA/cm ² , 20 min, 40 °C	Na ₂ SiO ₃ , NaOH	15 – 30 μm	Mg, MgO, Mg ₁₇ Al ₁₂	Jin et al., 2006
AZ91D (8.5-9.5% Al, 0.5-0.9% Zn)	100 - 350 V, 30 s - 30 min	Na ₂ SiO ₃ ,KOH	2 – 24 μm	Contains Mg, O, Al and Si	Duan et al., 2007
AM60B (5.6-6.4 % Al, 0.26-0.4 % Mn)	3 - 6 mA/cm ² , 30/ 40/51 min, 25 - 30 °C	Na ₂ SiO ₃ , KOH	N/A	MgO, Mg ₂ SiO ₄ , MgAl ₂ O ₄	Liang et al., 2007

Table 2.6 (continued)
Examples of PEO coatings on Mg alloys.

Substrate Alloy	Operational Conditions (Voltage, Current density, Coating time, Temperature)	Coating electrolyte	Thickness (μm)	Compounds in oxide layer	Reference
AM60B (5.6-6.4 % Al, 0.26-0.4 % Mn)	200 - 520 V, 6 mA/cm ² , 5 - 30 min, 25 - 30 °C	Na ₂ SiO ₃ , KOH	14 - 37 μm	MgO, Mg ₂ SiO ₄	Liang et al., 2007a
		Na ₃ PO ₄ , KOH	13 - 36.5 μm	MgO, MgAl ₂ O ₄	
AZ91D (9.1 % Al, 0.85 % Zn)	400 V, 10 min, 40 °C	Na ₂ SiO ₃ ·9H ₂ O, KOH, KF·2H ₂ O	20 - 50 μm	MgO, Mg ₂ SiO ₄ , MgAl ₂ O ₄	Luo et al., 2008
AZ91Nd (8.6 % Al, 0.74 % Zn, 1.02 % Nd)	400 V, 30 mA/cm ² , 10 min, 25 °C	NaAlO ₂ , NaOH	N/A	Mg ₁₇ Al ₁₂ , Al ₂ Nd, Nd ₂ O ₃	Song et al., 2008a
AM50 (5 % Al, 0.5 % Mn)	15/75/150 mA/cm ² , 15 min, 21 ± 2 °C	Na ₂ SiO ₃ , KOH	1 ± 0.5 μm	MgO Mg ₂ SiO ₄	Srinivasan et al., 2009
			4 ± 1 μm 8 ± 2 μm		
AM50 (4.4-5.5 % Al, 0.26-0.6 % Mn)	15 mA/cm ² , 30 min, 10 ± 2 °C	Na ₂ SiO ₃ , KOH	17 ± 3 μm	MgO, Mg ₂ SiO ₄	Liang et al., 2010
		Na ₃ PO ₄ , KOH	25 ± 2 μm	MgO, Mg ₃ (PO ₄)	
AZ31 (2.5-3.5 %Al, 0.7-1.3 % Zn)	325 V, 5 min	Na ₃ PO ₄ , KOH	N/A	Contains Mg, O, Al, P, Zn, Na and Mn	(Gu et al., 2012)

2.4.3 Organic Polymer Coatings

Biodegradable polymers have been used extensively in the medical field as a controlling release carrier for drug delivery (Jain, 2000; Peppas et al., 2000). A critical attribute of these polymers is that it is possible to modulate the biodegradation rate (and thus the rate of drug delivery) by altering the physical or chemical properties (Wu and Ding, 2004). Table 2.7 lists the abbreviations in the upcoming sections, and Table 2.8 shows the mechanical properties and degradation rate of some of the commercially available biodegradable polymers. While the mechanical properties are too low for load-bearing applications, biodegradable polyesters such as PLA, PGA and their copolymers have gained interest as biodegradable coatings. The following sections will focus on the most common biodegradable polymers in biomedical applications, poly(α -ester)s, most notably polylactic acid (PLA) and polyglycolic acid (PGA).

Table 2.7
Polymer abbreviations (Middleton and Tipton, 2000).

Abbreviation	Polymer
LPLA or PLLA	poly(L-lactide)
DLPLA	poly(DL-lactide)
LDLPLA	poly(DL-lactide- <i>co</i> - L-lactide)
PGA	Poly(glycolide)
LPLG	poly(L-lactide- <i>co</i> -glycolide)
DLPLG	poly(DL-lactide- <i>co</i> -glycolide)
PDO	poly(dioxanone)
PCL	poly(ϵ -caprolactone)
SR	self-reinforced

Table 2.8
Commercial polymer biodegradable devices (Middleton and Tipton, 2000).

Polymer	Glass transition temperature (°C)	Modulus^a (GPa)	Elongation (%)	Degradation time (months)^b
PGA	35 – 40	7.0	15 – 20	6 – 12
LPLA	60 – 65	2.7	5 – 10	> 24
DLPLA	55 – 60	1.9	3 – 10	12 – 16
PDO	-10 – 0	1.5	300 – 500	6 – 12
85/15 DLPLG	50 – 55	2.0	3 – 10	5 – 6
75/25 DLPLG	50 – 55	2.0	3 – 10	4 – 5
65/35 DLPLG	45 – 50	2.0	3 – 10	3 – 4
85/15 DLPLG	45 – 50	2.0	3 – 10	1 – 2

^aTensile or flexural modulus

^bComplete resorption

Poly(lactic acid) (PLA) is a thermoplastic that has already seen a wide application in the medical field as a biodegradable biomaterial as sutures and non-load bearing plates and screws (Lunt, 1998). They are aliphatic polyesters that are present in three isometric forms: the optically chiral L-lactide and D-Lactide, as well as the racemic (D, L)-lactide form. Polymerisation of the D and L-lactide forms results in a semi-crystalline polymer, however the racemic form polymerises amorphyously (Nair and Laurencin, 2007). Poly(L-lactide), or PLLA exhibits a crystallinity of ~37 %, depending on molecular weight and processing parameters (Nair and Laurencin, 2007). PLLA also exhibits good tensile strength and a relatively high elastic modulus of ~4.8 GPa (Nair and Laurencin, 2007).

Polyglycolic acid (PGA) is a highly crystalline (45 – 55 % crystallinity) thermoplastic, and can be considered one of the first synthetic polymers used for biodegradeable biomedical applications (Nair and Laurencin, 2007). PGA exhibits relatively good

mechanical properties compared to other biodegradable polymers, with the self-reinforced form having an elastic modulus of ~ 12.5 GPa (Maurus and Kaeding, 2004). For this reason, PGA has been investigated as a biomaterial for bone fixation devices. However, the relatively high rate of degradation and low solubility of the polymer has limited its potential biomedical applications, and several glycolide-containing co-polymers are being developed to offset these disadvantages (Nair and Laurencin, 2007).

The most widely investigated co-polymer is poly(lactide-*co*-glycolide) (PLGA). The composition ranges from 25 – 75 % to form an amorphous polymer, and is co-polymerised using both L- and DL-lactides (Nair and Laurencin, 2007). It has been reported that a 50/50 % composition is highly hydrolytically unstable, and the resistance to degradation increases at both ends of the co-polymerisation range (Miller et al., 1977; Gunatillake et al., 2006).

The degradation of PLA and PGA occurs through the hydrolysis of the backbone ester groups, resulting in the formation of lactic and glycolic acids respectively (Zhang et al., 1994). This occurs by the random chain scission of the ester groups, along with a reduction in the molecular weight. These polymers experience bulk erosion, rather than surface erosion, and PLA films have been identified as degrading faster in the centre of the film as opposed to the surface (Huang et al., 2006; Nair and Laurencin, 2007). Fluid penetrates the polymer bulk, and catalyses the faster cleavage of the ester bonds within the polymer (Zhang et al., 1994). Over time, a decrease in the molecular weight can be observed, followed by a loss in mechanical properties (Zhang et al., 1994; Middleton and Tipton, 2000). During hydrolytic degradation, chain cleavage increases the number of carboxylic chain ends, which auto catalyse the ester hydrolysis (von Burkersroda et al., 2002). Oligomers close to the surface are able to escape the matrix, while the rest remain trapped and contribute to the autocatalytic effect (Huang et al., 2006). Athanasiou (Athanasiou et al., 1998) reported that 50/50 DLPLG implants with a low porosity experience a more rapid degradation than those of high porosity. This was attributed to the more rapid diffusion of the low pH degradation products in the high porosity implants from the interior to the surface. Degradation rate is also affected by a range of other parameters, including molecular weight, crystallinity, and the presence of catalysts and location of the device (Lunt, 1998; Middleton and Tipton, 2000). The

degradation products, lactic and glycolic acid, are broken down into water and carbon dioxide via the citric acid cycle in the body (Maurus and Kaeding, 2004).

PLLA is a slow degrading polymer, taking between 2 and 5.6 years for total *in vivo* resorption (Bergsma et al., 1995). This rate is highly dependent on polymer crystallinity and matrix porosity. However, it should be noted that while the polymer will experience no mass loss until long exposure times, PLLA loses its mechanical strength in only 6 months when hydrolysed (Nair and Laurencin, 2007). In contrast to PLLA, PGA experiences a comparatively high rate of degradation and mass loss. PGA has been shown to lose its mechanical strength within 1 – 2 months, and loses mass within 6 – 12 months (Nair and Laurencin, 2007). The degradation rates of PLGA depend heavily on the ratios of the co-polymer composition. 50/50 PLGA degrades in only 1 – 2 months, whereas 75/25 and 85/15 are more stable, at 4 – 5 months and 5 – 6 months respectively (Middleton and Tipton, 2000).

2.4.3.1 Coating Methods

The simplest method of polymer deposition is through a single step method, such as dip coating or spin coating. In general, dip coating produces a thick, non-uniform coating, potentially resulting in poor adhesion to the substrate. Furthermore, dip coating tends to result in a higher concentration pores and defects when compared to spin coating (Hong and Park, 2011). Chen et al. (Chen et al., 2011) utilised a dip-coating method to deposit PLA on a pure Mg substrate. While the coating improved the degradation resistance, the authors reported bulging after prolonged exposure to SBF. Similarly, Ostrowski et al. (Ostrowski et al., 2013) polylactic-co-glycolic acid (PLGA) polymer on two Mg alloys using a dip coating method. The study reported some improvement in the *in vitro* degradation resistance, but this was reduced after 3 days immersion. The authors attributed this to coating detachment due to gas pocket formation.

Spin coating is a second single step method for depositing polymer coatings. This method is widely used for both its simplicity, and ability to produce homogenous polymer films with a relatively low porosity when compared to dip coating. The process typically involves depositing the desired polymer solution (comprised of the relevant monomer dissolved in an organic solvent) onto the Mg substrate, and then

rotating at high speeds. This evaporates the solvent, leaving a residual polymer film on the substrate.

Li et al. (Li et al., 2010) deposited PLGA on an Mg6Zn substrate, with a reported thickness of 33 and 72 μm . Both coatings showed an improvement in the degradation resistance in NaCl by polarisation and impedance testing. Interestingly, the thicker coating showed a lower resistance than the thin coating, which was attributed to voids and flaws. Chen et al. (Chen et al., 2011) produced PCL and PLA coatings on a pure Mg substrate, with reported thicknesses of 15-20 μm . *In vitro* testing showed some degradation resistance improvement, but interactions between the polymer layer and the substrate undermined the degradation resistance.

Xu and Yamamoto (Xu and Yamamoto, 2012) utilised a spin coating method to produce PLLA and PCL films on pure Mg. The results showed that uniform, amorphous, nonporous PLLA and semi-crystalline PCL films were present on the substrate. The authors reported that PLLA had better adhesion strength than that of PCL, and that low molecular weight exhibited better adhesion than high molecular weight for both polymers. Xu and Yamamoto (Xu and Yamamoto, 2012) also reported that both polymer coatings improved the initial degradation resistance and cytocompatibility of the Mg substrate. However, Mg^{2+} concentrations increased over time, suggesting that the electrolyte was able to permeate the polymer layer. Similarly, Alabbasi et al. (Alabbasi et al., 2012) showed that the addition of a PLA coating on an Mg substrate could improve the initial *in vitro* degradation resistance, but this effect was reduced over exposure time.

Chapter. 3 Materials and Methodology

3.1 Introduction

As stated in Chapter 1, this thesis covers four main objectives related to furthering the understanding of the biodegradation of Mg. The metal samples tested in this work were high purity Mg, AZ91 alloy, and Mg-Ca alloy. The specific compositions are described in their relevant chapters. This chapter outlines the methods used to meet the research objectives, with considerations given to the literature findings discussed in Chapter 2. Parameters specific to each experiment are further outlined in their respective chapters where necessary. Figure 3.1 shows the general outline of the specific research objective and methods used to achieve it in each chapter.

3.2 In-vitro Degradation and Electrochemical Degradation Techniques

Degradation behaviour was measured primarily through the use of electrochemical techniques, as described in the following sections. The setup was comprised of a typical 3 electrode cell connected to a potentiostat, as shown in Figure 3.2. Electrochemical degradation experiments were carried out using a model ACM Gill AC potentiostat, and a Princeton VersaSTAT 3 potentiostat/frequency response analyser controlled by PowerCORR and PowerSINE software. The working electrode is the metal sample, the counter electrode is either graphite or platinum, and the reference electrode is Ag/AgCl in saturated KCl. Prior to all electrochemical experiments, the system was allowed to reach a stable open circuit potential (OCP).

The degradation electrolyte is a buffered SBF that matches the ionic concentration of that found in human body fluid, the composition of which can be seen in Table 3.1. The SBF was maintained at pH 7.40 and 37 °C to match physiological conditions. As seen in Figure 3.2, the SBF is heated in a separate reservoir and constantly flows to the cell containing the sample in order to maintain the desired temperature. For long term experiments, the SBF solution was replaced every 12 hours for the duration of the testing.

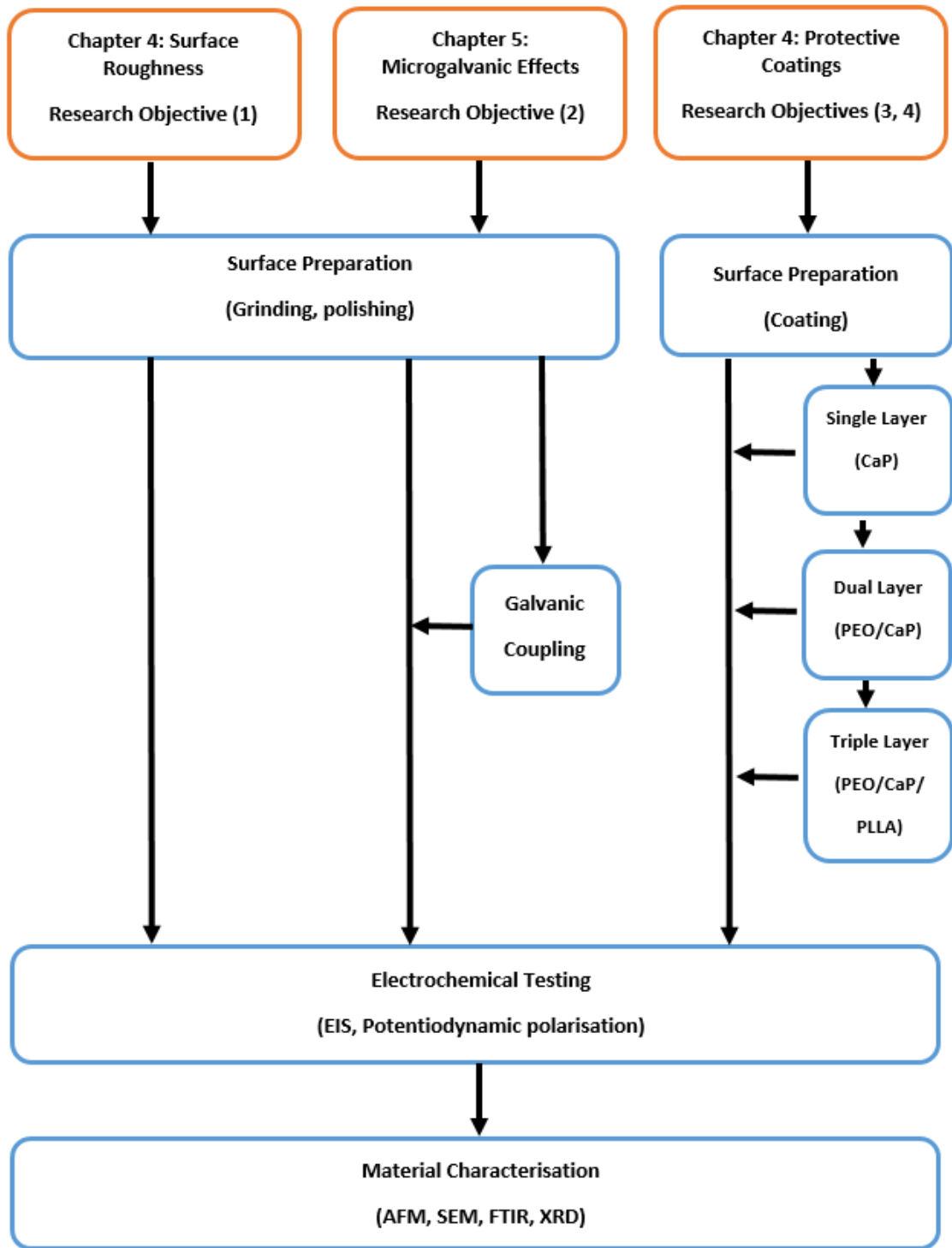


Figure 3.1 Outline of the methods used to fully describe degradation behaviour.

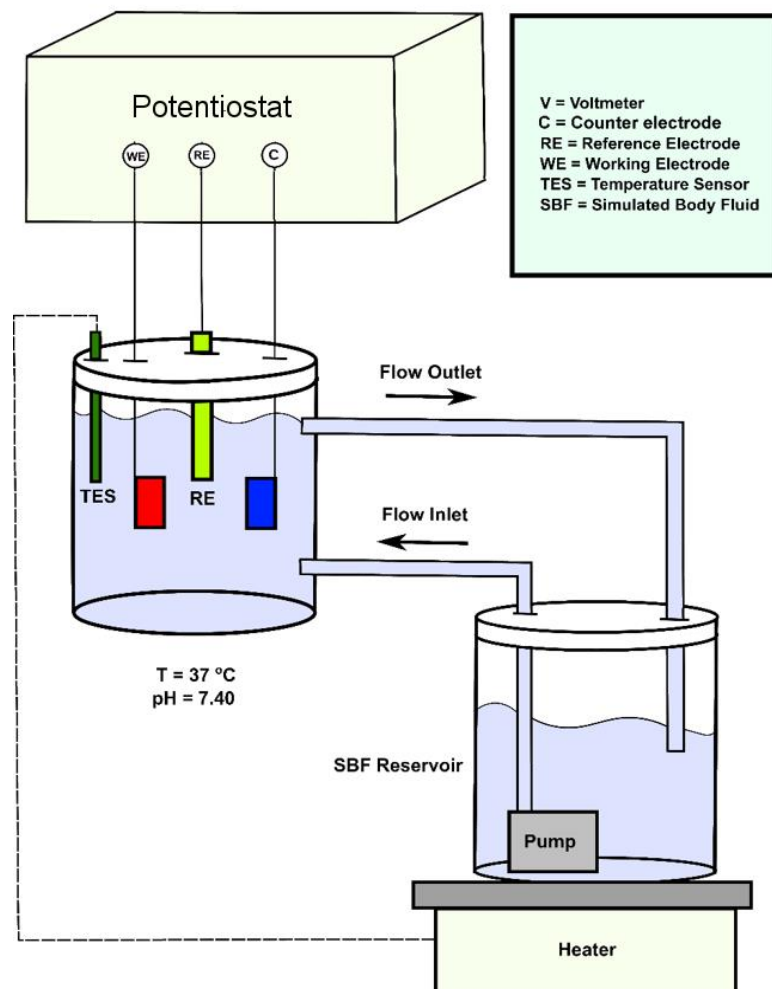


Figure 3.2 Experimental setup of the electrochemical degradation techniques.

Table 3.1
Composition of the SBF (Oyane, 2003).

Reagent	NaCl	NaHCO ₃	KCl	K ₂ HPO ₄ ·3H ₂ O	MgCl ₂ ·6H ₂ O	1 M HCl	CaCl ₂	Na ₂ SO ₄	TRIS buffer [†]
Amount (g/L)	8.036	0.352	0.225	0.230	0.311	40 (mL)	0.293	0.072	6.063

[†] TRIS buffer = tris(hydroxylmethylaminomethane)

3.2.1 Potentiodynamic Polarisation

Potentiodynamic polarisation is a technique that applies a sweeping potential from a value below the corrosion potential to one above. This work utilises a scan rate of 0.5 mV/s. This technique gives an estimation of the corrosion potential (E_{corr}) and corrosion current (I_{corr}), which are both valuable properties that give information on the corrosion behaviour of a material. Figure 3.6 shows an idealised Potentiodynamic polarisation curve. E_{corr} can be obtained by reading the potential at which the current approaches zero. I_{corr} can be obtained by extrapolating the linear regions of the cathodic and anodic curves, and measuring the current at the intersection.

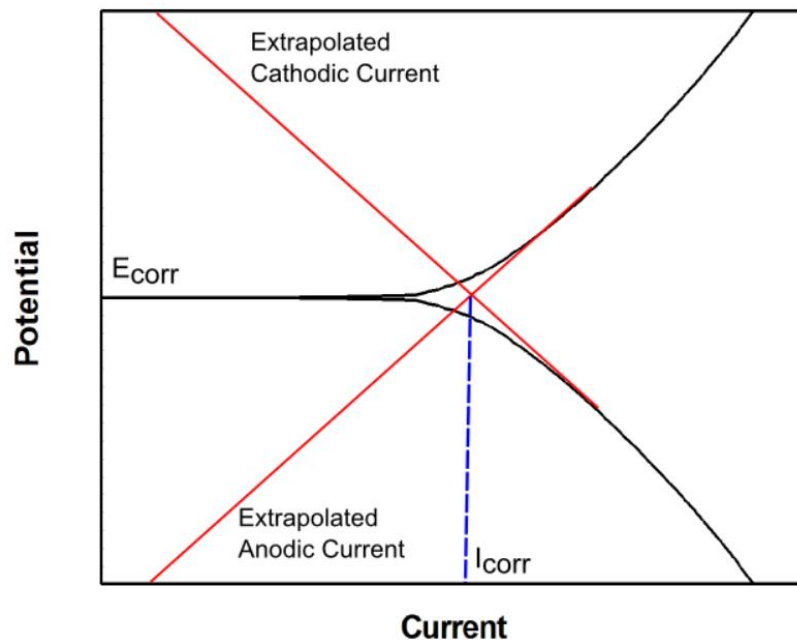


Figure 3.3 Ideal Potentiodynamic polarisation curve with marked points of importance.

3.2.2 Electrochemical Impedance Spectroscopy (EIS)

Electrochemical impedance spectroscopy (EIS) is a powerful tool that can be used to characterise electrochemical techniques in a non-destructive manner. This allows for multiple measurements over a long exposure time, and can be used to isolate and quantify the influences of the fundamental physical and chemical phenomena of the system. EIS utilises a small amplitude sinusoidal excitation to, typically between 5 – 50

mV. This work utilised an amplitude of 10 mV for all experimental work in order to be comparable to research previously reported in literature. The measured dc polarisation voltage (E_0) is then superimposed with a small amplitude sine wave of a particular frequency. This results in a current response superimposed on the dc current I_0 .

The impedance of the system is a complex quantity with a magnitude and phase shift. Thus, if a range of frequencies are applied, the impedance of the system as a function of frequency can be obtained. For typical electrochemical systems, this frequency range is $10^5 - 10^{-2}$ Hz. This can be expressed in either Cartesian or polar coordinates, given in equations 3.1 and 3.2, respectively.

$$Z(\omega) = Z'(\omega) + jZ''(\omega) \quad (\text{Cartesian expression}) \quad (3.1)$$

Where: Z = complex impedance

Z' = real part of the impedance

Z'' = imaginary part of the impedance

$j = \sqrt{-1}$

$$Z(\omega) = |Z(\omega)|e^{j\phi(\omega)} \quad (\text{Polar expression}) \quad (3.2)$$

Where: $|Z|$ = magnitude of the impedance

ϕ = phase shift

Expressing the plot of the real vs. the imaginary impedance gives the Nyquist plot, as shown in Fig. 3.3. The complex nature of the impedance arises as a result of the in-phase and out-of-phase components of the current due to the applied alternating potential. The Nyquist plot gives a quick overview of the data, and allows for some qualitative interpretations. However, this representation loses the frequency data unless the values are labelled on the curve itself. Plotting the absolute impedance and phase shifts gives a Bode plot, as shown in Fig. 3.4. This representation gives a more complete presentation of the data, but is more difficult to visually compare between data sets.

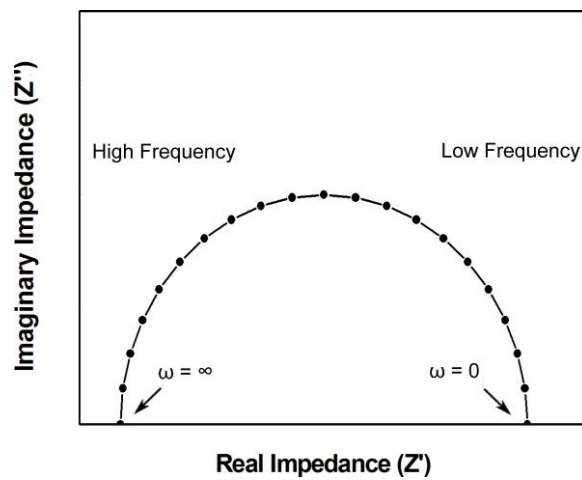


Figure 3.4 Typical Nyquist plot.

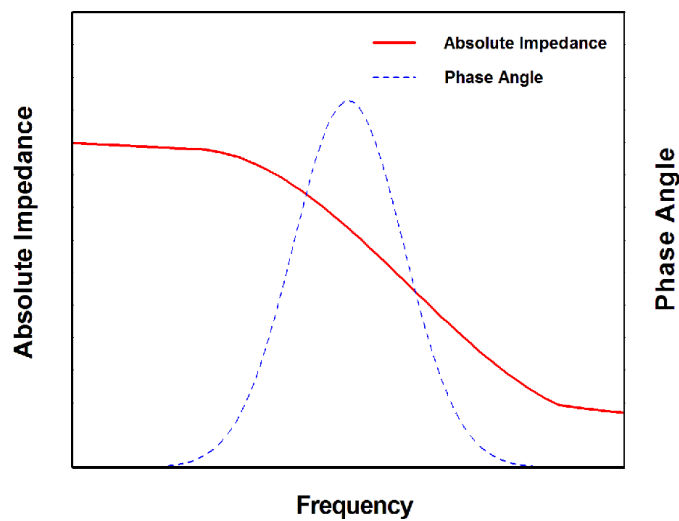


Figure 3.5 Typical Bode plot.

The frequency and impedance data can then be modelled using an equivalent circuit, where each of the elements in the circuit represents a physical or chemical process. This gives information on which processes are most significant in a particular system, as well as how they change over time. Equivalent circuit modelling of the EIS results in this work was done using ZSimpWin V. 3.21 software.

3.2.3 Galvanic coupling

For the micro-galvanic degradation investigation described in Chapter 5, a pure Mg and β -phase sample of equal surface area were galvanically coupled through a zero resistance ammeter in SBF at 37 °C and pH 7.40, as shown in Fig. 3.7. The samples were mounted in a resin, with an equal exposed surface area of 1 cm², and separated by a distance of 3 cm.

This setup simulates the microgalvanic effect between the two phases of interest (the primary α matrix and secondary β precipitate). A complete circuit causes the β phase to be cathodically protected by the anodic α matrix. By comparing the *in vitro degradation* behaviour of the coupled materials with an uncoupled control, insights into the relationship between the cathodic and anodic phases can be obtained.

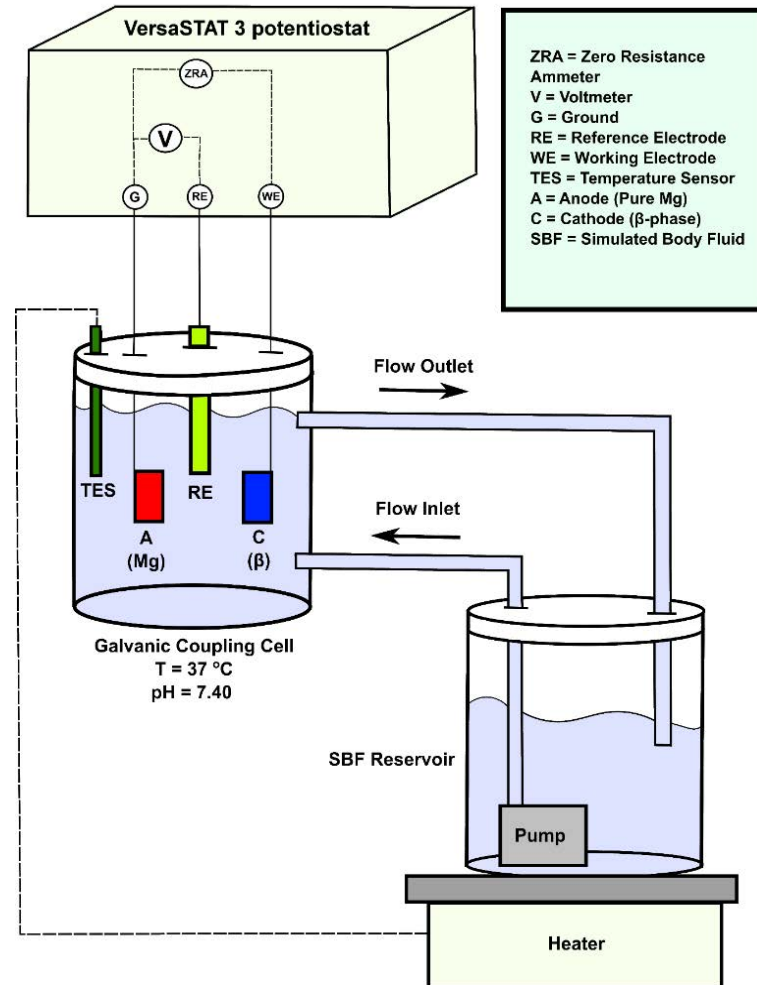


Figure 3.3 Experimental setup of the galvanic coupling.

3.3 Materials Characterisation

A range of techniques were utilised to characterise the metal samples and their protective coatings, both prior to and following degradation. Coating thicknesses were measured using a model Dual Scope thickness gauge, with a precision of $\pm 0.1 \mu\text{m}$. The coating and degradation morphology was examined using a Jeol JSM5410L scanning electron microscope (SEM). Samples were gold coated prior to examination to eliminate charging effects. The functional groups were determined using Fourier transform infrared (FTIR) spectroscopy analysis (Perkin Elmer spectrum 100 FTIR spectrometer). FTIR analysis was conducted in the spectral range of $1800 - 500 \text{ cm}^{-1}$, with measurements taken every 1 cm^{-1} . XRD was done using a Siemens D5000

Diffraction (XRD) theta-2 theta goniometer with a copper anode x-ray tube, fixed slits, monochromator and a forty position sample changer. The AFM is an NT-MDT NTEGRA, a high-resolution, low-noise scanning probe microscope with integrated analysis software.

3.4 Coatings

Chapter 6 focusses on the development of partially protective coatings to further enhance the long term *in vitro* degradation behaviour of Mg. Three coating types were utilised: plasma electrolytic oxidation (PEO), calcium phosphate (CaP), and poly(L-lactic acid) (PLLA). The specific coating parameters of each are described below.

CaP was electrochemically deposited on the substrate. The coating solution contained $\text{Ca}(\text{NO}_3)_2$, 0.06 M $\text{NH}_4\text{H}_2\text{PO}_4$ and 30 % v/v ethanol. Coating was carried out under either a constant potential of -3 V or a pulsed-potential of -3/0 V with a 35 % duty cycle (10 ms ON and 18.5 ms OFF) for 60 minutes.

The polymer layer was poly(L-lactide acid) PLLA, ester terminated RESOMER® L206 S (Aldrich). The monomer was dissolved in the organic solvent, dichloromethane (DCM), at a concentration of 60 g/L. The PLLA/DCM solution was then applied liberally to the surface of the sample and spin coated to remove the solvent and polymerise the monomer. The spin coating was conducted in a two-step process. The first stage was at a rotational speed of 500 rpm for 10 s, and the second was at a rotational speed of 2000 rpm for 10s.

Chapter. 4 Influence of Surface Roughness on the Degradation and Passivation Behaviour of Mg Alloys

4.1 Introduction

Generally, the surface roughness plays a role on the degradation behaviour of metallic materials. It has been reported that an increase in the surface roughness of stainless steels increases the pitting susceptibility (Sasaki and Burstein, 1996; Hong and Nagumo, 1997; Zuo et al., 2002) and general degradation rate (Shahryari et al., 2008). A similar trend has been reported for other metals, such as copper (Li and Li, 2006), and titanium-based alloys (Cabrini et al., 1997). However, the literature on the effect of surface roughness on the degradation behaviour of Mg and its alloys is limited. Interestingly, the only work by Alvarez et al. (2010) on AE44 Mg alloy is in contrast to the trend reported for other metallic materials. Based on immersion test results, the authors (Alvarez et al., 2010) reported that the general degradation decreased as the alloy's surface roughness increased. Further they reported that the polished alloy allowed greater initial pitting and higher pitting volume than the semi-polished alloy. Typically, the general and localized degradation behaviour of alloys would depend on their passivation behaviour. Hence, it is important to know the passivation behaviour of Mg alloys with different surface finish to correlate the surface roughness to their general degradation and pitting tendency.

Furthermore, while the many aspects of the *in vitro* degradation behaviour of AZ91 have been studied (Xin et al., 2007; Kannan and Singh, 2010; Gu et al., 2010a), there has been no work done to investigate how surface roughness plays a role on the localised degradation behaviour under physiological conditions. This is particularly relevant for biodegradable implants, since after undergoing localised degradation such as pitting the mechanical stress during service can potentially cause the implant to fail prematurely. Pits can act as stress risers, which allow the propagation of cracks due to stress corrosion cracking and/or hydrogen embrittlement (Winzer et al., 2005; Kannan and Dietzel, 2012).

In this chapter, the degradation behaviour of AZ91 Mg alloy was studied using electrochemical techniques, such as potentiodynamic polarisation and electrochemical

impedance spectroscopy, especially to understand the passivation behaviour of the alloy with different surface roughness, in both NaCl and SBF.

4.2 Materials and Methods

Sand-cast AZ91 Mg alloy was used as the test material in this study. The chemical composition of the alloys are given in Table 4.1. The AZ91 Mg alloy used in the SBF section was peak aged, i.e., solutionised at 400 °C for 24 h and allowed to air cool, peak-aged at 200 °C for 24 h and water quenched, a typical heat-treatment for achieving high strength. It should be noted that there is a small difference in the chemical composition between the two alloys, most notably in the iron concentration. As such, the degradation behaviour of the two alloys will not be directly compared.

For obtaining different surface roughness, the samples were ground/polished with different grits of silicon carbide (SiC) (i.e., 320, 600 and 1200) and 3 µm diamond paste. Following the grinding/polishing, the samples were rinsed and ultrasonically cleaned in acetone, and then rinsed with ethanol and dried. The degradation behaviour of the alloy was studied using electrochemical techniques as described in Chapter 3.

Table 4.1
Chemical composition (wt. %) of the AZ91 alloy tested in 3.5 % w/v NaCl.

Test Environment	Al	Zn	Mn	Si	Fe	Mg
3.5 % NaCl	9.18	0.78	0.20	0.01	0.002	Bal.
SBF	8.84	0.61	0.18	0.02	0.02	Bal.

4.3 Results and Discussion

4.3.1 *Influence of surface roughness in 3.5 % NaCl*

The AFM images for the different surface finishes are shown in Fig. 4.1. It was clearly evident that the surface roughness of the alloy decreased as the grit size of the grinding paper used was increased. The measured surface roughness and standard deviation are

listed in Table 4.2. As expected the standard deviation in the surface roughness values decreased as the surface of the alloy became smoother.

Table 4.2 Surface roughness (S_a) of AZ91 Mg alloy with different surface finish (N=3).

Sample Finish	S_a (nm)	Standard Deviation (nm)
320 SiC	430	183
600 SiC	248	86
1200 SiC	145	42
3 μ m Diamond-paste	80	21

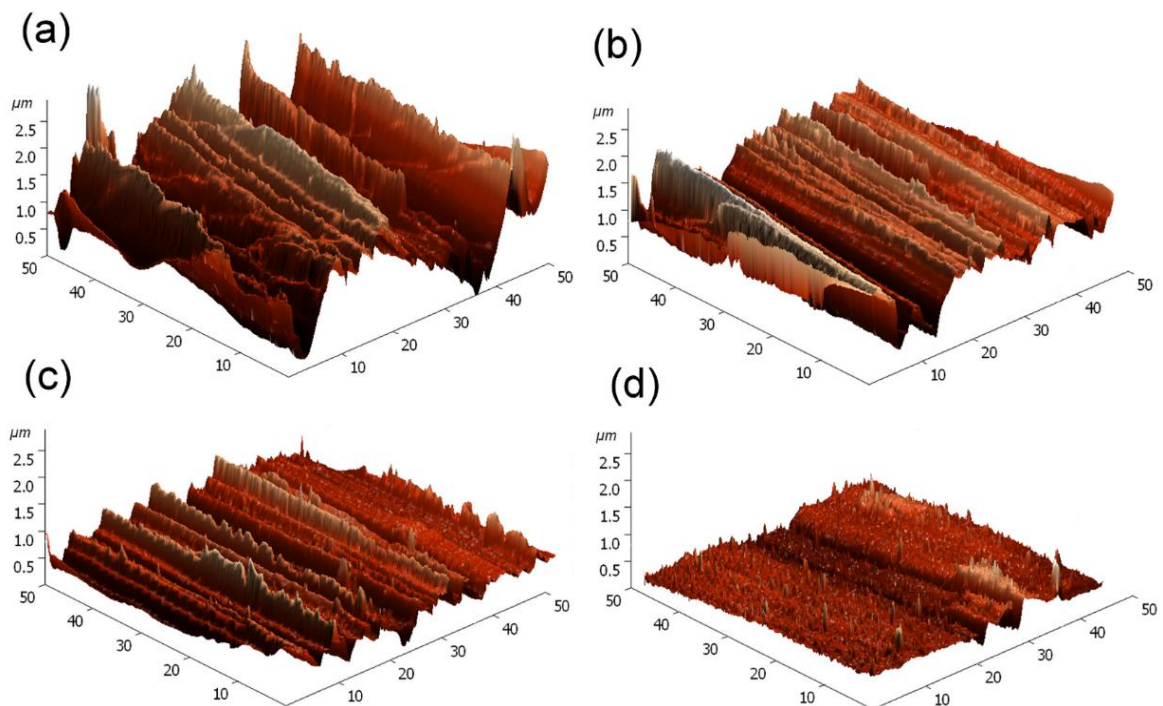


Figure 4.1 Surface topography of AZ91 Mg alloy ground/polished up to (a) 320 grit SiC; (b) 600 grit SiC; (c) 1200 grit SiC; and (d) 3 μ m diamond paste.

Fig. 4.2 shows the Nyquist plots of the alloy with different surface roughness tested in chloride-containing environment. In the SiC ground samples, a similar behaviour was observed i.e., a high frequency capacitive loop and low frequency inductive loop. It is reported in literature that the high frequency capacitive loop corresponds to the charge transfer and film effect (Guo et al., 2005; Zucchi et al., 2006) and the low frequency inductive loop indicates pitting of the alloy (Jin et al., 2007). The inductive loop arises as a result of relaxation of absorbed species on the surface due to the pitting corrosion itself, reducing the overall resistance. Interestingly, the diamond-paste polished alloy showed one capacitive loop at high frequency and another depressed capacitive loop at medium frequency. Moreover, the alloy showed no evidence of an inductive loop, which suggested that the sample with smooth surface has not undergone pitting.

It is reported in the literature that for rare-earth containing Mg alloys, an observation of a second capacitive loop in the mid frequency is related to the relaxation of mass transport through the degradation product layer, or in other words, suggests the presence of a protective film (Zucchi et al., 2006). It also means that the absence or lack of evidence of the second capacitive loop in the mid frequency is an indication of scarcely/no protective film. Although the formation of Mg hydroxide via the reaction: $2Mg + 2H_2O \rightarrow Mg(OH)_2 + H_2$, is plausible under different surface roughness conditions, the formation of a continuous protective film would be higher on a smooth surface alloy than on an irregular surface. Hence, the alloy with relatively high surface roughness showed no evidence of the second capacitive loop, but instead showed an inductive loop in the low frequency indicative of pitting. In the case of the low surface roughness alloy, the evidence of depressed second capacitive loop and the non-existence of low frequency inductive loop suggested that smooth surface alloy exhibits higher passivation tendency and pitting resistance than the high surface roughness alloy.

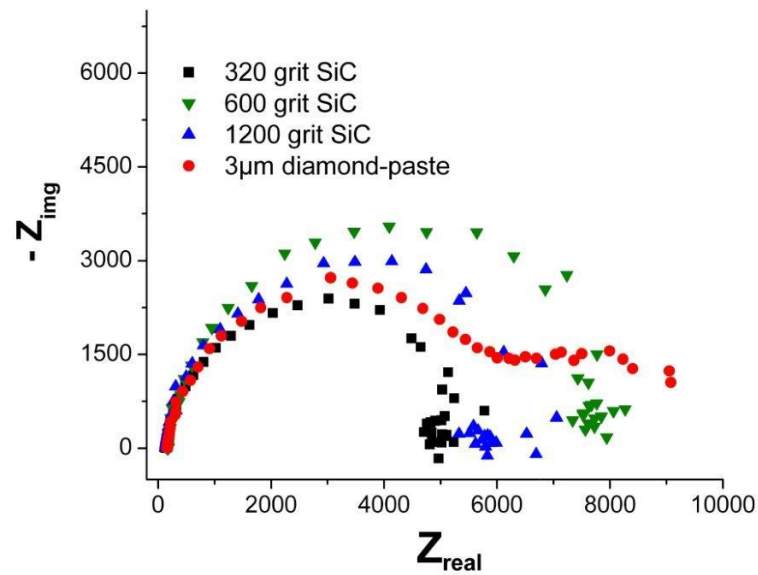


Figure 4.2 Nyquist plots of AZ91 Mg alloy, with different surface roughness, tested in 0.5 wt. % NaCl.

The polarisation curves of AZ91 alloy, with different surface roughness, tested in chloride-containing solution are shown in Fig. 4.3. The electrochemical degradation parameters from the polarisation curves are listed in Table 4.3. The corrosion potential (E_{corr}) of the alloy shifted towards the noble direction as the surface roughness decreased. Notably, the corrosion current (i_{corr}) decreased as the surface roughness decreased. However, there was no significant difference in the cathodic current within the samples having different surface roughness, which suggested that the shift in the E_{corr} and the difference in i_{corr} were solely due to the anodic behaviour of the alloy. The alloy with the highest surface roughness showed a sharp increase in the anodic current just above the E_{corr} . This phenomenon (i.e., sharp increase in the anodic current) was an indication of pitting, and in this case the pitting potential was pinned with the E_{corr} .

Interestingly, as the surface roughness decreased the alloy revealed a passive-like behaviour before a sharp break-down. It was noticed that the passive-potential region (E_{pass} , the difference between the corrosion potential and the break-down potential, E_{bd}) increased when the surface roughness of the alloy decreased. Hence, the alloy with the lowest surface roughness showed a passive-potential region of about 79 mV, whereas the highest surface roughness alloy showed no evidence of passive region. Although the

passivity could be mainly due to the formation of Mg hydroxide, the presence of aluminium (forms aluminium oxide in aqueous environment) in the alloy may also have some influence on the passivation behaviour.

Table 4.3

Electrochemical degradation parameters of AZ91 alloy (with different surface roughness) obtained from potentiodynamic polarisation curves (N=3).

Surface finish	i_{corr} ($\mu\text{A}/\text{cm}^2$)	E_{corr} ($\text{V}_{\text{Ag}/\text{AgCl}}$)	E_{bd} ($\text{V}_{\text{Ag}/\text{AgCl}}$)	E_{pass} ($\text{mV}_{\text{Ag}/\text{AgCl}}$)
320 grit SiC	6.92	-1.447	-1.447	0
600 grit SiC	4.79	-1.427	-1.392	35
1200 grit SiC	3.73	-1.418	-1.362	56
3 μm Diamond-paste	2.19	-1.378	-1.299	79

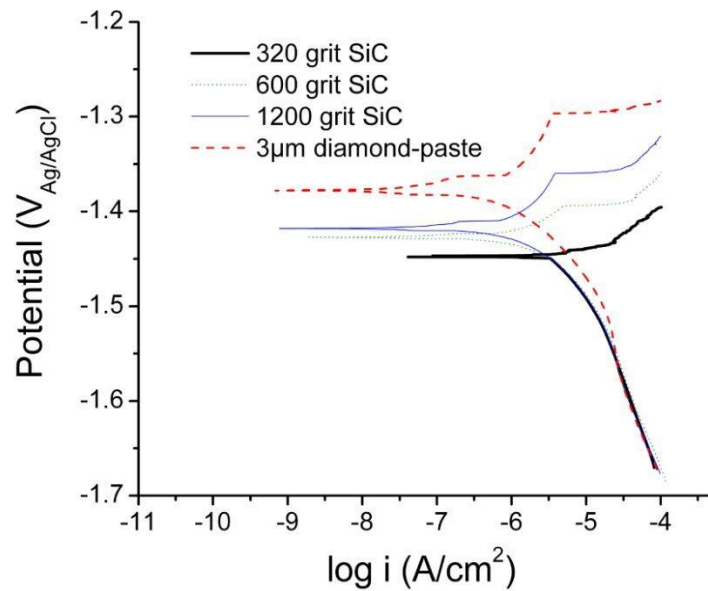


Figure 4.3 Potentiodynamic polarisation curves of AZ91 alloy, with different surface roughness, tested in 0.5 wt. % NaCl.

The SEM images of the samples immersed in chloride-containing solution at the open circuit potential for 24 h (Plate 4.1) clearly revealed that the alloy with the highest surface roughness underwent high pitting degradation, whereas the alloy with the lowest surface roughness showed no evidence of localized attack. The alloy having mid-range surface roughness did show some evidence of pitting degradation, however substantially lower than in the alloy with highest surface roughness.

Interestingly, the SEM images of galvanostatically-held alloy revealed a large number of pits, irrespective of their surface roughness (Plate 4.2). Alvarez et al. (2010) also found pitting in both polished and semi-polished AE44 Mg alloy. Interestingly, they reported that the density of pitting was relatively higher in polished alloy as compared to semi-polished alloy. In fact, a closer look at the SEM images of galvanostatically-held alloy, suggested that the alloy with lowest surface roughness exhibits a slightly higher number of pits as compared to the alloy with highest surface roughness. However, Alvarez et al. (2010) observed larger pits in semi-polished alloy as compared to polished alloy.

In order to understand the differences in the pitting behaviour of Mg alloy with different testing methods, the fundamental degradation mechanism of Mg has been reviewed. It is well documented in the literature that Mg dissolution increases the local pH at cathodic sites of the sample, which tends to facilitate degradation-product film, or in other words passivates the alloy (Song and Atrens, 2003). However, in the presence of chloride ions the passive film on Mg breaks down, causing pitting degradation. Alvarez et al. (2010) conducted the testing in 3.5% NaCl solution, which is not different to the test solution in this study; however it should be noted that they have aerated the solution throughout the experiment. Although oxygen (in air) has no significant influence on the degradation behaviour of the Mg (Makar and Kruger, 1993), the stirring effect caused by aeration could reduce the local pH change and consequently affect the passivation tendency of the alloy. Hence, they observed pitting degradation even in the polished alloy under immersion testing. However, in the case of the galvanostatically-held alloy, the anodic-current was high enough to break the passive film of the alloy under all surface roughness (refer Fig. 4.3), and hence pitting degradation was observed in all the samples irrespective of their surface roughness.

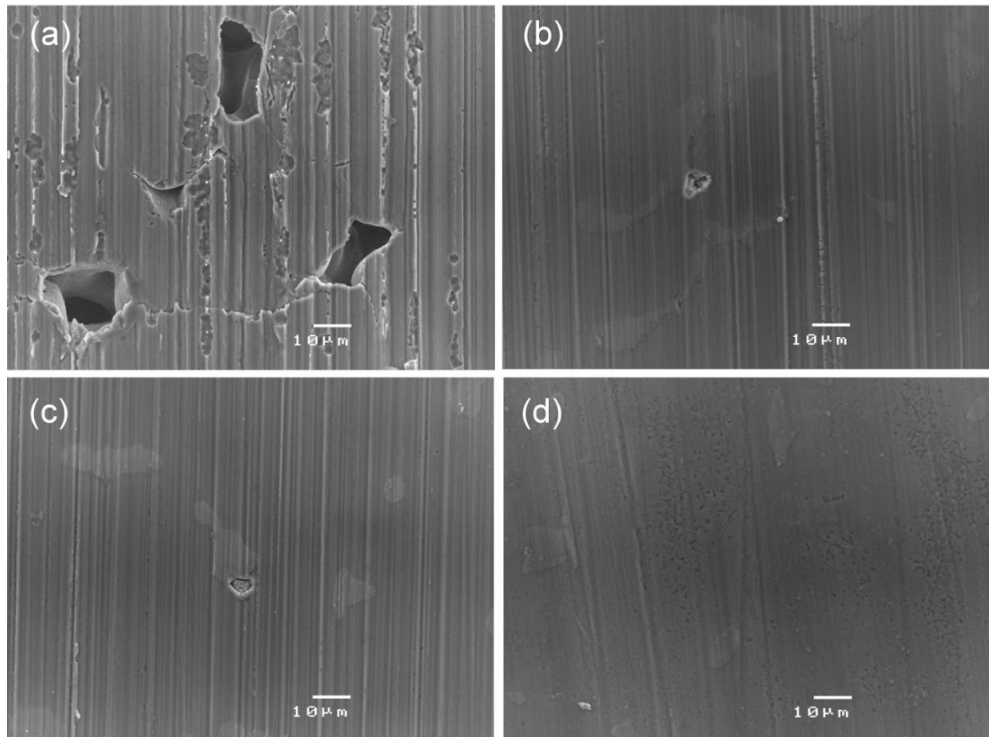


Plate 4.1 SEM images of AZ91 Mg alloy ground/polished (for different surface roughness) up to (a) 320 grit SiC; (b) 600 grit SiC; (c) 1200 grit SiC; and (d) 3 μ m diamond-paste, and immersed in 0.5 wt. % NaCl for 24 h.

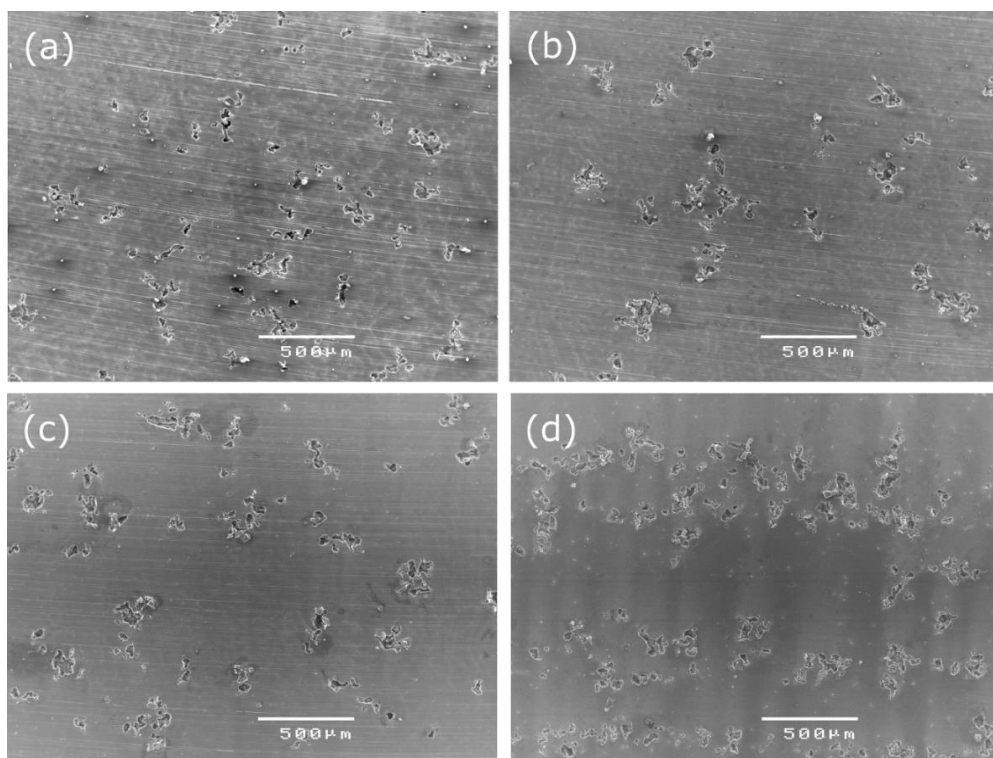


Plate 4.2 SEM images of AZ91 Mg alloy ground/polished up to (a) 320 grit SiC; (b) 600 grit SiC; (c) 1200 grit SiC; and (d) 3 μ m diamond-paste, after galvanostatic testing.

4.3.2 *Influence of surface roughness in SBF*

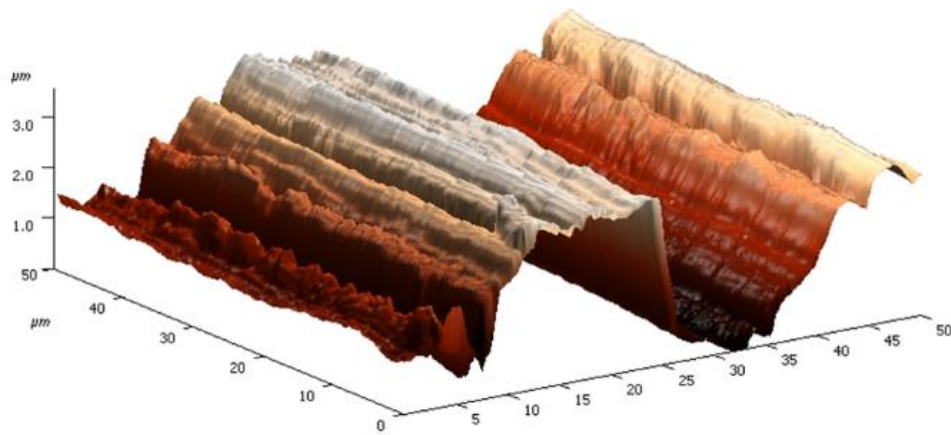
The surface topography of the smooth and rough surfaces of the test samples obtained from the AFM analysis is shown in Fig. 4.4, and the average surface roughness (S_a) data is given in Table 4.4. Since the previous section showed that there is a direct correlation between surface roughness and degradation behaviour, only the highest and lowest roughnesses have been examined in this section. Fig. 4.5 shows the EIS plots for the alloy immersed for different periods (1-12 h). It can be seen that for the rough surface at low immersion period (1-2 h), the plots show two capacitive loops; at high and mid frequencies. The longer immersion periods (3-12 h) show no mid frequency loop, but do show low frequency inductive loops. High frequency capacitive loop has been reported to correspond to charge transfer and passive film effects (Guo et al., 2005; Zucchi et al., 2006). The existence of a mid frequency capacitive loop suggests that the alloy is protected by degradation products/passive layer. Thus, the absence of this loop can either correspond to the complete lack of a passive film (such as for non-passivating materials), or that the film is scarcely protective.

This trend is also observed for the smoother surface, as shown in Fig. 4.5. However, the mid frequency capacitive loop is present until 4 h immersion. Longer immersion periods also produced an inductive loop in the low frequency. Inductive loops in the low frequency range have been reported to indicate pitting degradation (Jin et al., 2007). These loops only appeared following the disappearance of the mid frequency capacitive loops, which suggest that pitting initiates once there has been a breakdown of the passive layer. For the rougher sample, the inductive loop is slightly evident at 3 h immersion, but is well defined from 4 h onwards. Interestingly, for the polished sample, the inductive loop first appears at 4 h immersion time, though it is not well defined until 12 h immersion. Thus, pitting degradation initiates significantly sooner, and to a greater severity on the rougher surface when compared to the smoother surface. The second trend that is evident in these data is that the polarisation resistance (R_p) decreases with immersion time, which is apparent for both the smooth and the rough surfaces.

Table 4.4
Surface roughness (Sa) data for AZ91 Mg alloy (N=3).

Sample Finish	Sa (nm)	Standard Deviation (nm)
120 SiC	973	49
3 μ m Diamond-paste	22	10

(a) Rough (Sa = 973 nm)



(b) Smooth (Sa = 22 nm)

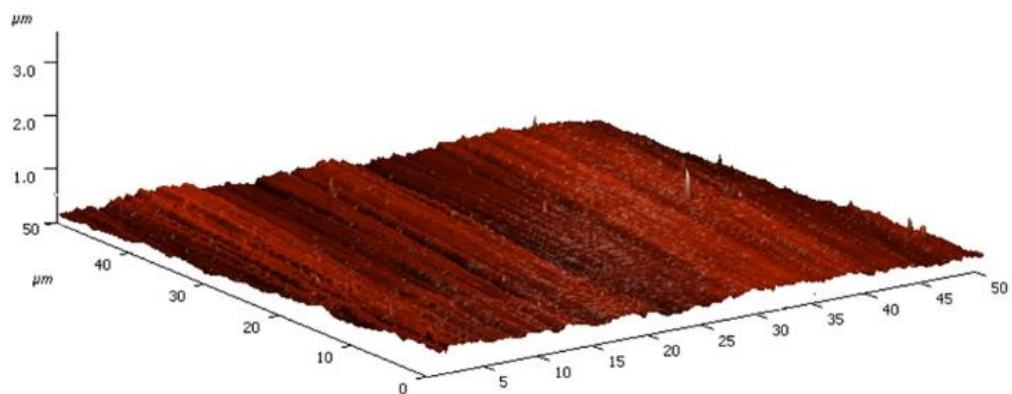


Figure 4.4 AFM images of AZ91 Mg alloy under two different surface finishes: (a) ground with 120 grit SiC paper, and (b) polished with 3 μm diamond paste.

The EIS data was modelled using an equivalent circuit as shown in Fig. 4.6, where R_s corresponds to solution resistance, CPE_{dl} the double layer capacitance, R_t the charge transfer resistance, and R_f and CPE_f represent the film effects (Walter and Kannan, 2011). To account for non-homogeneity of the system, constant phase elements were used in place of pure capacitors. The R_p (polarisation resistance) of smooth and rough samples are shown in Fig. 4.6, which was calculated by adding R_f and R_t (Jin et al., 2007). The highest polarisation resistances were found during the shortest immersion times (2 h for the rougher sample, and 3 h for the smoother) which correspond to the better passivation/degradation resistance.

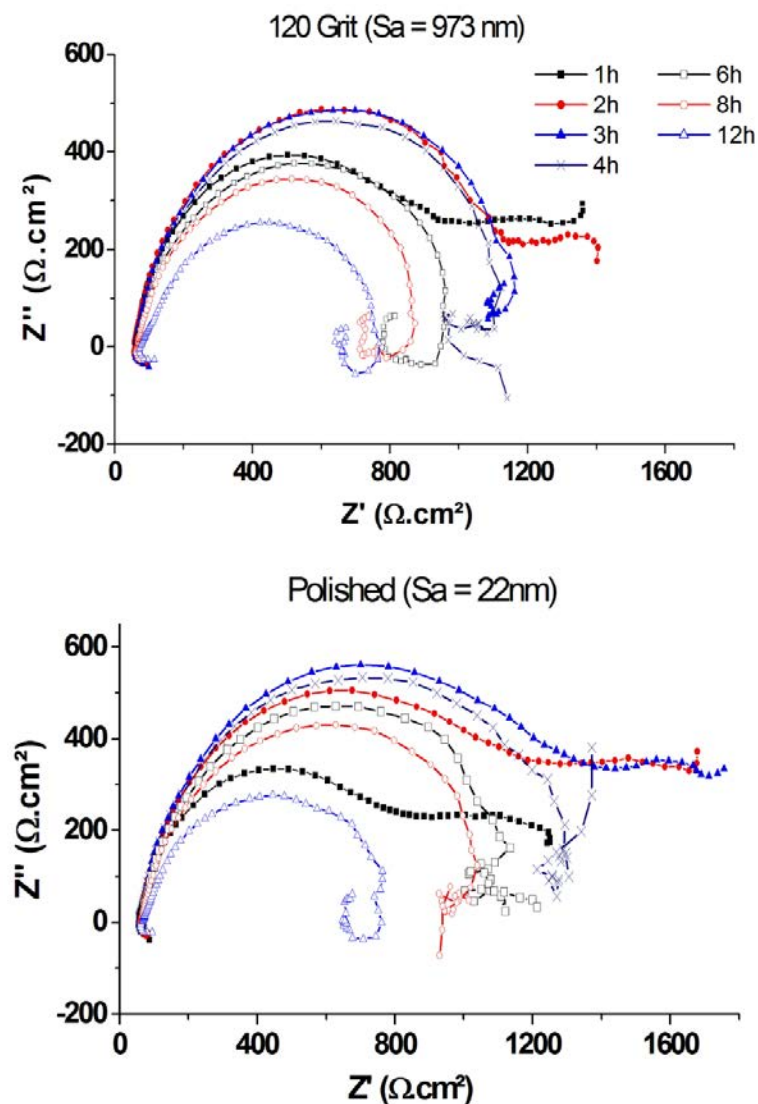


Figure 4.5 EIS plots for AZ91 Mg alloy immersed in SBF for varied immersion times.

This can be seen in Fig. 4.6 by the presence of the second mid-frequency capacitive loops at these times. Fig. 4.5 shows that R_p decreases after these times, due to the breakdown of the passive film, and the initiation of localised degradation. The primary difference between the two finishes was found in the film resistance of the alloy. The smoother sample showed a much larger R_f when compared to the rougher sample during early immersion. This difference decreased over time, but was enough to cause a shift in the pitting initiation time.

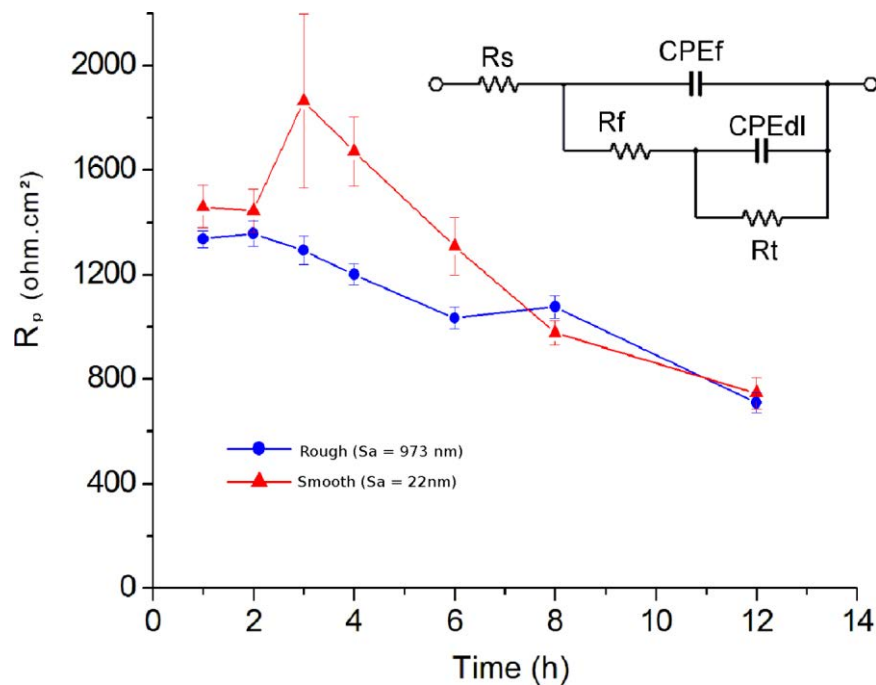


Figure 4.6 Polarisation resistance vs. time for AZ91 Mg alloy immersed in SBF, and the applied equivalent circuit model.

In order to understand the mode and degree of degradation, samples immersed for 2, 6, and 12 h in SBF were analysed using SEM. It can be seen from Plate 4.3 that for 2 h immersion time, both surface finishes show only some signs of general degradation, but no pitting degradation. This is in agreement with the EIS data, which had a distinct lack of a low frequency inductive loop at this immersion period. However, at 6 h immersion, Plate 4.3 shows that for the 120 grit finish, there are areas that display signs of heavy

localised attack. The EIS data showed a breakdown of passivation at this time, as well as a low frequency inductive loop, highly indicative of pitting attack. For the polished surface, Plate 4.3 shows only small pits. This indicates that pit initiation had only just begun, again in agreement with the EIS data. At 12 h immersion, both the rough and smooth surfaces show signs of heavy pitting degradation. The pitting degradation area is much more pronounced and developed in the rough surface alloy when compared to the smooth surface alloy.

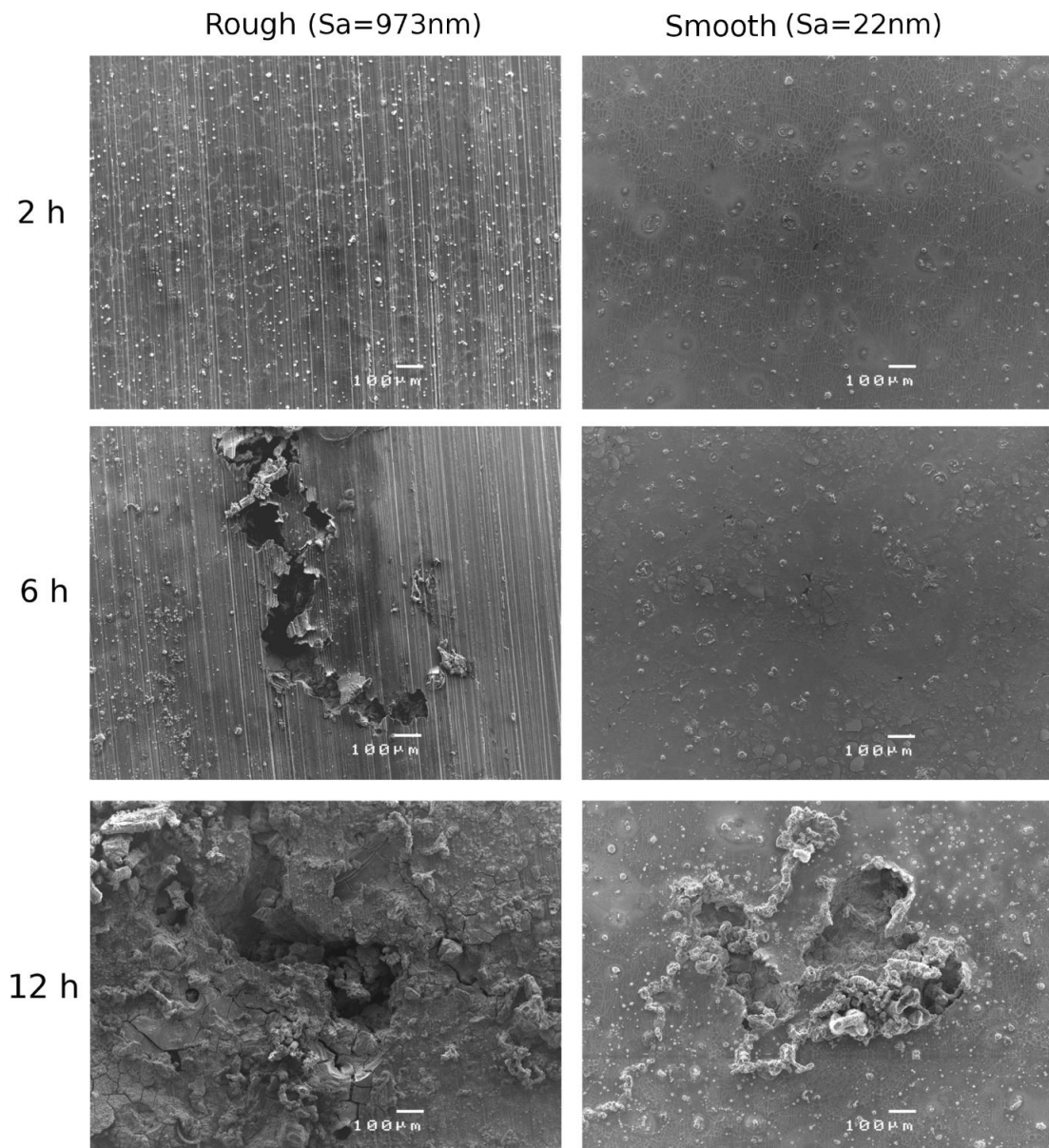


Plate 4.3 SEM images of the AZ91 Mg alloy immersed in SBF for 2, 6 and 12 hours.

The rougher surface sample had relatively deep valleys when compared to the smooth surface sample, which would have caused local pH drop as Mg dissolution occurred. Thus, the smoother surface was conducive to homogenous passivation across the whole surface, while the rough surface has areas of increased passive layer breakdown.

For low immersion times (1-2 h), the R_p value of the smooth surface sample was ~10% higher than the rough surface sample. For these low immersion times, passivation had not occurred across the whole surface. The lower R_p for the rough surface during this time can be attributed to a slight increase in surface area not accounted for due to a more varied surface topography. The largest disparity between the R_p values (30% variance) occurred at 3 h immersion time, which suggests that the passive film on the rough surface started to breakdown.

From 3 h onwards, the R_p values of the samples decreased until it reached a minimum at 12 h immersion time, which was the longest time the samples were examined in this study. This corresponds to an overall decrease in the R_p of 60% for the smooth surface, and 47% for the rough surface. The passive layer is attacked by chloride and hence as the immersion time increases, the rate of passive layer removal overtakes the repassivation, and the protective layer becomes less protective. Similarly, as the alloy degrades, more unprotected area is exposed, further increasing the degradation rate.

By comparing the effect of the individual resistances in the equivalent circuit (Fig. 4.6), it was observed that the main variation between the two samples was only in the film resistance. Once this effect was no longer the dominant source of resistance, the R_p values converged to a similar value ($728 \pm 77 \Omega \cdot \text{cm}^2$) for the two surfaces. Interestingly, the film effects at low immersion times play a critical role on the degradation behaviour of the material. If only the long term immersion data were to be observed, it would seem that surface roughness only plays a very minor role on degradation rate. However, the key point to be noted is the low frequency inductive loops in the EIS plots, which are indicative of localised degradation of the alloy. These loops first appeared at 3 h immersion time for the rough surface, and 4 h for the smooth. It was noticed that during these times the corresponding R_p values began to decrease from the maximum. While these times represent the points at which the loops first appeared, there were not well defined until 4 h and 12 h for the rough and smooth surfaces, respectively. This suggests that not only does pitting degradation occur sooner

for the rougher surface, it also occurs much more severely. Thus it can be stated that although the overall degradation resistance is similar between the two surface conditions, the localised attack behaviour is significantly different. This agrees with the previously reported results in chloride-containing solution, where the pitting degradation behaviour of the alloy was much more severe on rougher surface when compared to smoother surface.

The SEM images confirm the results presented in the electrochemical tests. Localised attack initiated much sooner on the rougher surface than on the smoother surface, and to a higher degree. Neither surface showed any signs of degradation at 2 h immersion. At 6 h, the rough surface showed significant localised degradation. It could also be seen that the pits had coalesced into a much larger area of degradation. The smooth surface however, showed only signs of very small pits, indicating that the localised degradation had just initiated. At 12 h, these pits size had increased, but there were still areas that showed no signs of degradation. The rough surface, however, showed much larger and deeper pits, and the surrounding areas also showed signs of generalised degradation.

A phenomenological model for the localised degradation process of the smooth and the rough surfaces is shown in Fig. 4.7. Stage 1 shows the two surfaces prior to any degradation (not to scale). The rougher surface has areas of deep valleys, whereas the smooth surface is relatively flat. Once the samples are immersed in the SBF, passive layers form on the samples (Stage 2), which is a rapid process. In Stage 3, the chloride ions react with the passive layer and causes dissolution of the passive layer. Due to the deep valleys in the rough surface, local pH drop occurs during this process. However, for the smooth surface such as pH drop does not occur and as a consequence the repassivation is partially offsetting the passive layer breakdown, which slows down the dissolution of the passive layer. In Stage 4, the pits initially formed in the earlier stages on the rough surface have grown, whereas they are only just initiating on the smooth surface due to long exposure period. Stage 5 shows the surfaces after 12 h degradation. The rough surface has undergone significant general and localised degradation, as shown in Plate 4.3. Conversely, the smooth surface has undergone primarily localised degradation, with some areas being still protected by passive layer remnants.

Due to the significant difference in the pit initiation and growth behaviour of the two surfaces, it is proposed that smoother surface alloy would be more beneficial than

rougher surface alloy. In fact, pitting degradation must be minimised in biodegradable Mg alloys to reduce the chance of premature implant failure due to stress corrosion cracking and/or hydrogen embrittlement (Kannan and Orr, 2011).

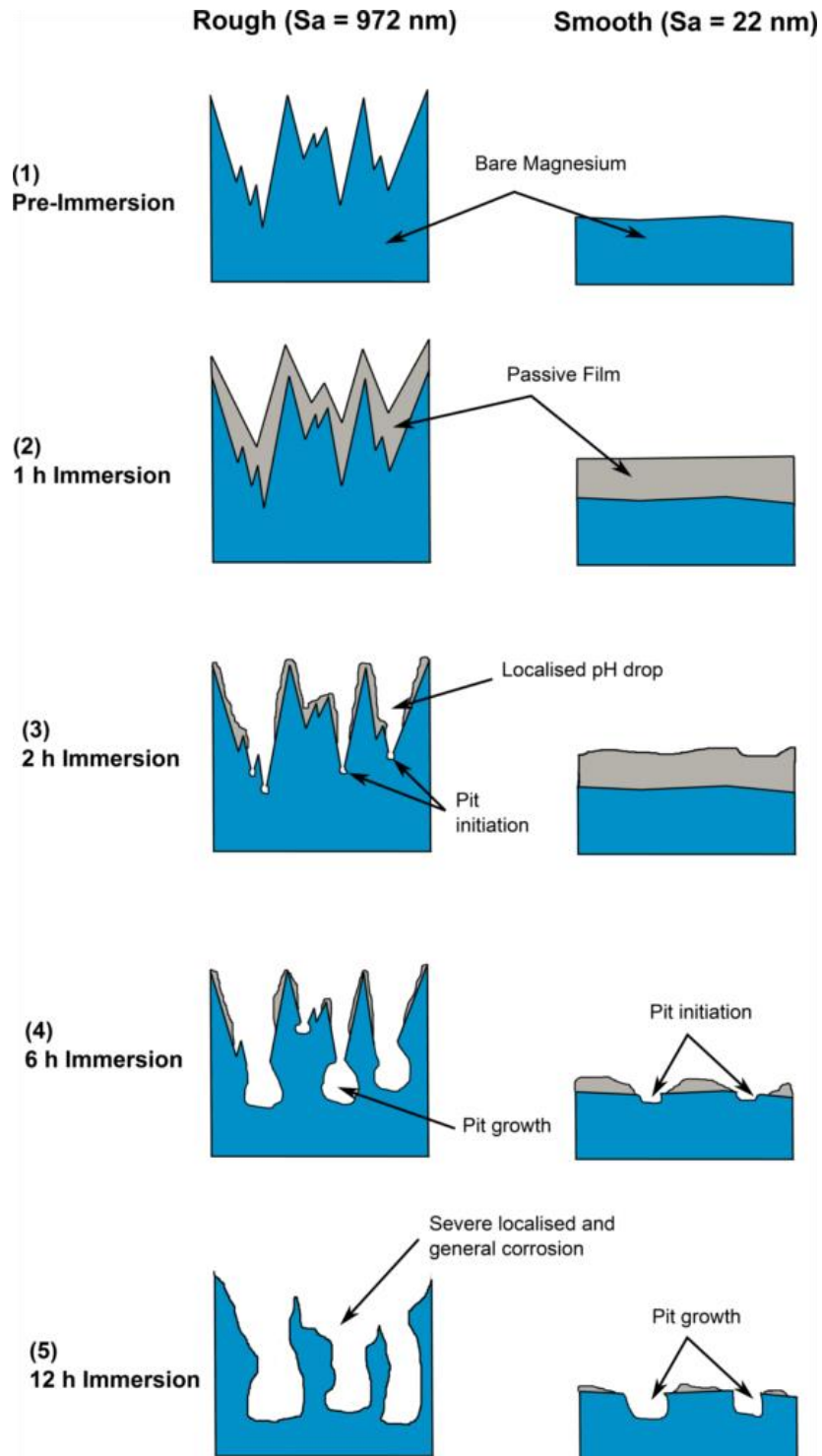


Figure 4.7 Phenomenological model of the localised degradation behaviour of a rough surface and a smooth surface of AZ91 Mg alloy.

4.4 Conclusions

The study clearly suggests that the surface roughness plays a critical role in the degradation behaviour of AZ91 Mg alloy in chloride-containing environment. The electrochemical experiments showed that an increase in the surface roughness of the alloy affects the passivation tendency and consequently increases the pitting susceptibility of the alloy. However, when the passivity of the alloy is disturbed then the influence of surface roughness on the pitting degradation susceptibility becomes less significant.

Although the surface roughness of AZ91 Mg alloy did not show any significant effect on its general degradation resistance under long-term exposure in SBF, it played a critical role on the localised degradation behaviour of the alloy. A rougher surface reduced the incubation time for pitting degradation of the alloy. Moreover, the severity of the localised degradation of the alloy was also high in the rough surface alloy as compared to the smooth surface alloy.

Chapter. 5 A Mechanistic in Vitro Study of the Micro-galvanic Degradation of Secondary Phase Particles in Mg Alloys

5.1 Introduction

While it is understood that secondary phase particles are cathodically protected by the Mg matrix, it is not clear how the degradation behaviour of the secondary phase particles changes once micro-galvanic effects are reduced i.e., via undermining or dissolution of the Mg matrix. This knowledge is critical in the development of Mg-based biomaterials in order to accurately predict in-service implant performance. Hence, in this study the effect of micro-galvanic degradation on β -phase (secondary phase particles commonly found in AZ series Mg alloys) was investigated under physiological conditions.

5.2 Materials and Methods

In this study, pure Mg and $\text{Mg}_{17}\text{Al}_{12}$ (β -phase) intermetallic sample were used since a significant amount of work has been done on the in vitro and in vivo behaviour of aluminium containing (AZ series) Mg alloys. β -phase sample was prepared by melting pure Mg and aluminium in a mixing ratio 56:44 (wt. %) at 750°C under argon gas atmosphere. The molten intermetallic sample was then cast in a preheated (250 °C) cast iron mould under protective SF_6 gas. The composition of the β -phase intermetallic was determined using inductively coupled plasma mass spectrometry (ICP) analysis, and is given in Table 5.1. X-ray diffraction (XRD) analysis on the sample was conducted using a Siemens D5000 diffractometer. Electrochemical testing, galvanic coupling and materials characterisation were done as described in Chapter 3.

Table 5.1
Chemical composition (wt. %) of pure Mg and β -precipitate.

Sample	Al	Zn	Mn	Si	Fe	Mg
Pure Mg	0.02	0.01	0.01	0.01	0.003	Bal.
β - phase	41.43	-	0.004	0.007	0.003	Bal.

5.3 Results

Fig. 5.1 shows the XRD analysis of the cast intermetallic product of Mg and aluminium mixture. The XRD spectra confirmed that the intermetallic corresponds to $Mg_{17}Al_{12}$, otherwise known as the β -phase of AZ series Mg alloys (Zhao et al., 2008; Lee et al., 2011).

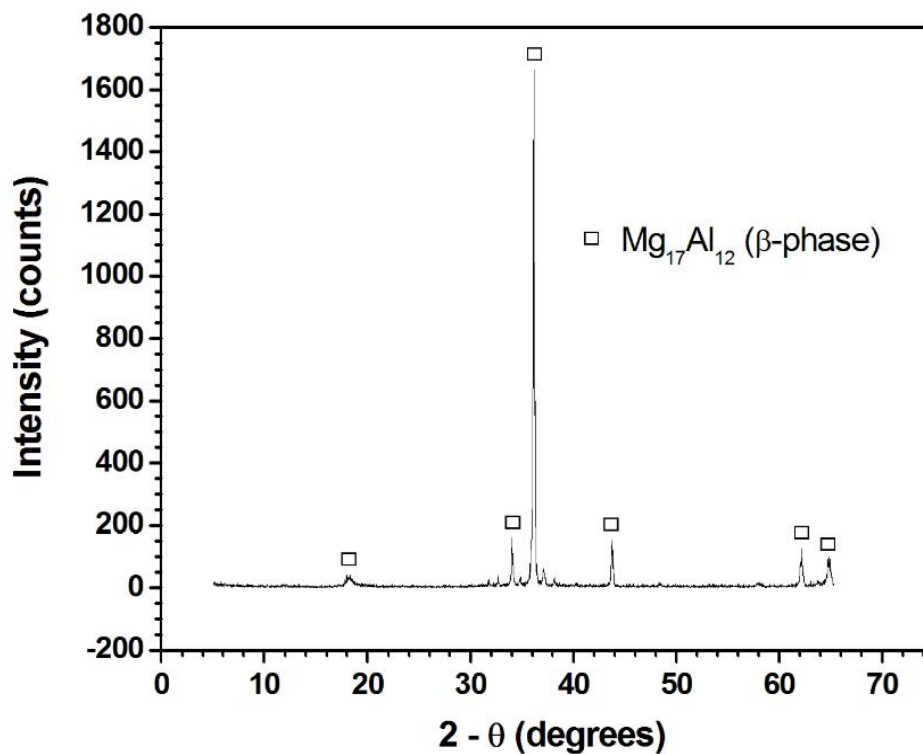


Figure 5.1 XRD pattern of the $Mg_{17}Al_{12}$ (β -phase).

The EIS results of pure Mg and β -phase immersed in SBF for different periods (2-24 h) are shown in Fig. 5.2. The Nyquist plots were modelled using an equivalent circuit model as shown in Plate 5.1. The elements correspond to the same physical phenomena as described in 4.3.2.

Initially, the pure Mg showed an R_P value of $195 \Omega \cdot \text{cm}^2$, whereas the β -phase showed $645 \Omega \cdot \text{cm}^2$, corresponding to a three-fold increase in the polarisation resistance. A two-tailed unpaired t-test between pure Mg and β -phase showed a p-value of 0.0011, a very significant difference. However, it was evident that this difference decreased over time; after 24 h, the R_P of pure Mg had increased to $945 \Omega \cdot \text{cm}^2$, while the R_P of β -phase was measured to be $925 \Omega \cdot \text{cm}^2$; a statistically insignificant difference ($p=0.9173$). SEM analysis shows that the pure Mg had undergone significant general degradation, with evidence of localised degradation (Plate 5.1a, b). However, the β -phase sample exhibited significant localised degradation (Plate 5.1c, d).

In order to investigate the effect of micro-galvanic degradation, the β -phase sample was galvanically coupled with pure Mg for 48 h. Fig. 5.4 shows the mixed potential and current density of the pure Mg and β -phase sample during the coupling. While the potential remained relatively stable at $-1.49 \text{ V}_{\text{Ag}/\text{AgCl}}$, the current showed a cyclical increase/decrease during the entire coupling period. Following the coupling, it was seen that the pure Mg has degraded significantly over this period, as expected. Also visible was a white powder layer that had formed on the surface of β -phase sample. Interestingly, this layer appeared to be thicker at the 24 h period as compared to the 48 h period. This can be attributed to the falling of particles from the white powder layer after a period of time. In fact, this was visually observed during testing, i.e., the white particles fell off the β -phase sample surface during the experiment, and had settled to the bottom of the cell.

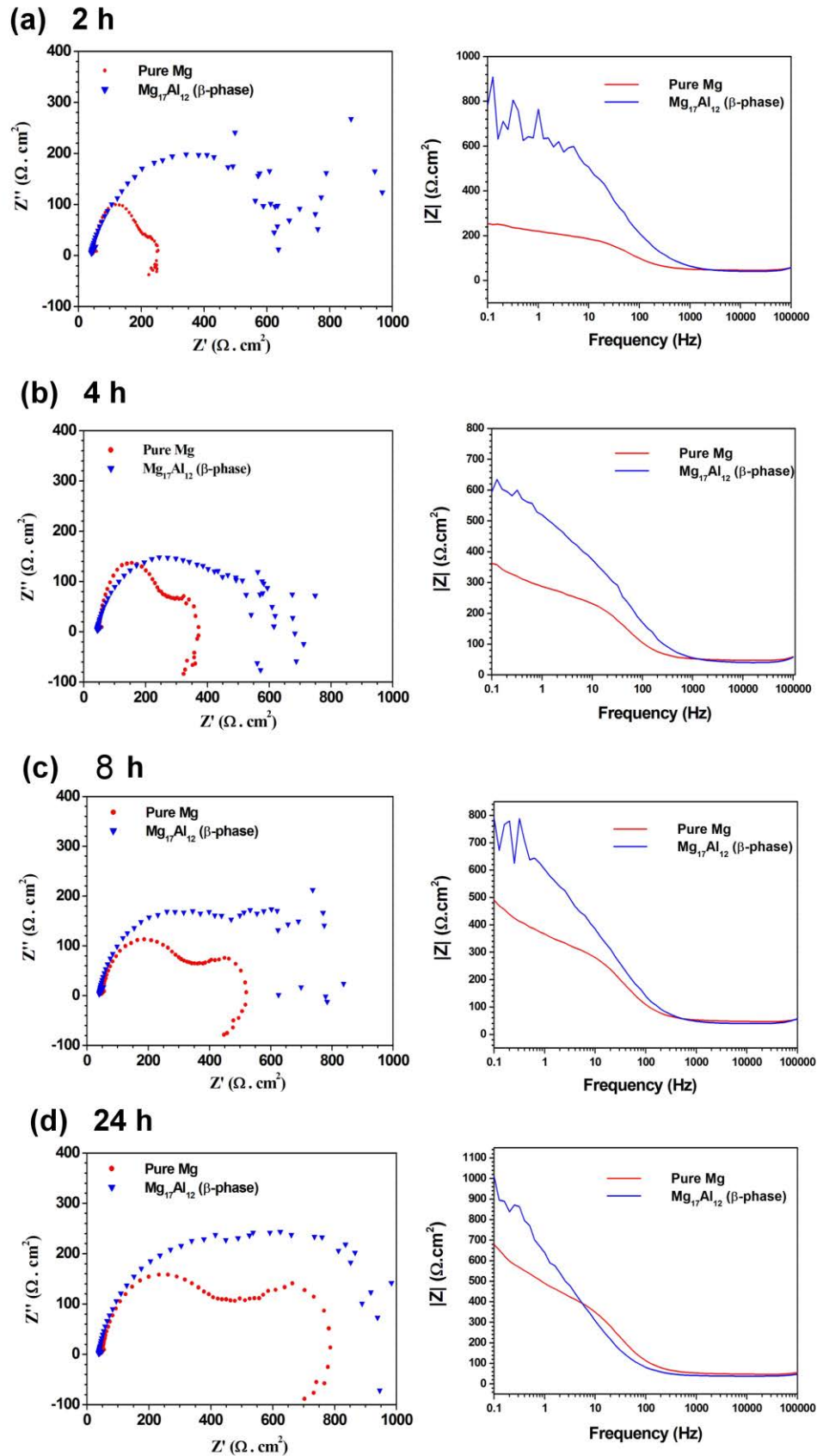


Figure 5.2 Nyquist and Bode plots of the pure Mg and β -phase immersed in SBF for (a) 2 h, (b) 4 h, (c) 8 h and (d) 24 h.

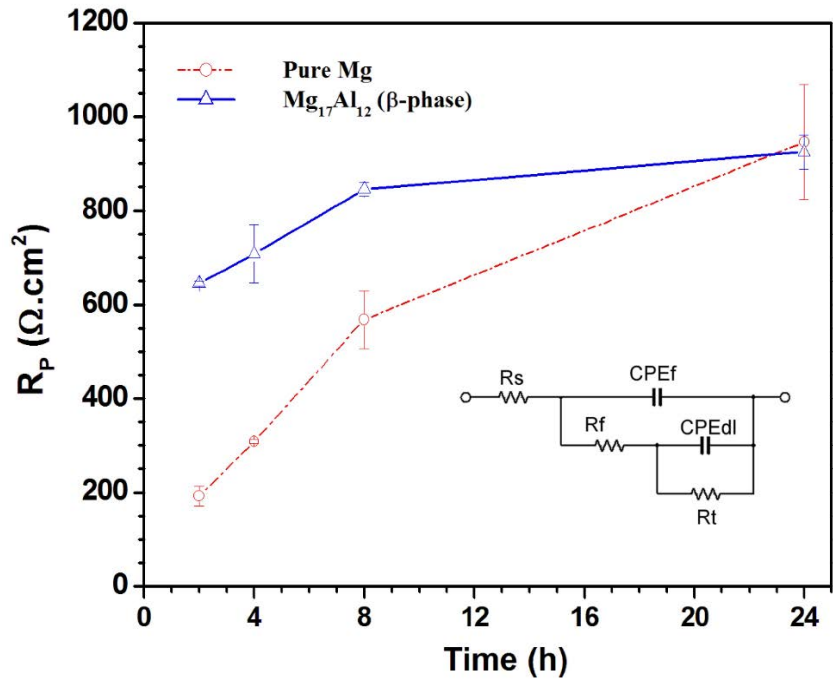


Figure 5.3 Polarisation resistance (R_p) vs. time for the pure Mg and β -phase (N=3).

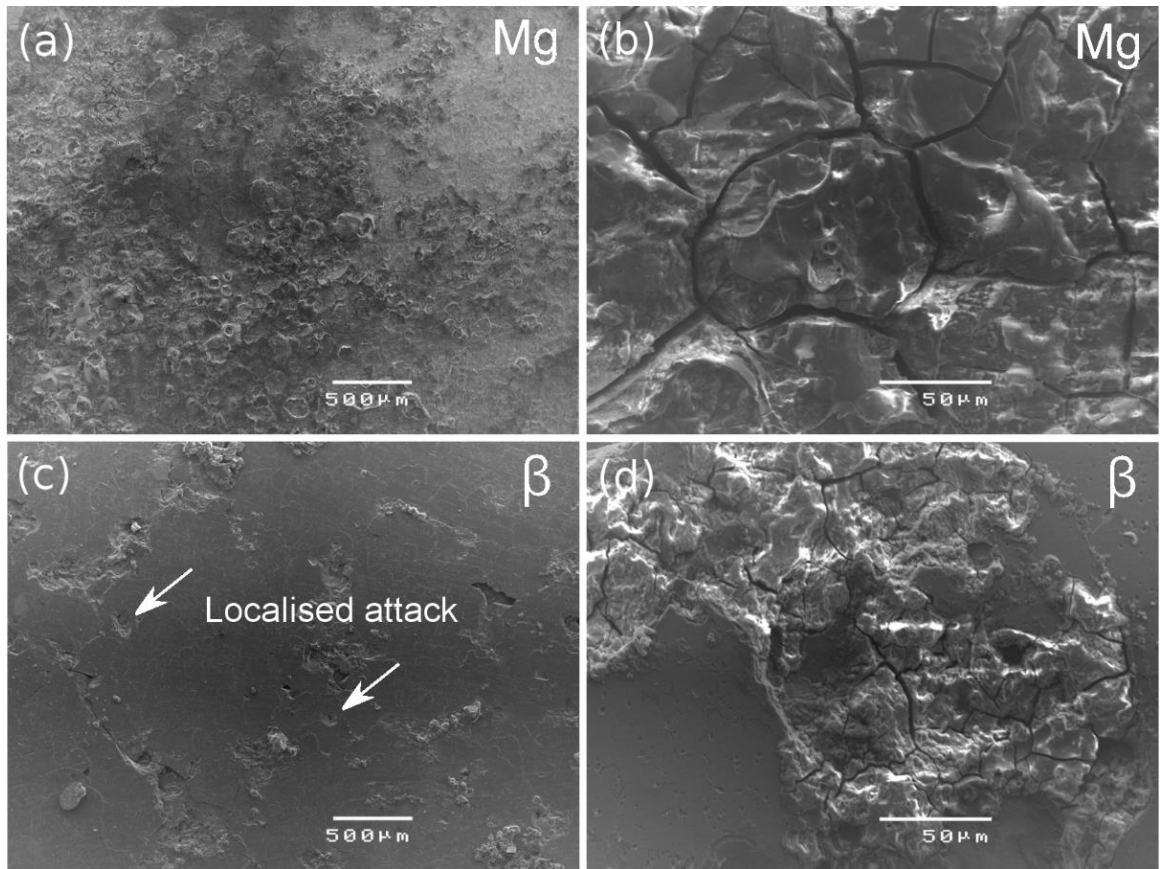


Plate 5.1 SEM images after 24 h immersion in SBF for (a, b) pure Mg and (c, d) β -phase.

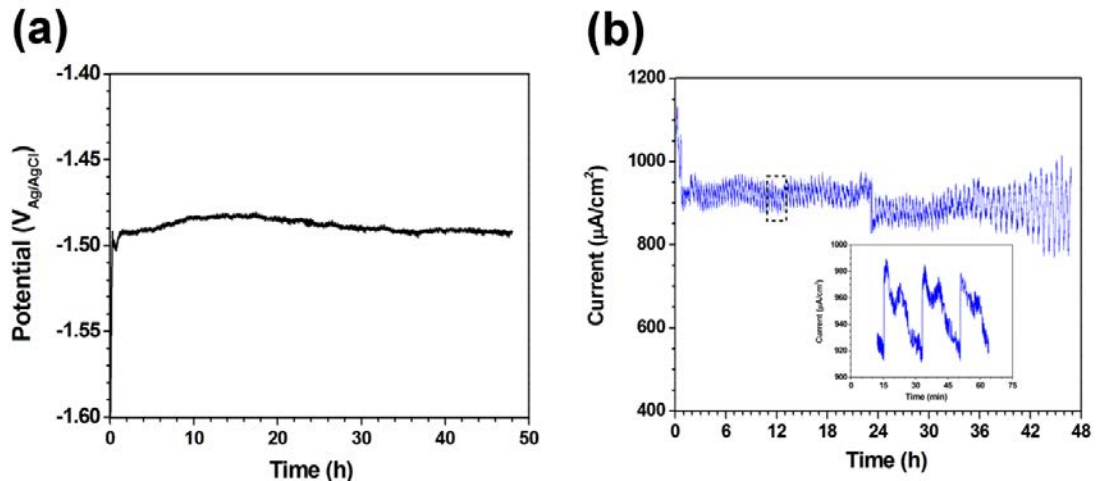


Figure 5.4 (a) Mixed potential of the pure Mg and β -phase during the galvanic coupling and (b) current vs. time during the galvanic coupling.

The falling of particles from the white powder layer on the β -phase sample during galvanic coupling could be due to the following two reasons: (i) particle size growth resulting in poor adhesion and (ii) hydrogen bubble bursting (hydrogen evolution reaction, a predominant cathodic reaction) causing the particles to fall. The chemistry of the white powder layer on the β -phase sample was analysed using FTIR spectroscopy, and the obtained spectra is shown in Fig. 5.5. The peak at 1045 cm^{-1} corresponds to PO_4^{3-} . There is also a distinct peak at 1432 cm^{-1} , suggesting the presence of CO_3^{2-} . Another, smaller peak is visible at 868 cm^{-1} , also indicative of CO_3^{2-} . The spectra is characteristic of an amorphous carbonated calcium phosphate (Habibovic et al., 2002; Qu and Wei, 2008; Berzina-Cimdina and Borodajenko, 2012). To confirm this, an XRD analysis was conducted on the white powder and the spectra is shown in Fig. 5.6. The spectra showed no visible peaks, suggesting that the deposited layer was amorphous in structure. Similar results have been presented in other studies, which showed only a “halo” region, indicative of broadening of apatitic diffraction lines (Barrère et al., 1999; Habibovic et al., 2002; Barrère et al., 2002).

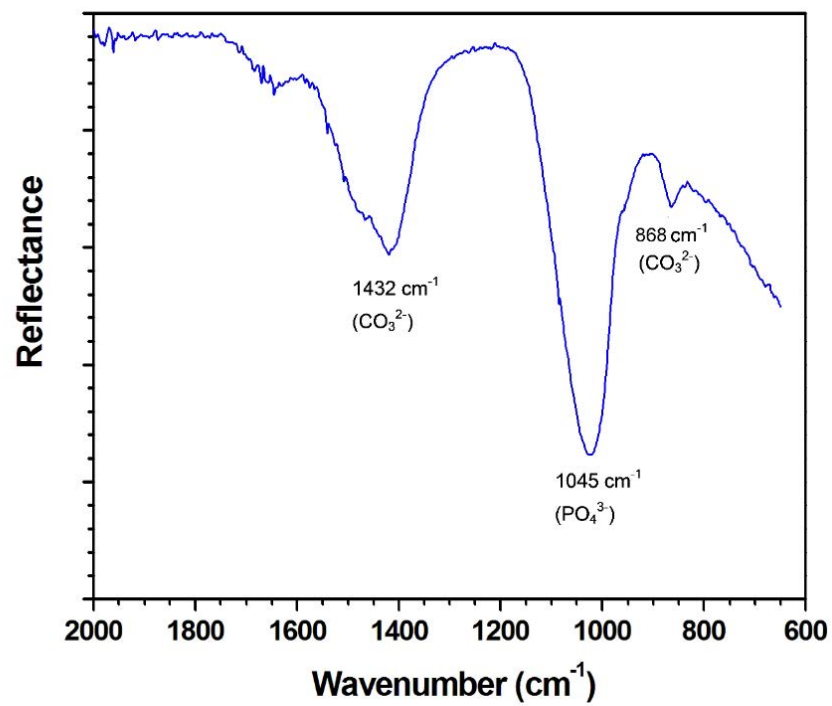


Figure 5.5 FTIR spectrum of the coating deposited on the β -phase.

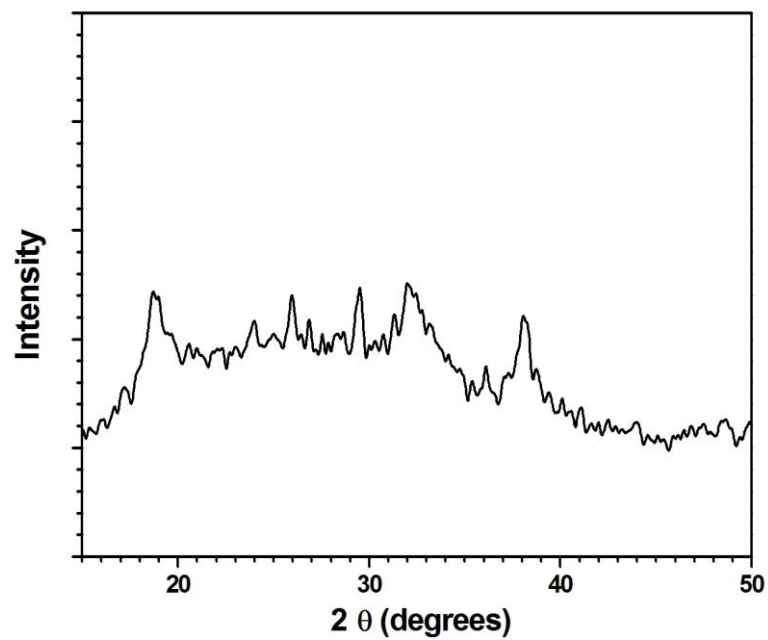


Figure 5.6 XRD pattern of the coating deposited on the β -phase.

Plate 5.2 shows the SEM images of the β -phase sample surface following 4 h galvanic coupling in SBF. It can be seen that the particles have covered the entire surface with even distribution of pores across the entire surface. The cathodic reaction of the microgalvanic degradation is hydrogen gas evolution, which forms gas bubbles on the β -phase surface. It can be suggested that the growth and subsequent detachment due to hydrogen bubble bursting from the surface could remove some of the calcium phosphate particles, resulting in the observed morphology. In Plate 5.2 (b), the coating displays irregular growth within the grains, and thus, it is evident that the coating is poorly crystalline in nature.

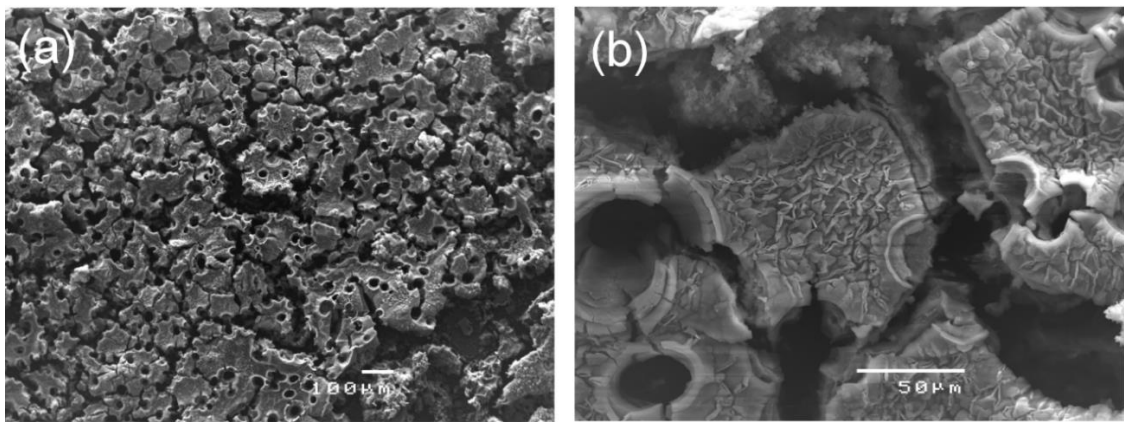


Plate 5.2 SEM images of the coating after 4 h galvanic coupling in SBF at (a) low magnification, showing pores and (b) high magnification showing particles.

To compare how the galvanic coupling affected the degradation behaviour of the two phases, the samples were decoupled and further immersed in SBF. Fig. 5.7 (a) and (b) show the open circuit potentials (OCP) of the samples prior to and following the galvanic coupling, respectively. It can be seen that in the pre-coupling immersion, the two samples reached a relatively stable OCP of $-1.75 V_{\text{Ag}/\text{AgCl}}$ for pure Mg and $-1.05 V_{\text{Ag}/\text{AgCl}}$ for β -phase, which are well matched with the values presented in literature (Kannan et al., 2012a).

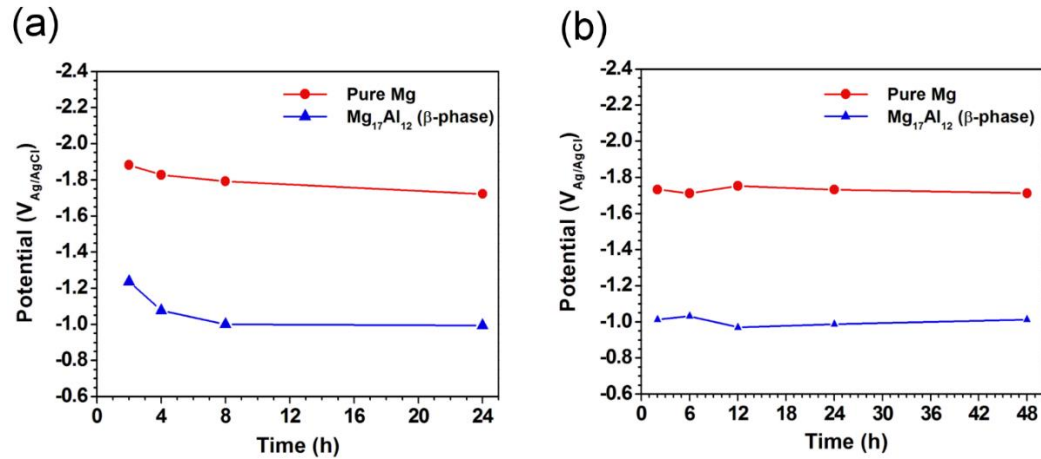


Figure 5.7 Open circuit potential (OCP) for the pure Mg and β -phase during immersion in SBF (a) prior to galvanic coupling and (b) following galvanic coupling.

Interestingly, following the galvanic coupling, the samples showed only a slight change in the potential in the initial stage, but quickly returned to similar values. Fig. 5.8 shows the Nyquist and Bode plots for the post-galvanically coupled pure Mg and β -phase sample immersed in SBF for different immersion period (2-48 h). Fig. 5.9 shows the calculated R_P values following the equivalent circuit modelling. The R_P for pure Mg stayed relatively constant throughout the entire 48 h exposure period. Conversely, for the β -phase, the initial R_P showed a value significantly higher than that of pure Mg, as shown in Fig. 5.3. This can be attributed to the formation of the calcium phosphate layer, as described previously. A two-tail unpaired t-test of pure Mg and β -phase ($N=3$) showed that the p value was 0.0003 for this immersion time. However, this resistance rapidly drops over time, reaching less than 40% of its value within 12 h immersion, and less than 20% within 48 h. By the 48 h immersion point, the R_P had begun to converge on that of pure Mg, not only confirming the results presented in Fig. 5.3, but also strongly suggesting that the calcium phosphate layer is poorly protective over long immersion times. At 48 h, the p-value had increased to 0.2786, suggesting an insignificant difference between the two samples.

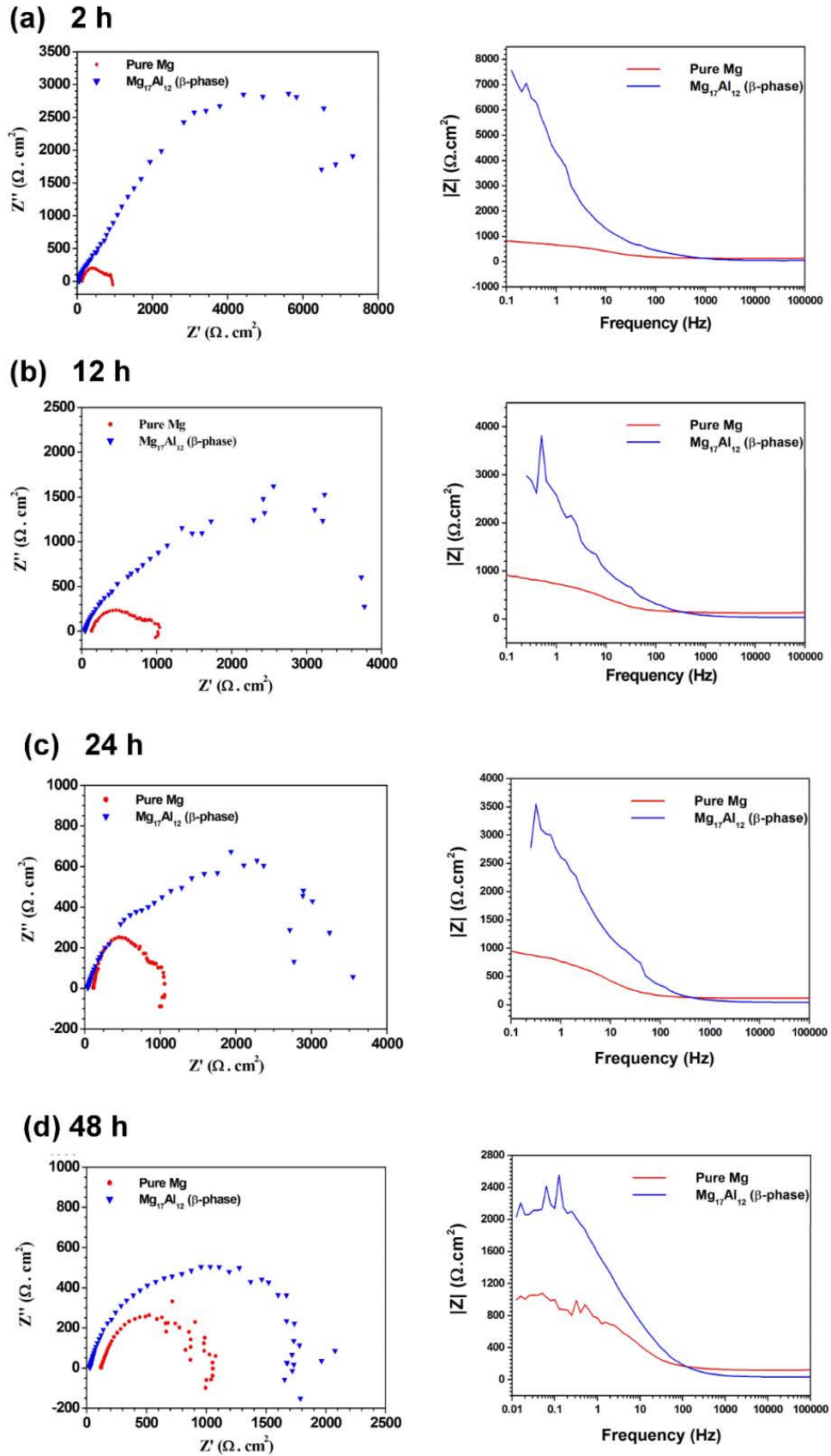


Figure 5.8 Post-coupled Nyquist and Bode plots of the pure Mg and β -phase immersed in SBF for (a) 2 h, (b) 12 h, (c) 24 h and (d) 48 h.

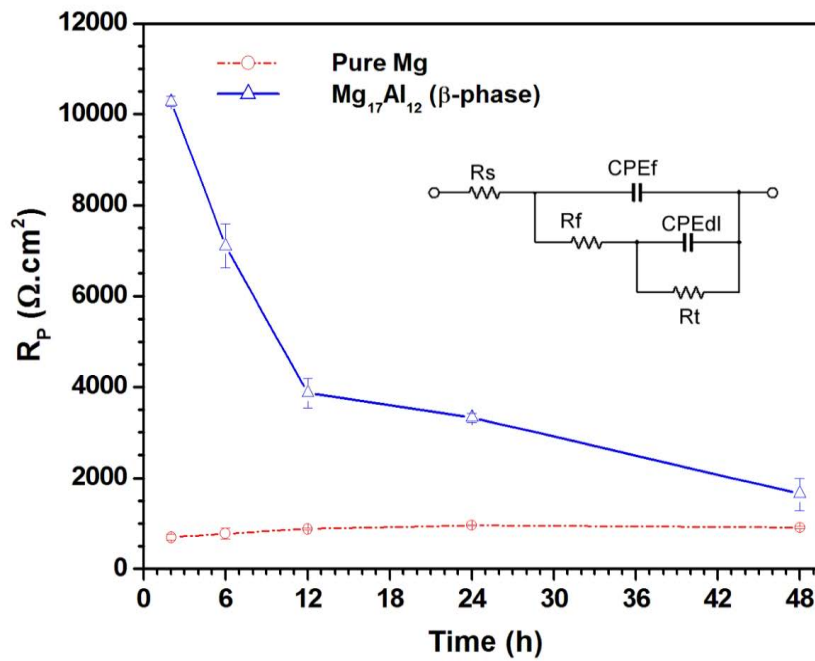


Figure 5.9 Post-coupled R_p vs. time for the pure Mg and β -phase (N=3).

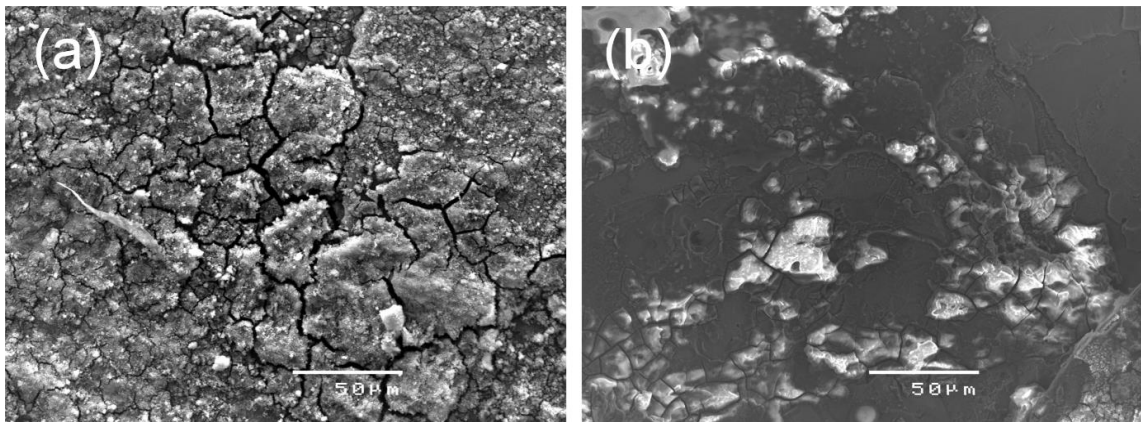


Plate 5.3 SEM images of the coating after 4 h immersion in SBF, (a) showing calcium phosphate coating degradation, and (b) the same sample with the remaining calcium phosphate particles removed.

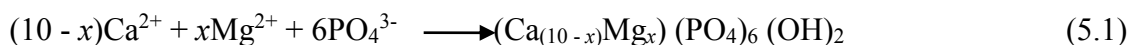
Plate 5.3 (a) and (b) show the post-immersion β -phase surface. It can be seen that the calcium phosphate surface that was visible in Plate 5.2(a) has been severely degraded, leaving a large proportion of the substrate surface exposed. Interestingly, no localised

degradation was visible (Plate 5.1) suggesting that the calcium phosphate coating was partially protective over this time. Removal of the remaining calcium phosphate layer, as shown in Plate 5.1 (b), further reveals that some general degradation has occurred on the β -phase surface, with no evidence of localised attack.

5.4 Discussion

The measured R_p values for pure Mg and β -phase suggest that there is no significantly different long-term degradation resistance in SBF when considered separately. The stability of the secondary phase particles (β -phase) in Mg alloys is almost entirely due to the cathodic protection. However, after galvanically coupling the two samples, the R_p for the β -phase was dramatically higher at 2 h immersion than the uncoupled value at the same immersion time.

It has been reported in the literature that hydrogen diffuses into the β -phase surface during galvanic coupling in chloride-containing solution, and then diffuses into the product layer during the degradation (Zhang et al., 2006). It was further suggested that the hydrogen entering the layer would be ionised, and could decrease the vacancies in the valence band of the product film and thus increasing the degradation resistance. However, this explanation is unlikely to cause the dramatic increase in the β -phase R_p as observed in this study in SBF (Fig. 5.9). The increase in R_p is mainly due the deposition of calcium phosphate particles onto the β -phase surface. It is well known that the local pH rise decreases the solubility of calcium and phosphate ions in solution (Barrère et al., 2002). Calcium and phosphorous rich precipitate formation was noted by Song et al. (2009) on AZ31 after immersion in 12 h in SBF, and was found to be $\text{Ca}_{10}(\text{PO}_4)_6(\text{OH})_2$. Several authors reported the formation of an amorphous calcium phosphate layer formed biomimetically on Ti-6Al-4V by immersion in SBF (Barrère et al., 1999; Habibovic et al., 2002; Barrère et al., 2002, Waterman et al., 2011). There have also been suggestions that the biomimetic formation of carbonated amorphous calcium phosphate on Mg substrates also incorporates Mg into the lattice, via (Gray-Munro et al., 2008; Gray-Munro et al., 2009):



Carbonates are incorporated into the structure via partial ionic substitution with either PO_4^{3-} or OH^- groups (Boanini et al., 2010). The reason as to why the layer is amorphous as opposed to crystalline is explained by the presence of Mg^{2+} ions in the solution. Mg^{2+} is known to inhibit the crystal growth of calcium phosphate, causing the observed amorphous structures (Barrère et al., 1999; Habibovic et al., 2002, Barrère et al., 2002). It has been reported that biomimetically formed calcium phosphate layer in Mg deficient environments are more crystalline than calcium phosphate formed in environments containing Mg^{2+} ions (Barrère et al., 1999). This mechanism is further supported by a study by Tie et al. (2010), which conducted XPS studies on Mg following 20 h immersion in SBF. They reported $\text{Ca}_m(\text{PO}_4)_n(\text{OH})_x$ and CaCO_3 to be the most likely formed degradation products.

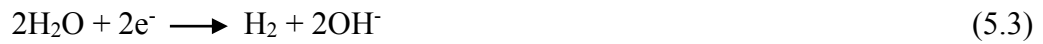
In this study, it was assumed that the anode/cathode area remains constant, thus causing a constant rate of growth of calcium phosphate on the surface. In reality, the anodic matrix will preferentially degrade, which can (for network particles such as in the case of AZ91), leave behind a layer of almost 100% secondary phase near to the metal/degradation medium interface (Song and Atrens, 1999; Kannan et al., 2008). A numerical model depicting the micro-galvanic degradation of an AM30 α phase and β phase in NaCl was reported by Deshpande et al. (Deshpande, 2011). In the model, it was shown that for continuous β -phase networks, as the α -phase preferentially dissolves, the β -phase fraction will approach 100%. For discrete β -phase distributions, this phase would fall out into the electrolyte, since it is not well supported along the depth of the alloy. In both these cases, the galvanic effect near to the surface would vary significantly during the degradation process, since the galvanic degradation is accelerated when the cathode-to-anode area ratio is high, and conversely, lessened when it is low.

This was modelled experimentally by uncoupling the materials and exposing them to SBF separately. The R_p of pure Mg after galvanic coupling stayed relatively constant throughout the whole 48 h immersion, mimicking the long-term degradation behaviour of pure Mg with no galvanic coupling. The β -phase R_p initially started significantly higher than pure Mg (due to the calcium phosphate coating), but sharply dropped within 12 h, before levelling off at $1650 \Omega \cdot \text{cm}^2$, only 16 % of its measured resistance at 2 h immersion. This suggests that the calcium phosphate coating was not stable on the

β -phase substrate, and will rapidly degrade once the secondary phase is no longer cathodically protected. Non-crystalline calcium phosphate coatings are not particularly stable under physiological conditions, and it has been suggested that the coating undergoes a dynamic precipitation/dissolution process (Zhang et al., 2009). Thus, as the cathodic protection of the β -phase is reduced due to Mg matrix dissolution, the calcium phosphate formation will slow and eventually be overtaken by dissolution. In the case of discontinuous particles, it is more likely that the secondary phase precipitates would be removed by undermining, which of course would negate the galvanic formation of calcium phosphate entirely.

Once the protective effect of the calcium phosphate layer on the β -phase has been significantly reduced, the passivation of the Mg and aluminium begins to play a more dominant role. Song et al. proposed the formation of a three layer passive film, consisting of Al_2O_3 , MgO and $\text{Mg}(\text{OH})_2$ (Song, 1998). In an aqueous, chloride containing environment, the Al passive layer would be at least partially hydrated, and chlorides would be incorporated into the film through a combination of migration through oxygen vacancies and passive layer thinning (McCafferty, 2003). Over time, the $\text{Mg}(\text{OH})_2$ layer would be converted to soluble MgCl_2 , and localised pH rises would cause the aluminium oxide to be converted into soluble AlO_2^- (Song et al., 1998), resulting in complete dissolution of the β -phase.

To further illustrate the points above, a phenomenological model is shown in Fig. 5.10. The model shows a semi-continuous, high volume fraction β -phase network along the primary α -grain boundaries, such as die-cast AZ91. Note that while secondary α -eutectic regions would likely occur around the β -particles, they have been omitted from the model for simplicity. All degradation product formation has also been omitted for the same reason. The first stage shows each of the phases prior to immersion. Once exposed to the physiological medium, dissolution of the Mg matrix initiates. Microgalvanic coupling between the anodic α -phase and the cathodic β -phase enhances the degradation close to the α/β interface. In this stage, the β -phase is largely protected. The dissolution of the α -phase Mg cathodically produces hydrogen on the β -phase, as shown, via the half reactions:



As such, there is a localised pH rise close to the surface. This reduces the solubility of calcium and phosphate ions in the solution, causing them to precipitate out as a calcium phosphate layer. Carbonates are incorporated into the lattice via partial ionic substitution with PO_4^{3-} and OH^- groups. Mg may also be incorporated since the concentration of Mg^{2+} ions near the degradation surface should be relatively high.

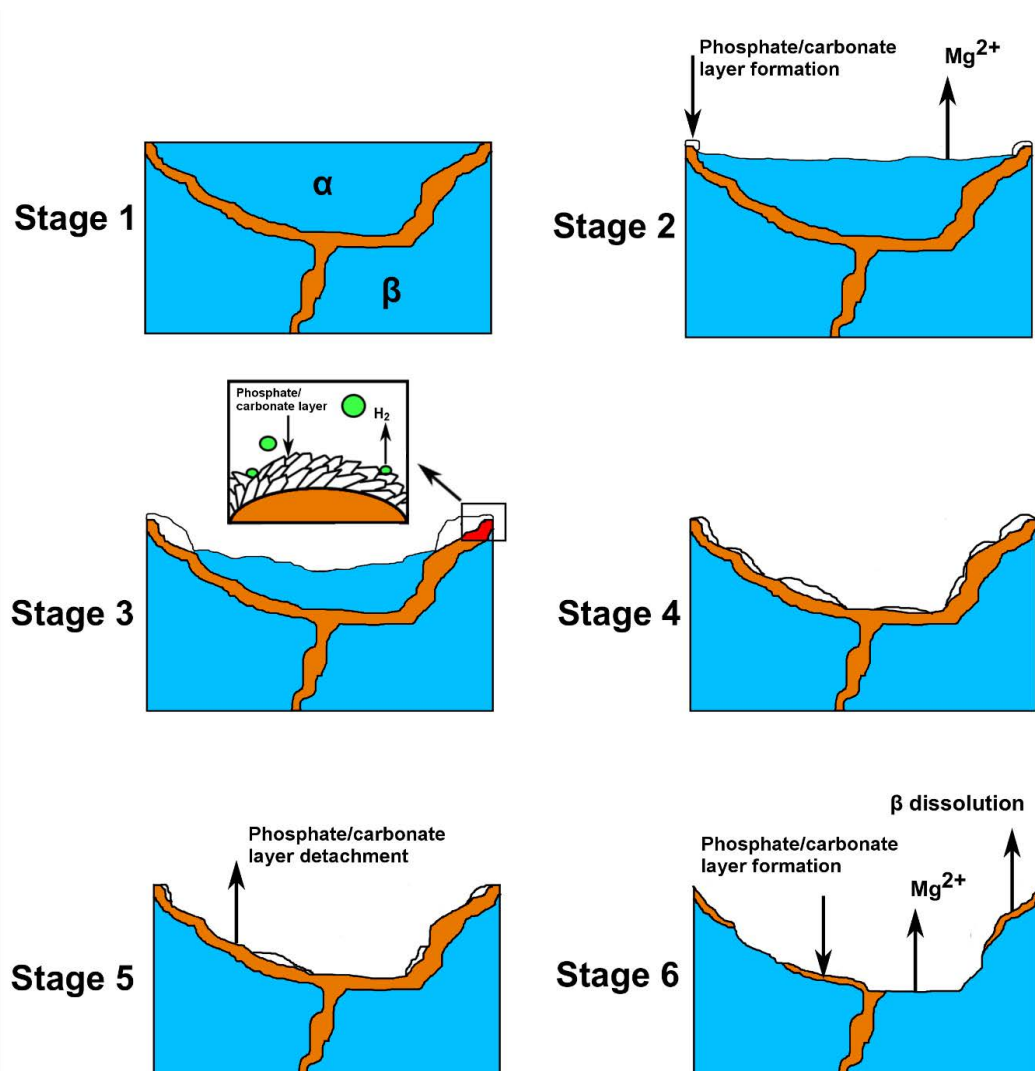


Figure 5.10 Phenomenological model describing the micro-galvanic effects in an Mg alloy.

Calcium phosphate is known for its protective nature of metallic implant materials under *in vitro* conditions (Song et al., 2010), and the formation of the calcium phosphate layer accounts for the initial sharp increase in the β -phase R_P as shown in Fig. 5.9. Stage 3 shows the growth of the calcium phosphate coating on the β -phase, whilst the α -grains undergo heavy attack. The large disparity between the degradation resistances of the Mg matrix and β network eventually causes the near complete dissolution of the α -grains, while leaving the β -phase relatively unattacked. The low volume fraction of α -phase near to the exposed β -phase reduces the micro-galvanic effect in these areas. As such, detachment of the calcium phosphate rapidly occurs, as evidenced by the sharp drop in R_P seen in Fig. 5.9. Fig. 5.9 suggested that over time, the R_P of the β -phase approaches that of pure Mg. Thus, once the exposed β -phase is no longer protected by calcium phosphate formation or micro-galvanic coupling, rapid dissolution occurs. This inevitably exposed fresh α -grains, allowing the process to repeat.

It is important to note that the composition of the matrix in Mg alloys would not be comprised purely of Mg, and would contain alloying elements. In the case of AZ series alloys, the primary phase is a solid solution of Mg and aluminium, which would shift the corrosion potential in the noble direction when compared to pure Mg alone (Mathieu et al., 2003; Pardo et al., 2008; Wen et al., 2009). However, since the potential of the Mg matrix is always anodic to the secondary phase particles, the micro-galvanic effects observed in this study are still applicable. The potential difference between the Mg matrix and β -phase would be slightly lessened, but would still be sufficient for micro-galvanic degradation. This would also be the case for rare-earth containing Mg alloys, which have been demonstrated to be susceptible to micro-galvanic degradation (Coy et al., 2010). For these alloys, the distribution of secondary phase particles tends to be more discrete as opposed to semi-continuous, and form in particle-like regions around the grain boundaries. In these cases, the lack of continuity would likely cause undermining of the secondary phase particles, rather than the cyclical α/β breakdown shown in Fig. 5.9.

5.5 Conclusions

Galvanic coupling of β -phase ($\text{Mg}_{17}\text{Al}_{12}$) with pure Mg in SBF resulted in the formation of carbonated calcium phosphate on the β -phase. While the calcium phosphate layer initially increased the degradation resistance of the β -phase, the layer rapidly degraded once the galvanic coupling was removed. Within 48 h immersion in SBF, the degradation resistance of the β -phase began to approach that of pure Mg. The results suggest that under long-term immersion period in SBF, the degradation resistance of the β -phase will decrease and eventually the β -phase will dissolve in body fluid as the micro-galvanic effects are reduced due to complete dissolution of the Mg matrix around the β -phase.

Chapter. 6 Multilayer Coatings on pure Mg

6.1 Introduction

In order to delay the general and localized degradation of Mg and its alloys, there has been growing interest in biocompatible and biodegradable coatings. A wide range of coatings has been studied to this end, including plasma electrolytic oxidation (PEO), biodegradable polymers, and calcium phosphate (CaP) deposition. Calcium phosphates are well-known for their high bioactivity and biocompatibility, and have been successfully used as coating materials on metallic implant materials such as titanium and its alloys to improve osseointegration and osteoconductivity. There are various methods available for the coating of CaP on metallic substrates, such as high-temperature sputtering and plasma spraying (Yang et al., 2005). However, these are often high temperature techniques, potentially resulting in a decomposition and non-uniformity of the coating when used on an Mg substrate.

Electrochemical coating of CaP is attractive for Mg-based materials since it can be done rapidly and at room temperature, and possible to coat complex geometries such as plates and screws implants. There has been some preliminary work done on galvanostatic and potentiostatic deposition of CaP on Mg and its alloys. However, a limitation of these electrochemical techniques is that the rapid deposition of CaP results in the evolution of large amounts of hydrogen gas. The hydrogen gas bubbles build-up on the surface, potentially detaching and damaging the CaP layer, resulting in a loosely packed and inhomogeneous structure. Further, in the case of potentiostatic deposition, a negatively charged layer forms across the surface, which impedes the adherence of ions and results in poor deposition. These issues can be overcome by utilising a pulsed-potential waveform (Chandrasekar and Pushpavanam, 2008).

Pulse-potential method has shown to produce CaP coating on Mg and its alloys with improved performance (Wang et al., 2010; Kannan and Wallipa, 2013). In principle, the OFF time in the pulse-potential method dissipates the charge build up on the surface, and thereby allowing ions to freely diffuse towards the substrate (Chandrasekar et al., 2008). A recent study by one of the authors has shown that addition of ethanol to the coating electrolyte improves the packing of CaP on an Mg-aluminium-zinc alloy

(AZ91) (Kannan, 2013). A synergistic effect of pulsed-potential and ethanol addition has also been reported by the author, which produced high performance CaP coating on AZ91 alloy (Kannan, 2012).

While these results show good performance of the CaP coatings on AZ91, which contains 9 wt. % aluminium, there has been a recent shift toward aluminium-free alloys. Magnesium-calcium (Mg-Ca) alloys have been studied as a base material due to the attractive properties of Ca as an alloying element, such as good biocompatibility (Li et al., 2008; Erdmann et al., 2011). Chun-Yan et al. (2010) compared potentiostatically coated brushite ($\text{CaHPO}_4 \cdot 2\text{H}_2\text{O}$) coatings on AZ31 and Mg-1.0Ca alloys in Hank's solution. The addition of the coatings reduced the corrosion current densities by two orders of magnitude for both alloys. However, measurement of the evolved hydrogen suggested that the CaP coated Mg-1.0 Ca provided inferior resistance to even the uncoated AZ31 sample. This can be attributed to the underlying degradation behaviour of the substrate itself. AZ series alloys are significantly more passive than Mg-Ca alloys, and will undergo less dissolution during the coating process, resulting in a better coating.

This work utilises the techniques described by Kannan (Kannan, 2012) on an Mg-Ca substrate to produce a CaP coating. The results section investigates the *in vitro* degradation performance of the single layer CaP (along with influence of cathodic activity on electrochemical deposition of CaP), and improves on it by producing a dual layer PEO/CaP, and a triple layer PEO/CaP/PLLA coating.

6.2 Materials and Methods

There were three Mg alloys studied: AZ91 (9.18 wt. % Al, 0.78 wt. % Zn) and Mg-Ca (1 wt. % Ca) for the initial single layer CaP coatings, and high purity Mg for the subsequent hybrid coatings. The CaP coatings were produced using a pulsed potential waveform for the single layer coatings, and a constant potential for the hybrid coatings. All experiments were done under physiological conditions as described in Chapter 3.

6.3 Results and Discussion

6.3.1 Single layer CaP coating

The average coating thickness of the deposited CaP layer was measured to be 5.7 ± 0.4 μm . The FTIR spectra (Fig. 6.1a) of the coating showed strong bands at 1122, 1052 and 984 cm^{-1} corresponding to phosphate (Pecheva et al., 2004; Pramatarova et al., 2005). Also, bands at 1631 cm^{-1} and 874 cm^{-1} corresponding to hydroxide and carbonate groups, respectively, were also observed. XRD analysis (Fig. 6.1b) confirmed that the compound is CaP, i.e., $\text{CaHPO}_4 \cdot 2\text{H}_2\text{O}$. However, the hydroxide and carbonate groups observed in the FTIR spectra, which could be $\text{Mg}(\text{OH})_2$ and MgCO_3 , were not evident in the XRD, probably due to the amorphous nature of the products.

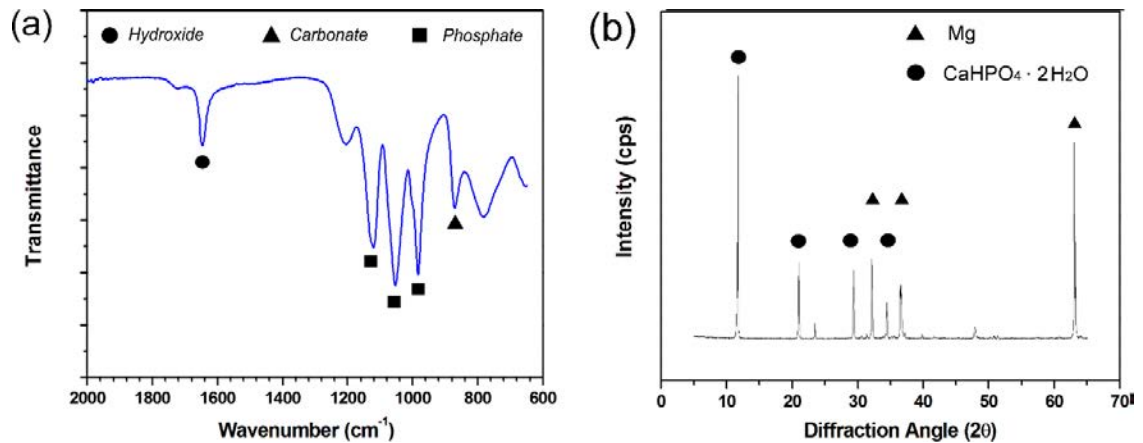


Figure 6.1 (a) FTIR and (b) XRD spectra of the CaP coating on Mg-Ca alloy.

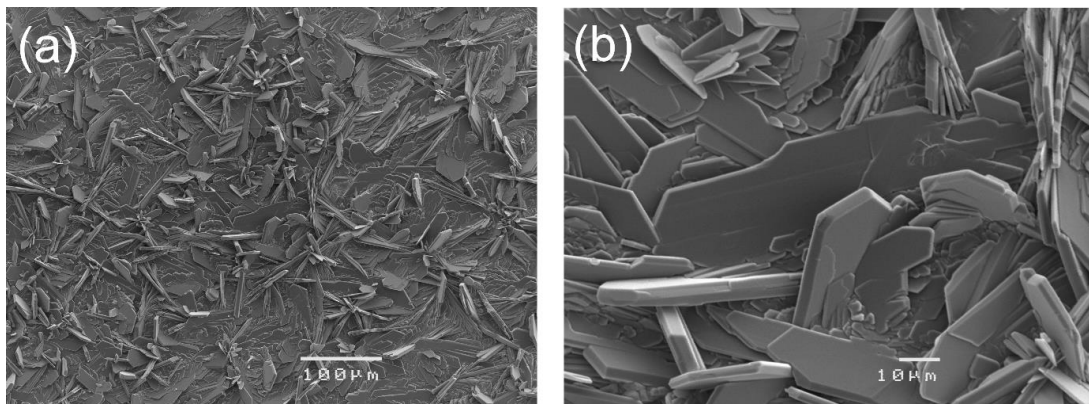


Plate 6.1 SEM images of the CaP coating on Mg-Ca alloy: (a) low magnification shows complete coverage of the base material, and (b) high magnification shows large, flat and irregularly oriented particles.

The morphology of the CaP coating obtained from SEM imaging is shown in Plate 6.1, which reveals large, flat and irregularly oriented CaP particles. However, the base metal was completely covered by the CaP particles. Interestingly, the CaP layer coated under similar conditions on AZ91 alloy showed much denser packing and the particles were larger in size (Le Guéhenec et al., 2007). This suggests that the morphology of the CaP coating using electrochemical method depends on the electrochemical behaviour of the base material.

The potentiodynamic polarisation curves of the bare alloy and CaP coated alloy are shown in Fig. 6.2 and the corresponding electrochemical data is given in Table 6.1. CaP coating to the alloy significantly improved the degradation performance, i.e., by decreasing the corrosion current density (i_{corr}) from $90 \mu\text{A}/\text{cm}^2$ to $4.1 \mu\text{A}/\text{cm}^2$, which is $\sim 95\%$ reduction. The coating also shifted the corrosion potential (E_{corr}) towards the noble direction, i.e., $-1.64 \text{ V}_{\text{Ag}/\text{AgCl}}$ to $-1.46 \text{ V}_{\text{Ag}/\text{AgCl}}$.

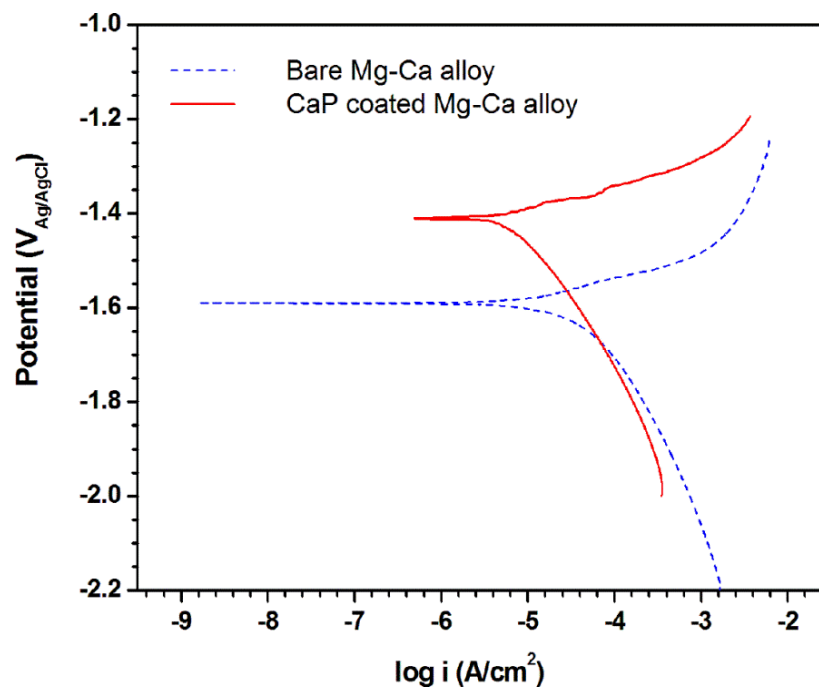


Figure 6.2 Potentiodynamic polarisation curves for the bare alloy and CaP coated Mg-Ca alloy in SBF.

Table 6.1

Electrochemical degradation parameters of bare alloy and CaP coated alloy obtained from potentiodynamic polarisation curves in SBF (N=2).

Sample	E_{corr} (V _{Ag/AgCl})	i_{corr} ($\mu\text{A}/\text{cm}^2$)
Mg-Ca alloy	-1.63±0.06	90±14.1
CaP coated alloy	-1.46±0.09	4.1±1.7

Fig. 6.3 shows the EIS plots from 2-72 h immersion of bare metal and CaP coated alloy in SBF. The polarisation resistance (R_p) calculated based on equivalent circuit modelling as shown in Fig. 6.4, and the open-circuit potential (OCP) measurements are shown in Fig. 6.5. The complete data of the modelling is presented in Table 6.2. It can be seen that for the bare alloy, the R_p initially starts at $\sim 413 \Omega \cdot \text{cm}^2$, and increases to $\sim 1305 \Omega \cdot \text{cm}^2$ after 24 h immersion due to the formation of a partially protective passive film. The R_p then decreases across the remaining immersion time to $\sim 695 \Omega \cdot \text{cm}^2$ after 72 h as the passive film is attacked by the presence of the Cl^- ions. All the plots show a high frequency capacitive loop, which correspond to charge transfer resistance and double layer capacitance. There is a mid-frequency capacitive loop for the 2 h immersion curve, which is indicative of the relaxation of mass transport through the degradation product layer.

The mid-frequency loop is no longer visible from 8 h onwards, suggesting that the partially protective layer is no longer present. The R_p for the CaP coated alloy was initially much higher than the bare alloy, at an R_p of $\sim 6452 \Omega \cdot \text{cm}^2$ (~ 15 times higher). This value rapidly decreased by 82% over the immersion period, exhibiting an R_p of $1185 \Omega \cdot \text{cm}^2$ after 72 h immersion, which was only $\sim 70\%$ higher than the bare alloy. Interestingly, the R_p showed a slight increase after 48 h immersion, though this is within the margin of measurement error. All EIS plots for the CaP coated alloy showed a similar shape; a single high and mid-frequency capacitive loop corresponding to an outer layer and compact inner layer characteristic of ceramic coatings (Redepenning et al., 1996; Ghasemi et al., 2008).

The FTIR spectra and XRD analysis of the CaP coated alloy after in vitro degradation are shown in Fig. 6.6. The hydroxide and carbonate bands at 1631 cm^{-1} and 874 cm^{-1}

observed in Fig. 6.1 are no longer visible. The strong phosphate bands have also merged, showing only a broad phosphate band at approximately 1000 cm^{-1} . This reduction in bands suggests that there has been a change in the coating structure, due to either incongruent dissolution and/or re-precipitation of new CaP phases onto the surface (Redepenning et al., 1996; Kokubo, 1996). This was likely caused by localised pH increase due to hydrogen evolution reaction as a consequence of alloy dissolution. This reduces the solubility of calcium and phosphate ions in the solution, resulting in a subsequent precipitation onto the surface (Kokubo, 1996). XRD analysis (Fig. 6.6) did not show any strong peak of $\text{CaHPO}_4 \cdot 2\text{H}_2\text{O}$, which suggests that the precipitates/layer on the surface is possibly amorphous in nature.

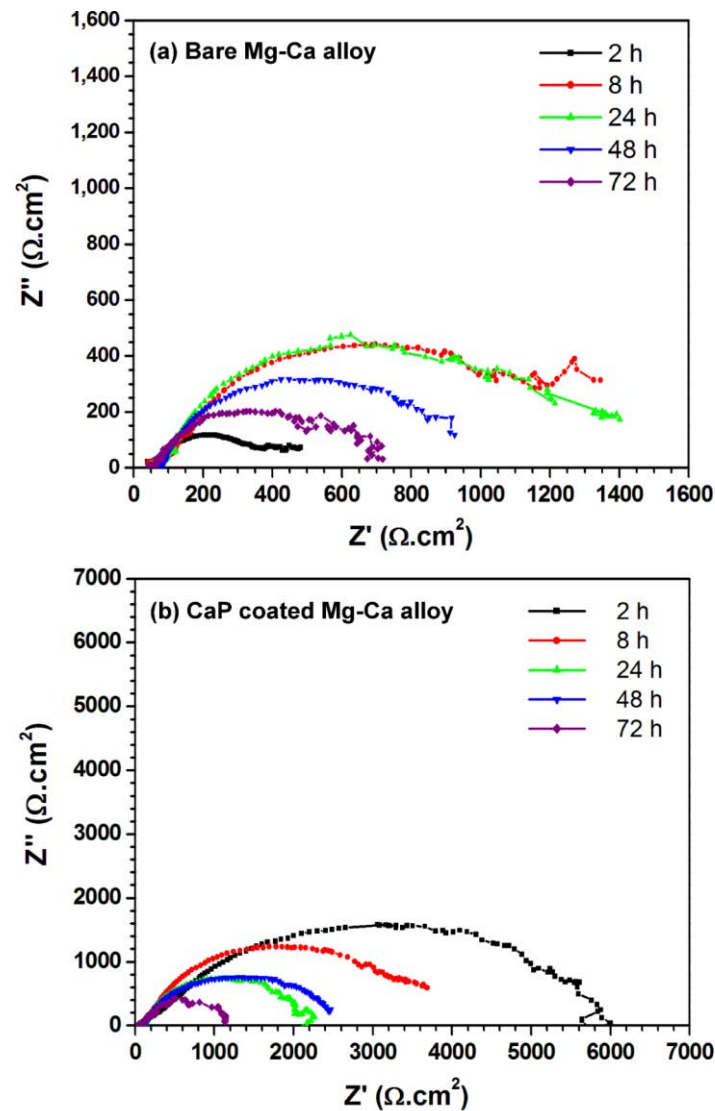


Figure 6.3 EIS plots for: (a) bare alloy, and (b) CaP coated Mg-Ca alloy over the 72 h immersion period in SBF.

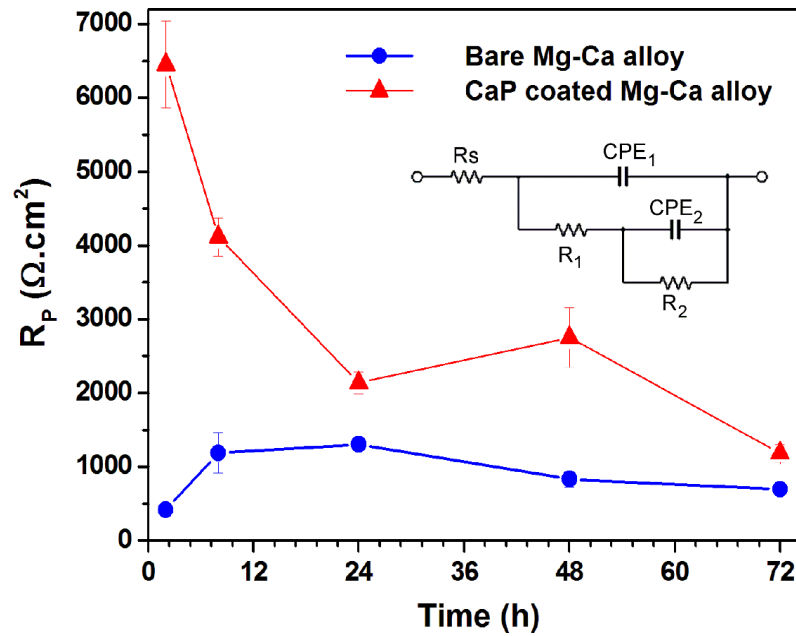


Figure 6.4 Polarisation resistance (R_p) vs. time from EIS data of bare alloy and CaP coated Mg-Ca alloy in SBF ($N=2$).

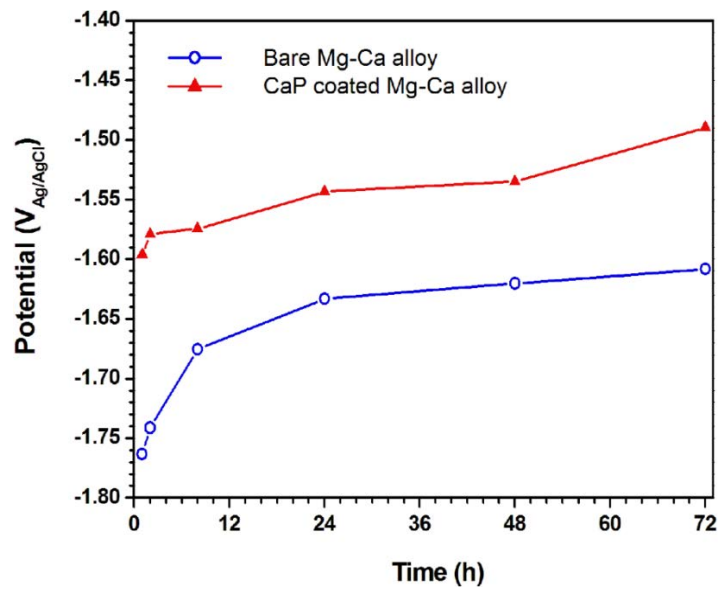


Figure 6.5 Open-circuit potential (OCP) measurements of the bare alloy and CaP coated Mg-Ca alloy during immersion in SBF

Table 6.2
Modelling data from the EIS plots of bare alloy and CaP coated alloy (N=2).

Sample	Time (h)	CPE ₁ ($\Omega^{-1}\cdot\text{cm}^{-2}\cdot\text{s}^{-n} \times 10^{-6}$)	n	R ₁ ($\text{k}\Omega\cdot\text{cm}^2$)	CPE ₂ ($\Omega^{-1}\cdot\text{cm}^{-2}\cdot\text{s}^{-n} \times 10^{-6}$)	n	R ₂ ($\text{k}\Omega\cdot\text{cm}^2$)	R _P ($\text{k}\Omega\cdot\text{cm}^2$)
Mg-Ca alloy	2	815.5 ± 110.3	0.52	0.021 ± 0.015	17.8 ± 4.4	0.88	0.392 ± 0.003	0.413 ± 0.011
	8	95.2 ± 20.0	0.53	0.113 ± 0.050	7.0 ± 2.4	0.98	1.077 ± 0.229	1.190 ± 0.140
	24	45.7 ± 32.0	0.77	0.062 ± 0.020	25.0 ± 11.0	0.88	1.243 ± 0.020	1.305 ± 0.003
	48	180.9 ± 127.2	0.59	0.041 ± 0.016	64.0 ± 8.7	0.80	0.791 ± 0.067	0.832 ± 0.051
	72	0.8 ± 0.1	1.00	0.016 ± 0.001	88.5 ± 12.2	0.74	0.679 ± 0.020	0.695 ± 0.021
CaP coated Mg-Ca alloy	2	6.6 ± 4.6	0.81	0.338 ± 0.111	22.6 ± 7.5	0.66	6.114 ± 0.405	6.452 ± 0.294
	8	22.5 ± 34.2	0.58	0.331 ± 0.148	12.5 ± 1.5	0.80	3.785 ± 0.017	4.116 ± 0.131
	24	12.5 ± 7.4	0.71	0.074 ± 0.006	58.8 ± 1.5	0.75	2.063 ± 0.079	2.137 ± 0.074
	48	0.4 ± 0.1	1.00	0.071 ± 0.002	58.2 ± 2.1	0.72	2.680 ± 0.203	2.751 ± 0.201
	72	28.7 ± 4.5	0.63	0.053 ± 0.007	88.1 ± 15.0	0.74	1.132 ± 0.012	1.185 ± 0.058

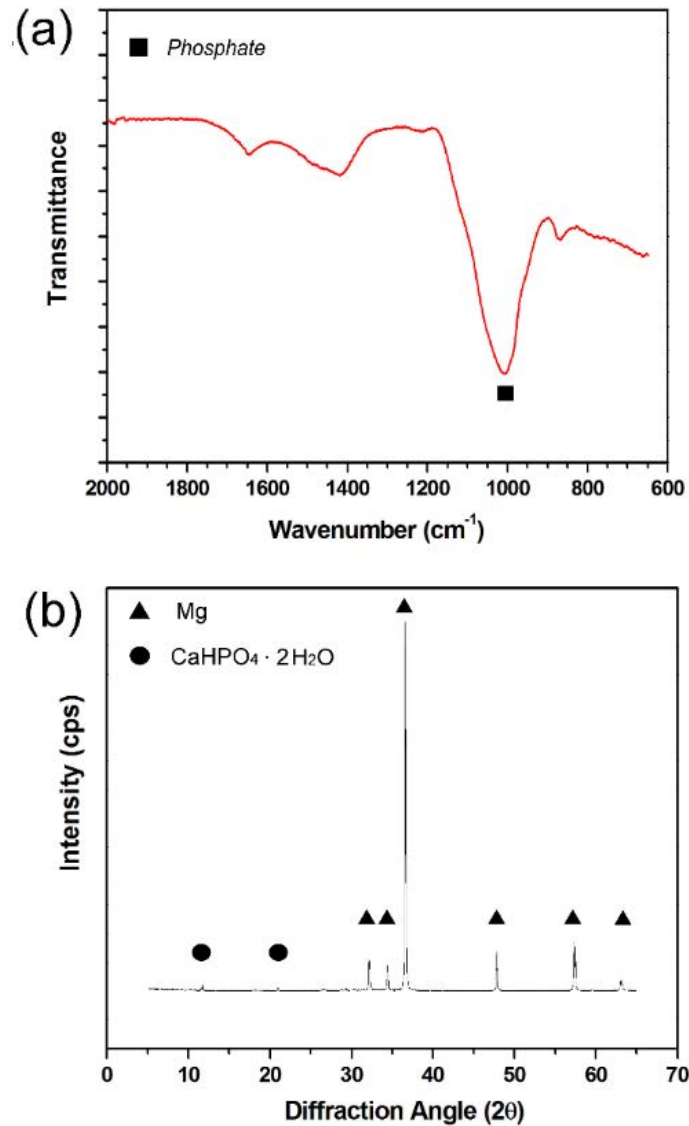


Figure 6.6 (a) FTIR and (b) XRD spectra of the CaP coated Mg-Ca alloy following 72 h immersion in SBF.

The morphology of the CaP coating following 72 h immersion is shown in Plate 6.2 a, b. It can be seen that there was noticeable damage to the coating across the entire surface, resulting in a high amount of cracking and skeletal, frond-like areas. This change in the morphology of the coating occurs once substrate dissolution initiates, forming Mg(OH)₂, which provides favourable sites for the reprecipitation of hydroxyapatite nucleation (Koerten and Van der Meulen, 1999; Li et al., 2008). These areas are points of rapid and dense crystal growth resulting in the tightly packed frond areas, while the surrounding areas become cracked as Mg(OH)₂ converts to highly

soluble MgCl_2 . A comparison with a corroded bare alloy (Plate 6.2 c, d) suggests that that there is no substrate surface directly exposed. The bare alloy underwent significant damage across the entire surface, with some areas of heavy pitting attack visible. It follows that since the CaP layer is still covering the entire substrate, the drop in R_P observed in Fig. 6.3 is due to penetration of electrolyte through the coating, rather than direct dissolution of the coating itself.

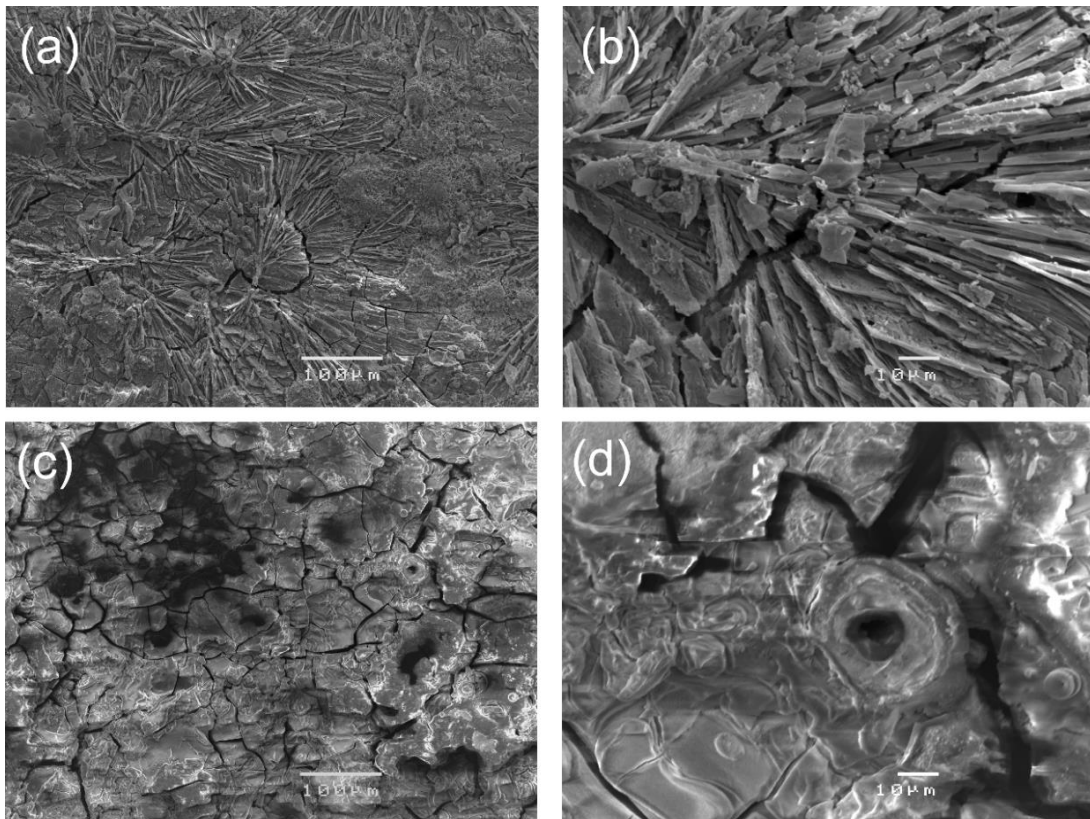


Plate 6.2 SEM images of: (a, b) CaP coated alloy, and (c, d) bare Mg-Ca alloy following 72 h immersion in SBF.

The degradation behaviour of the bare metal follows the progression typically seen in Mg alloys, i.e., an increase in R_P early on in the immersion due to film formation which is partially protective, followed by a slight decrease over time as this layer is deteriorated. The CaP layer, however, displays a much more rapid loss in its protection than expected. Calcium phosphates have been shown to have a very low rate of dissolution under physiological conditions (Koerten and Van der Meulen, 1999; Jonášová, et al., 2004). Conversely, the EIS results from this study show rapid drops in the measured resistance. This suggests penetration of the electrolyte through the CaP

layer. Once the electrolyte comes into contact with the substrate, Mg dissolution would result in H₂ evolution.

As the H₂ gas detaches, it breaks through the coating layer, compromising the protective nature of the CaP coating. The possible penetration of the electrolyte through the CaP layer is supported by the rest potential measurements (Fig. 6.5) prior to each EIS tests. Across the entire immersion period, there is a relatively stable separation in potentials (~100 mV) between the bare and the coated alloy. If there was a significant breakdown of the CaP layer to explain the rapid drop in R_P seen in Fig. 6.5, the rest potentials would begin to converge to that of the bare alloy. However, the near constant 100 mV potential difference between the two samples suggests that the CaP layer is still intact, albeit penetrated by the electrolyte.

Since the diffusion of the coating ions is critical for better coating, the degradation behaviour of the substrate may also play an important role on the coating morphology and performance. It is expected that the mass transfer resistance due to substrate dissolution would impact the cathodic deposition of CaP on the surface. To determine the significance of this effect, the CaP coating produced on Mg-Ca was compared to one on a substrate with a higher degradation resistance, AZ91 alloy. SEM analysis revealed that the coating morphology was significantly different between the coatings on Mg-Ca and AZ91 alloys (Plate 6.3 (a-d)). A low magnification micrograph (Plate 6.3a) of the coating on Mg-Ca alloy showed visible protruding particles distributed evenly across the entire surface. On the AZ91 alloy, however, the particles were relatively flat, with a much lower number of protruding particles (Plate 6.3c). Higher magnification micrographs of the coatings showed that the particles were of a slightly smaller size on the Mg-Ca alloy than those on the AZ91 alloy (Plate 6.3b and d). The packing of the particles were relatively denser on the AZ91 alloy. The FTIR spectra of the two coatings suggest that the coatings are similar in composition (Fig. 6.7). The strong bands at 1122, 1052 and 984 cm⁻¹ correspond to phosphate (Pecheva et al., 2004; Pramatarova et al., 2005), and the bands at 1631 cm⁻¹ and 874 cm⁻¹ correspond to hydroxide and carbonate groups, respectively.

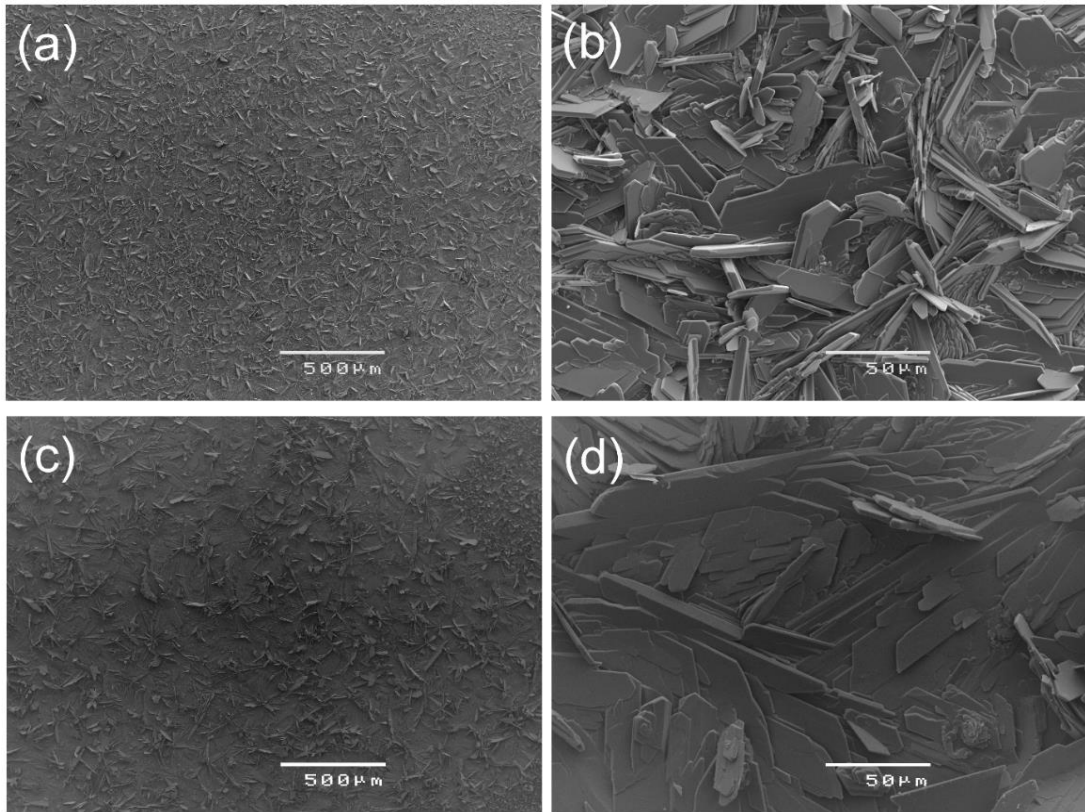


Plate 6.3 SEM images of the calcium phosphate coating on: (a, b) Mg-Ca alloy, and (c, d) AZ91 alloy.

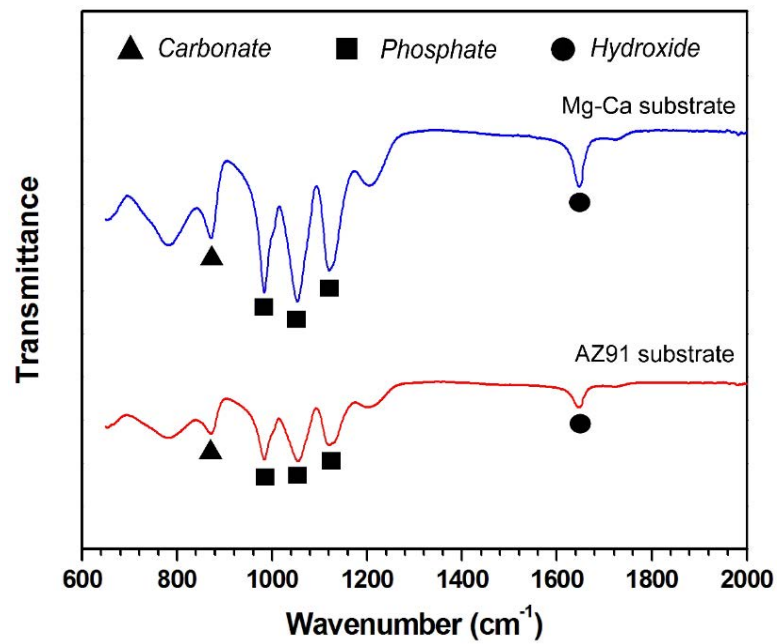


Figure 6.7 FTIR spectra of the calcium phosphate coating on Mg-Ca and AZ91 alloys.

The in vitro degradation behaviour of the bare alloys was evaluated in SBF. Fig. 6.8a shows the EIS plots of the bare Mg-Ca and AZ91 alloys. Both alloys showed similar characteristics, i.e., high and mid frequency capacitive loops. The AZ91 alloy also showed a low frequency inductive loop, which has been shown to be indicative of pitting degradation. The Nyquist plot of the Mg-Ca alloy was modelled using the equivalent circuit $R_s(Q_f(R_f(Q_{dl}R_{ct})))$, where R represents resistors and Q represents constant phase elements. R_s is the solution resistance, R_f and Q_f represent film effects, Q_{dl} represents double layer capacitance and R_{ct} represents charge transfer resistance. The AZ91 alloy used a similar model with added inductive elements: $R_s(Q_f(R_f(Q_{dl}R_{ct}))(R_L L))$. This model has been used for Mg in chloride containing environments (Walter and Kannan, 2011).

The bare Mg-Ca alloy exhibited a R_p of $6.1 \times 10^2 \Omega \cdot \text{cm}^2$, ~30% lower than that of AZ91 alloy ($8.4 \times 10^2 \Omega \cdot \text{cm}^2$). The degradation performance of CaP coated Mg-Ca and AZ91 alloys showed significant difference between them. Interestingly, the CaP layer created a much larger relative difference in R_p between the two alloys. The CaP coated alloys were modelled using the equivalent circuit $R_s(Q_{po}(R_{po}(Q_b R_b)))$, which has been used elsewhere to model ceramic coatings on Mg substrates (Jamesh et al., 2012). Q_{po} and R_{po} represent the pore capacitance/resistance of the ceramic layer, and Q_b and R_b represent the base material double layer capacitance and polarisation resistance respectively. The addition of the coating increased the R_p for the Mg-Ca alloy to $6.5 \times 10^3 \Omega \cdot \text{cm}^2$, ~85 % lower than that of the CaP coated AZ91 alloy ($4.8 \times 10^4 \Omega \cdot \text{cm}^2$).

Visual observations of the samples during the coating process suggested that gas bubbles evolving from the surface of the samples were higher on the Mg-Ca alloy as compared to that from the AZ91 alloy. Since hydrogen evolution is the predominant cathodic reaction in Mg and Mg alloys (Song and Atrens, 1999), the gas bubbles must be hydrogen gas bubbles. In order to understand the difference in the phenomenon between the two alloys, the cathodic current density during the coating process was recorded and shown in Fig. 6.9. It can be clearly seen that the cathodic current density is much higher during the coating of the Mg-Ca alloy when compared to that of AZ91 alloy. This confirms that the hydrogen evolution was higher in the former. Further, the difference between the two alloys was quantified by integrating the cathodic current density with respect to time, resulting in the average charge density. Notably in Fig. 6.9

c, the cathodic charge density was significantly higher (~5 times) for the Mg-Ca alloy, which can be related to the higher degradation tendency of the coated Mg-Ca alloy compared to the coated AZ91 alloy.

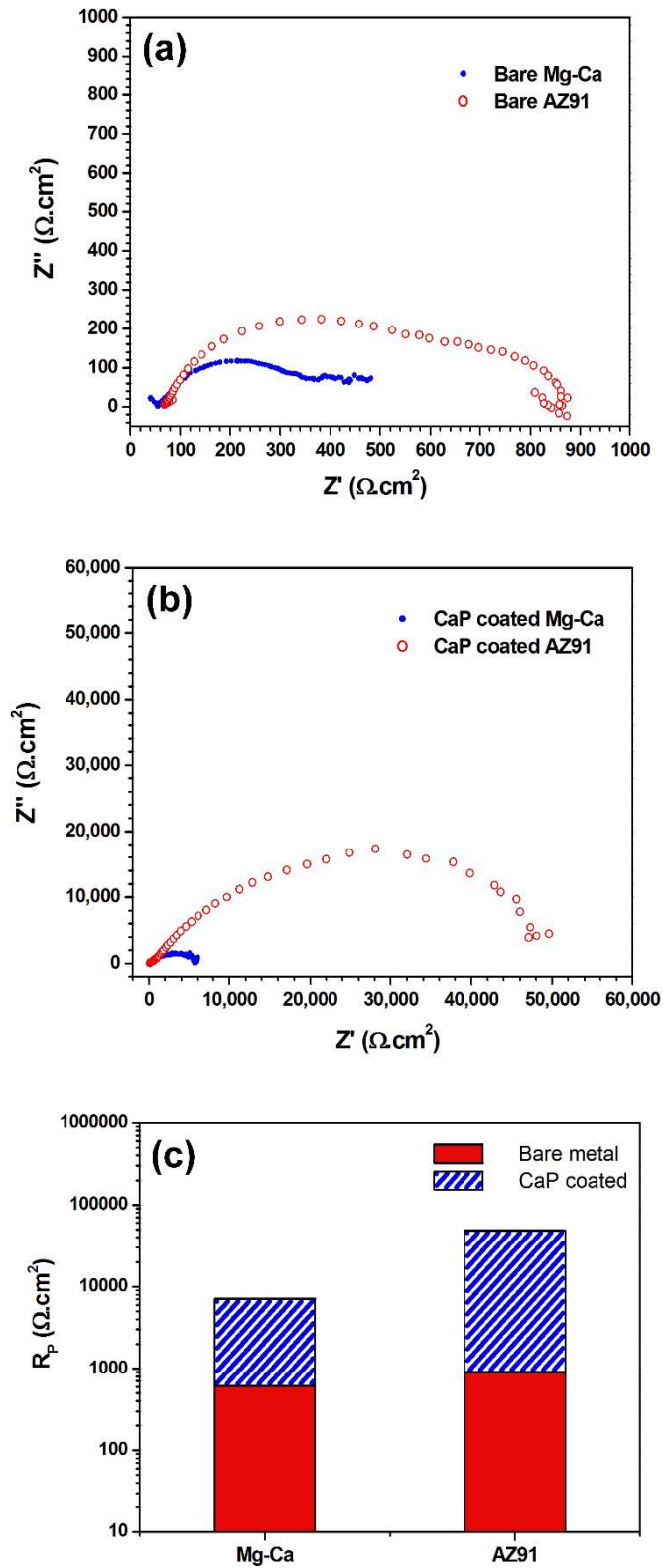


Figure 6.8 EIS plots of: (a) bare metals and (b) CaP coated metals; and (c) polarisation resistance (R_p) from EIS modelling (N=2).

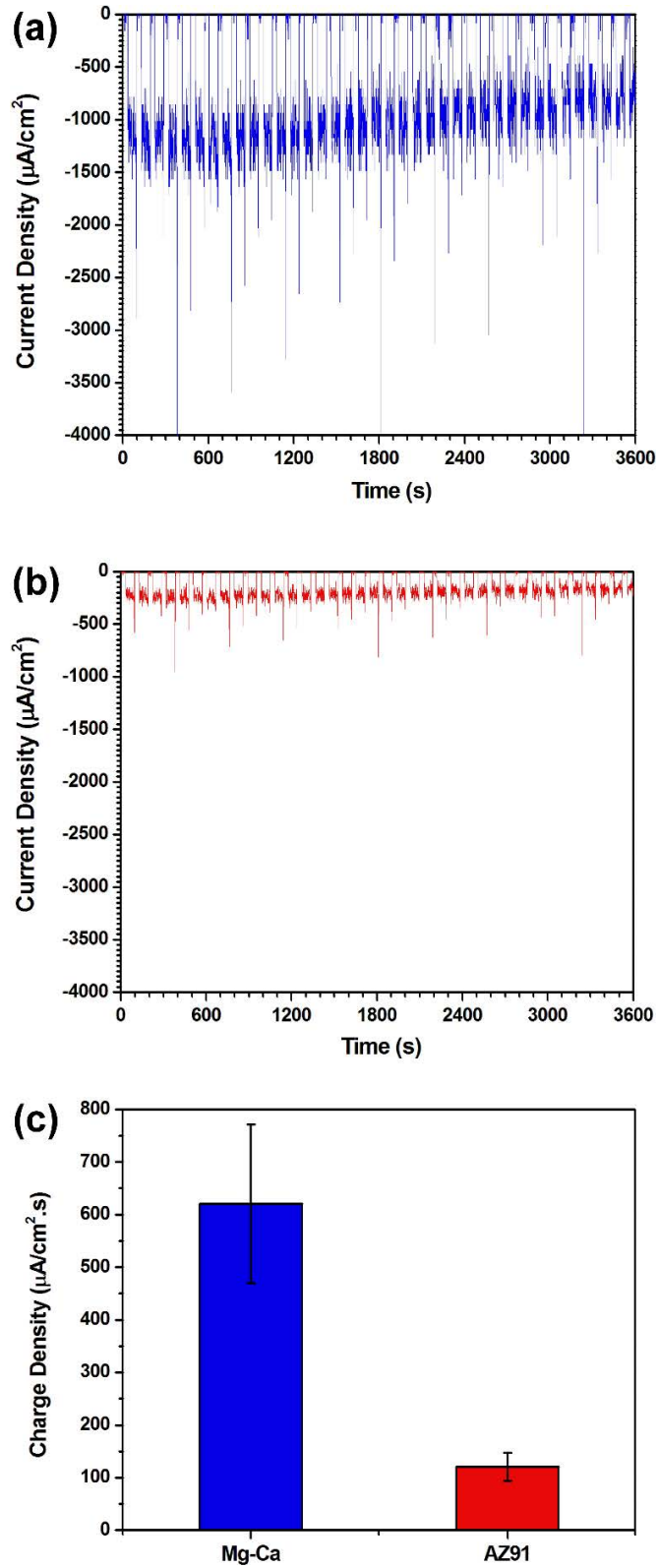


Figure 6.9 Cathodic current density recorded during the calcium phosphate coating on (a) Mg-Ca alloy, and (b) AZ91 alloy; and (c) average charge density for both the alloys during the coating process (N=2).

In general, Mg in an aqueous environment will produce a partially protective surface film comprised of both MgO and Mg(OH)₂. However, aluminium containing alloys, such as AZ91, have a third layer comprised of Al₂O₃, which accounts for the increase in degradation resistance when compared to pure Mg (Song and Atrens, 1999). Similarly, the Al₂O₃ protective layer would reduce the electrochemical reactions on the surface compared to an aluminium-free substrate, thus reduced the hydrogen evolution. While it is expected that this difference between the alloys would be prominent during the early stage of the coating, as the bare substrate is exposed to the electrolyte, results from this study suggest that the differences in cathodic reaction, due to differences in electrode composition, affect CaP nucleation which in turn influences the growth of the coating particles as well as the overall coating performance.

6.3.2 Dual Layer PEO/CaP coating

The previous results suggested that after only 72 h immersion, electrolyte was able to penetrate through the CaP layer. This resulted in only a marginal improvement in the long-term degradation rate. Since the limiting factor was the pore resistance, a more tightly packed CaP layer may provide better performance. Liu et al. (2011) chemically coated a CaP layer on top of a MAO coated pure Mg substrate. The authors reported a much lower volume of evolved hydrogen for the calcified sample when compared to the MAO sample. However, SEM images showed two regions, flake-like and porous spherical-shaped structures. This porosity may still allow for penetration of electrolyte through the coating layer and in contact with the Mg substrate. Recently, Alabbasi et al. (2014) electrochemically deposited CaP on a silicate-based PEO coated Mg substrate using a pulsed constant-current method. The authors report a 65 % reduction in the i_{corr} and a two order of magnitude increase in the R_p of the PEO-CaP when compared to pure Mg. The following results expanded on this work by electrochemically depositing CaP on a phosphate-based PEO layer on pure Mg using the pulsed potential method utilised in section 6.3.1.

Figure 6.10 shows the FTIR spectra for the PEO and PEO/CaP dual layer coatings, both prior to immersion and following 72 h immersion in SBF. The PEO showed a spectrum consistent with that in literature, showing only a single band at 1000 cm⁻¹, corresponding to phosphate. Following immersion in SBF, a hydroxide peak appeared at 1400 cm⁻¹, suggesting uptake of the aqueous electrolyte into the layer. The CaP

coated sample showed a spectrum consistent with the previous work. Visible are bands at 1631 cm^{-1} and 874 cm^{-1} , corresponding to hydroxide and carbonate groups, respectively. The strong bands at 1122 , 1052 and 984 cm^{-1} sample correspond to phosphates.

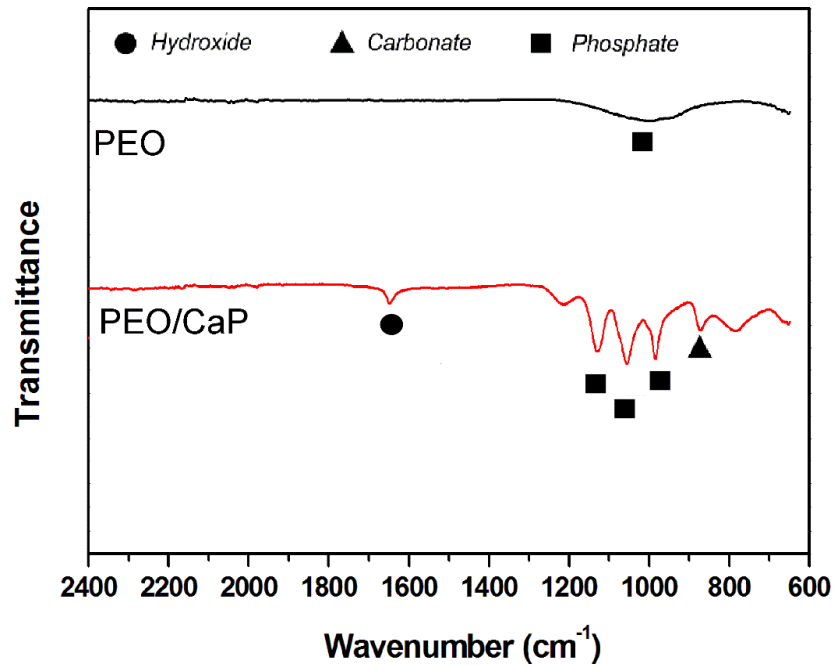


Figure 6.10 FTIR spectra of the PEO and PEO/CaP dual layers.

The SEM images in Plate 6.4 show typical morphologies of both the PEO and CaP structure. Clearly visible in Plate 6.1 (a, b) is the PEO microstructure, with the evenly distributed pores across the entire surface. Interestingly, the CaP layer in Plate 6.4 (c, d) shows a morphology somewhat similar to the CaP coated on Mg-Ca presented in Plate 6.3 (a, b). These particles were slightly smaller and more protruding than those produced on AZ91. This was explained by the higher cathodic current density on the Mg-Ca substrate increasing the hydrogen evolution and damaging the surface. However, the PEO layer would reduce the current density, and larger, flatter particles would be expected. The structure seen in Plate 6.4 (c, d) can instead be explained by the pores in the PEO layer acting as nucleation sites. An increased density in nucleation sites of the CaP would explain the smaller particle size. This further suggests that the CaP is not only formed directly on top of the MgO layer, but is also precipitating within the pores themselves.

The potentiodynamic polarisation curves of the two coatings are shown in Figure 6.11, and the electrochemical degradation parameters are shown in Table 6.3. The curves are shown against a bare Mg sample as a reference. The PEO layer showed a 65 % reduction of the corrosion current when compared to the bare Mg, from 23.5 to 8.3 $\mu\text{A}/\text{cm}^2$. Interestingly, the PEO also caused a shift in the corrosion potential of approximately 120 mV in the active direction, from -1.80 to -1.92 $V_{\text{AgAg/Cl}}$. The addition of the CaP layer onto the PEO had a positive effect on both the corrosion current and potential. The CaP layer reduced the corrosion current to 2.0 $\mu\text{A}/\text{cm}^2$, a 76 % reduction compared to the single PEO layer (or a 91 % reduction compared to the bare Mg). The corrosion potential was measured to be -1.51 $V_{\text{AgAg/Cl}}$. This suggests that the surface of the material is likely to be entirely CaP, which agrees with the SEM images as shown in Plate 6.4.

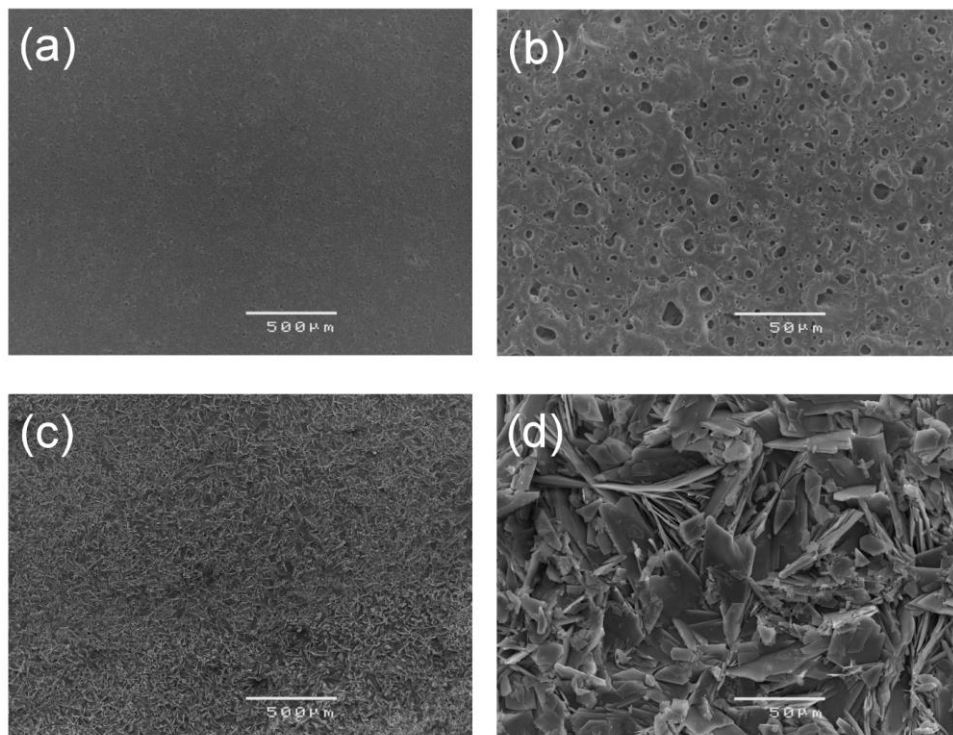


Plate 6.4 SEM images of the (a, b) PEO and (c, d) PEO/CaP dual layers.

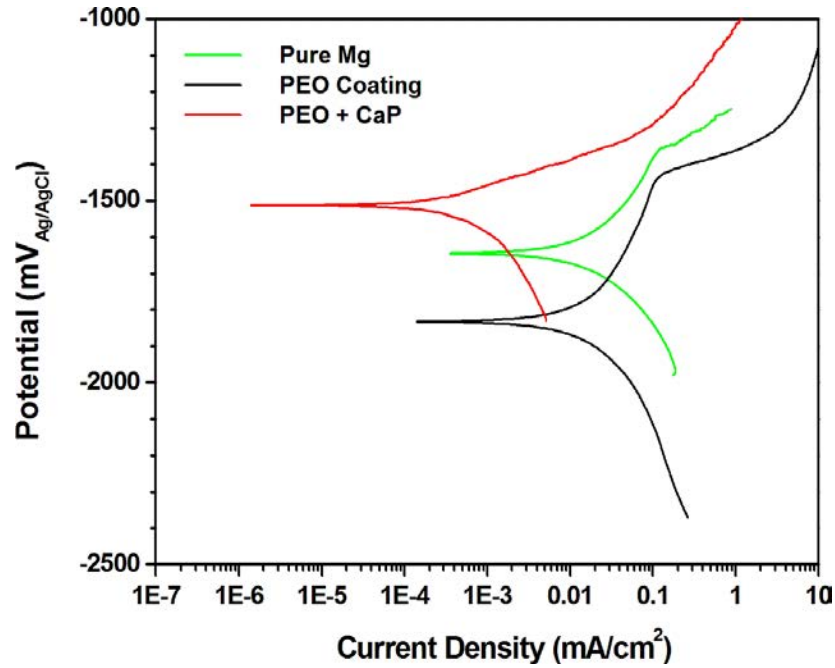


Figure 6.11 Potentiodynamic polarisation curves for bare Mg, PEO and PEO/CaP dual layer coatings.

Table 6.3

Electrochemical degradation parameters of Mg and its alloys obtained from potentiodynamic polarisation curves (N=2).

Sample	i_{corr} ($\mu\text{A}/\text{cm}^2$)	E_{corr} ($\text{V}_{\text{Ag}/\text{AgCl sat'd}}$)
Pure Mg	23.5 ± 3.6	-1.8 ± 0.02
PEO	4.5 ± 0.7	-1.92 ± 0.02
PEO + CaP	2.0 ± 0.6	-1.51 ± 2.6

Figure 6.12 shows the EIS plots of the PEO and PEO/CaP dual layer coatings over the 72 h immersion period. The R_p values obtained from these plots are shown with respect to time in Figure 6.13. The PEO layer had an initial R_p of approximately $3500 \Omega \cdot \text{cm}^2$, increasing to $7100 \Omega \cdot \text{cm}^2$ after 24 h, and slowly decreasing to $5600 \Omega \cdot \text{cm}^2$ after the full 72 h immersion period. From 2 h to 24 h immersion, the plots showed only a single layer capacitive loop. From 48 h onward, a second mid-frequency capacitive loop

becomes visible, suggesting that the coatings are only partially protective. The addition of the CaP particles onto the PEO layer significantly increased the R_p by an order of magnitude. The initial R_p was measured to be approximately $206 \text{ k}\Omega\cdot\text{cm}^2$, which slowly decreased to $38 \text{ k}\Omega\cdot\text{cm}^2$ after 72 h immersion. All the dual layer plots showed only a single capacitive loop, which implies that there was very little coating breakdown or penetration of the electrolyte when compared to the single layer PEO coatings.

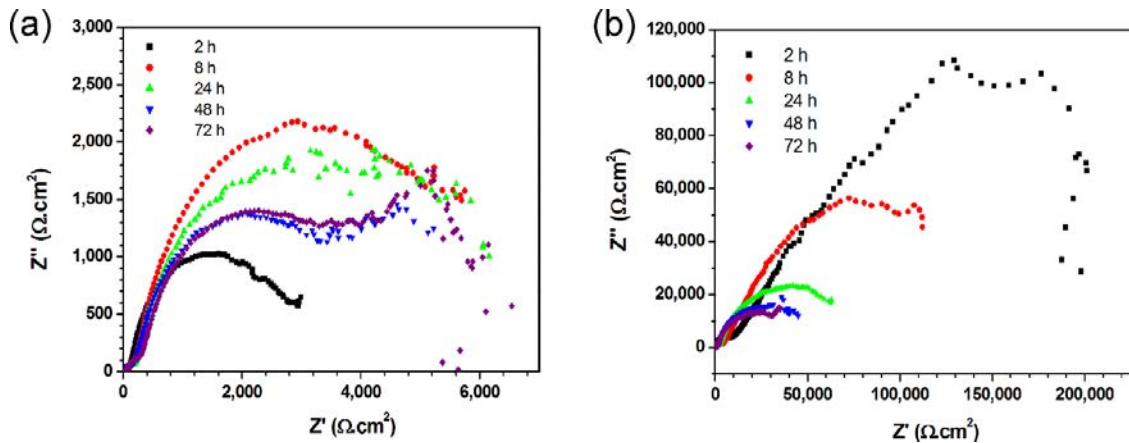


Figure 6.12 EIS plots over a 72 h immersion period in SBF for (a) PEO and (b) PEO/CaP dual layer coatings.

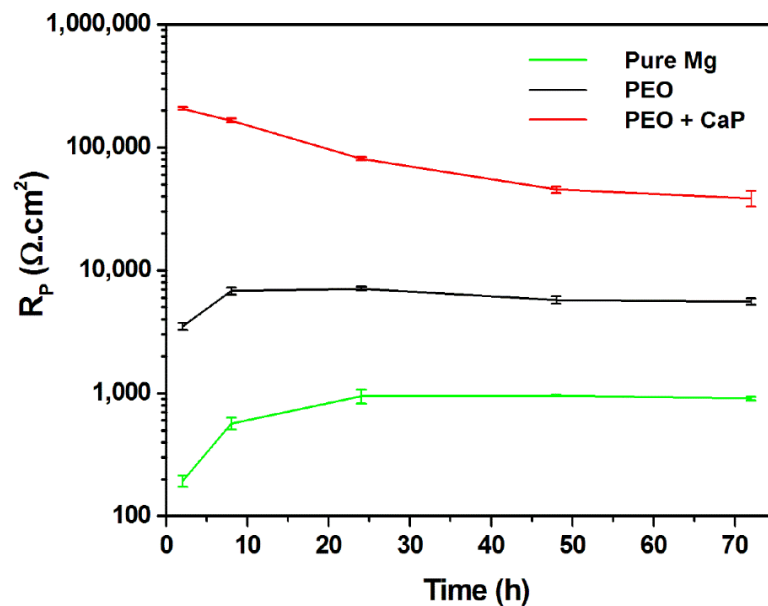


Figure 6.13 R_p vs. Time for bare Mg, PEO and PEO/CaP dual layers over a 72 h immersion period in SBF (N=2).

Figure 6.14 shows the FTIR spectra of the PEO and dual layer coating following immersion, and Plate 6.5 shows the resultant SEM images. For PEO, the most notable change is the appearance of a carbonate band at 1435 cm^{-1} . For the dual layer coating, the hydroxide and carbonate bands at 1435 cm^{-1} and 874 cm^{-1} are still visible, with extra carbonate bands appearing at 1488 cm^{-1} and 1631 cm^{-1} . The strong phosphate bands have also merged, showing only a broad phosphate band at approximately 1000 cm^{-1} . These spectra agree with the data presented by Liu et al. (2011). This reduction in bands strongly suggests that there has been a change in the coating structure, due to either incongruent dissolution and/or precipitation of new CaP phases onto the surface.

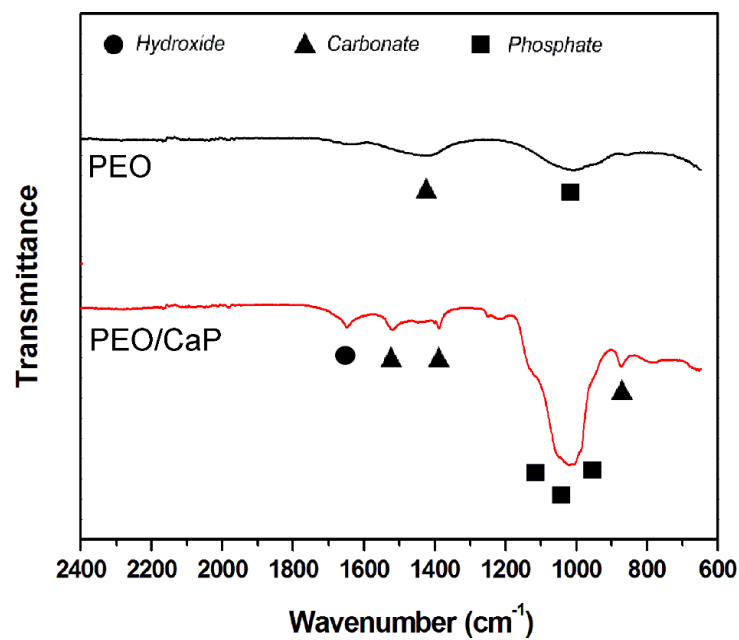


Figure 6.14 FTIR spectra of the PEO and PEO/CaP dual layers following 72 h immersion in SBF.

There are also some noticeable changes to the microstructures of the coatings. Firstly, the PEO layer shown in Plate 6.5 (a, b) seems relatively unattacked, with only some areas of degradation products forming across some pores. This is consistent with the accepted degradation behaviour of this type of coating, that is, permeation of the electrolyte through the porous outer layer and subsequent attack on the more compact, inner layer. In fact, this is a major limitation of the PEO type coatings; the porous outer layer allows rapid permeation of the electrolyte while providing relatively little resistance to degradation, instead relying on the much thinner inner layer to protect the substrate. The CaP coated layer in Plate 6.5 (c, d) shows signs of attack across the entire surface, exposing floret-like regions. However, there are no areas of particularly

heavy localised attack, suggesting that the coating was both well packed and quite even. Furthermore, the surface, while slightly damaged, shows no signs of cracking such as that seen in Plate 6.2. This suggests that the penetration of electrolyte through the coating was strongly reduced when compared to the single layer CaP coating.

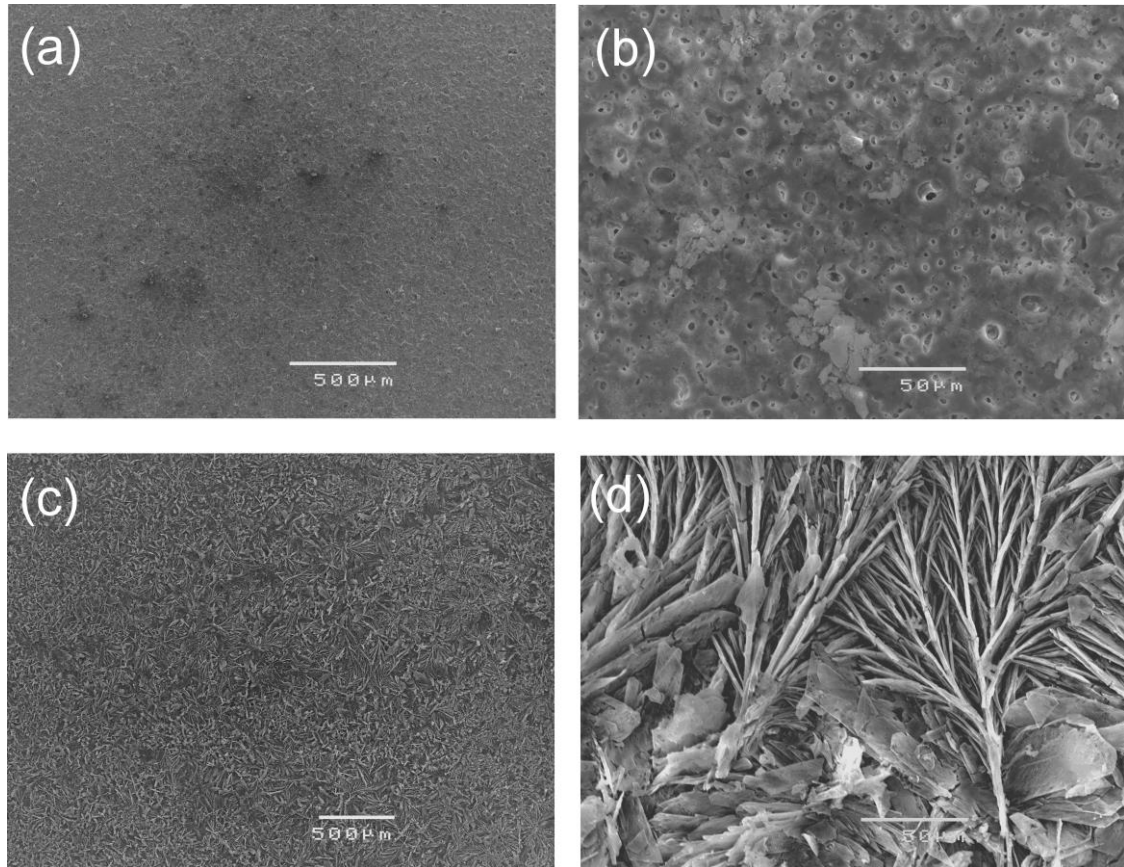


Plate 6.5 SEM images of the (a, b) PEO and (c, d) PEO/CaP dual layers following 72 h immersion in SBF.

6.3.3 Triple layer PEO/CaP/PLLA coating

Section 6.3.2 showed that the addition of the CaP layer on the PEO/Mg substrate was very effective in delaying the general and localised degradation of pure Mg by heavily reducing the penetration of electrolyte through the coating. However, the drop in R_p over the immersion period suggests that there is still some degree of electrolyte penetration. To further improve the porous resistance this work employed spin coating technique to produce a third, polymeric layer on top of the previous dual layer coating. Srinivisan et al. (2010a) produced a duplex coating of poly(etherimide) on a PEO coated Mg substrate. The authors reported that the polymer was effective in filling the PEO pores and provided enhanced degradation resistance. Similarly, Arrabal et al.

(2012) sealed a PEO coated Mg alloy with a polyester-based polymer. The polymer seal significantly improved the degradation resistance when compared to the single PEO layer. However, to date no authors have investigated the combined effects of both CaP and polymer sealing of a PEO coated Mg substrate. This work spin coating technique to coat a PLLA layer on the dual layer coating to produce a hybrid, triple layer coating.

The SEM images of the triple layer coating in Plate 6 (a-c) shows the polymer layer is quite evenly distributed across the surface. The structure of the underlying CaP layer is still slightly visible, but the even distribution of pores across the entire surface indicates that there are no polymer-free regions. Figure 6.15 compares the potentiodynamic polarisation curves of the dual and triple layer coatings, and the electrochemical degradation parameters can be seen in Table 6.4. The addition of the PLLA layer shifted the corrosion potential 80 mV in the noble direction, from -1.51 to -1.43 $V_{AgAg/Cl}$. Interestingly, the triple layer curve shows a slightly higher cathodic current when compared to the dual layer coating. However, the anodic current is markedly lower. This corresponds to a ~40 % decrease in the corrosion current compared to a previously examined dual layer coating, and a ~99 % reduction compared to pure Mg. Interestingly, a breakdown potential is visible at ~1200 $mV_{Ag/AgCl}$, which was notably absent in the dual layer coating.

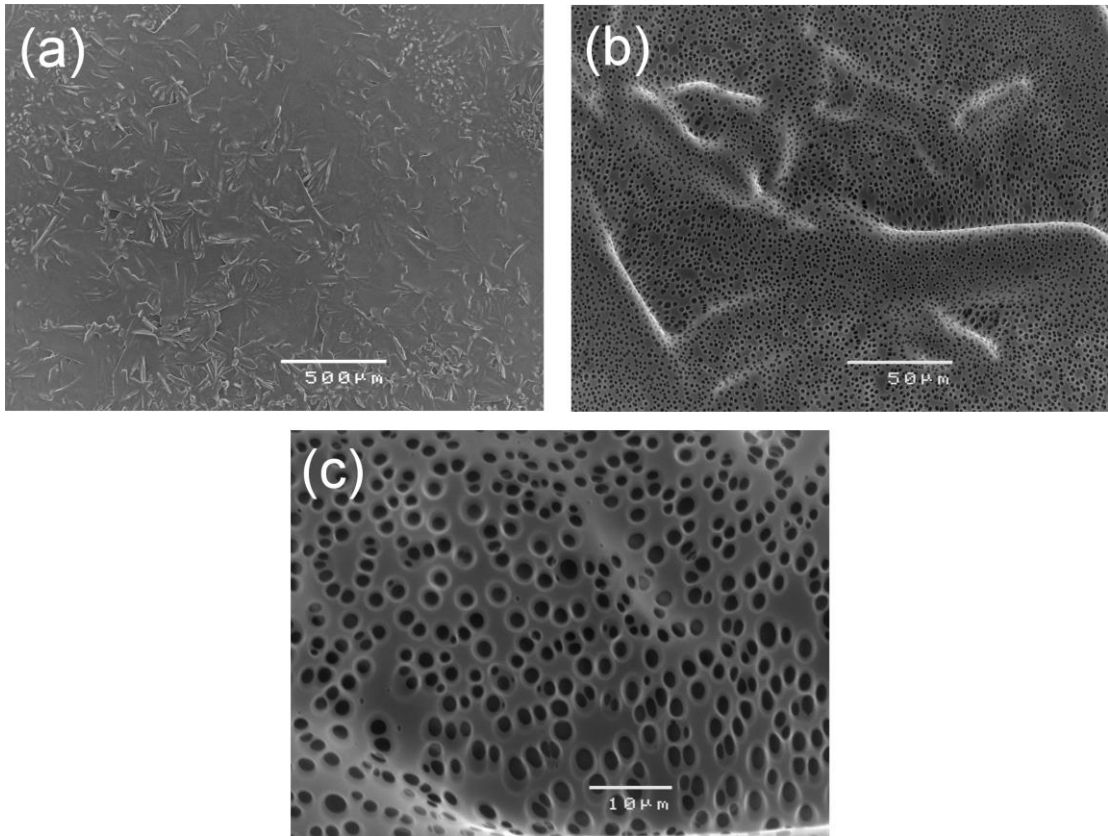


Plate 6.6 SEM images of the triple layer hybrid coatings.

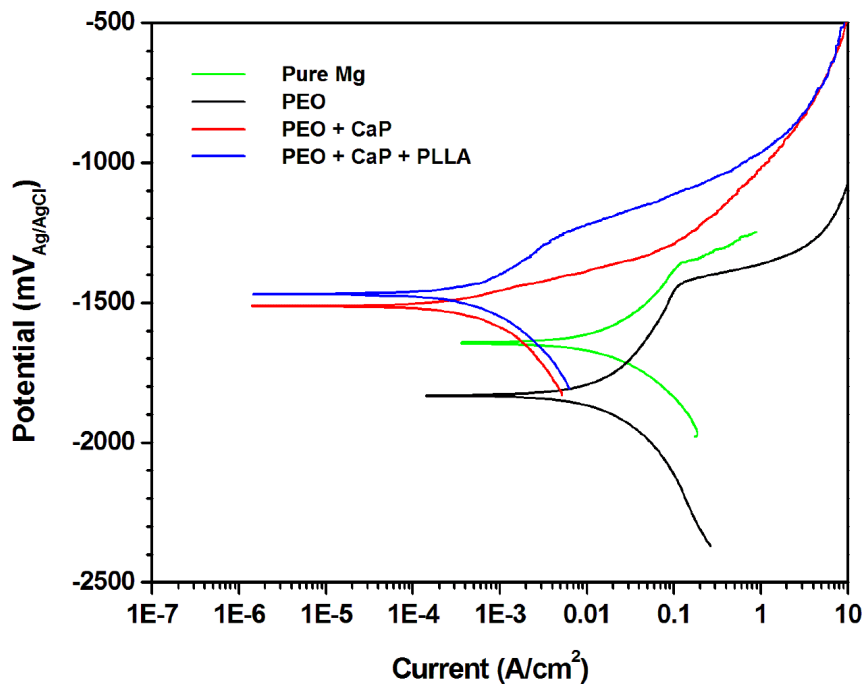


Figure 6.15 Potentiodynamic polarisation curves for bare Mg, PEO, PEO/CaP dual layer, and triple layer hybrid coatings.

Table 6.4: Electrochemical degradation parameters of pure Mg, PEO, dual layer, and triple layer coatings obtained from potentiodynamic polarisation curves (N=2).

Sample	E_{corr} (V _{Ag/AgCl sat'd})	i_{corr} ($\mu\text{A}/\text{cm}^2$)	i_{bd} ($\mu\text{A}/\text{cm}^2$)
Pure Mg	-1.80 ± 0.02	23.5 ± 3.6	96.2 ± 4.9
PEO	-1.92 ± 0.02	8.3 ± 3	93.8 ± 8.2
PEO + CaP	-1.51 ± 2.6	0.35 ± 0.16	33 ± 9.9
PEO + CaP + PLLA	-1.43 ± 0.05	0.20 ± 0.02	7.2 ± 2.0

Figure 6.16 shows the EIS plots for the dual and triple layer coatings over the 72 h immersion period. The calculated R_P following equivalent circuit modelling of these plots is shown in Fig 6.17. The initial R_P of the triple layer coating was almost an order of magnitude larger than the dual layer coating, at a value of approximately 960 $\text{k}\Omega\cdot\text{cm}^2$. As with the dual layer coating, the R_P dropped over time due to electrolyte permeation. However, the rate of decrease was markedly higher than the dual layer coating, resulting in the R_P dropping below that of the dual layer coating between 60-72 h immersions. The initial 2 h plot shows both high and mid-frequency capacitive loops. This indicates that there is most likely rapid permeation of the electrolyte through the top layer of the polymer. Interestingly, from 8 h immersion onwards, the plots are similar in shape to the dual layer plots shown in Fig. 6.12 (b). That is, only a single capacitive loop is visible, with no low frequency inductive loop. Since the R_P of the triple layer is higher than that of the dual layer coating until ~60 h immersion, it would appear that the PLLA has a positive effect on the coating for low immersion times beyond being a physical barrier. This can be explained by the polymer having effectively sealed the remaining pores of the dual layer structure. The triple layer coating after 72 h immersion is shown in Plate 6.7. The surface shows some signs physical degradation, however the porous structure visible in Plate 6.6 is still present. Small amounts of polymer thinning have made visible the distinct underlying CaP structure, but the grains themselves remain unexposed. This suggests that the loss in resistance is due to bulk erosion of the polymer, as expected.

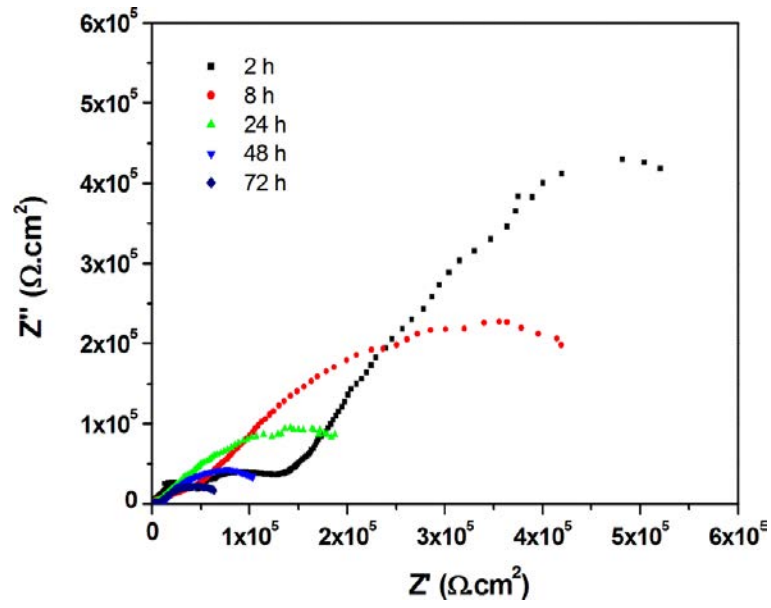


Figure 6.16 EIS plots over a 72 h immersion period in SBF for the triple layer hybrid coatings.

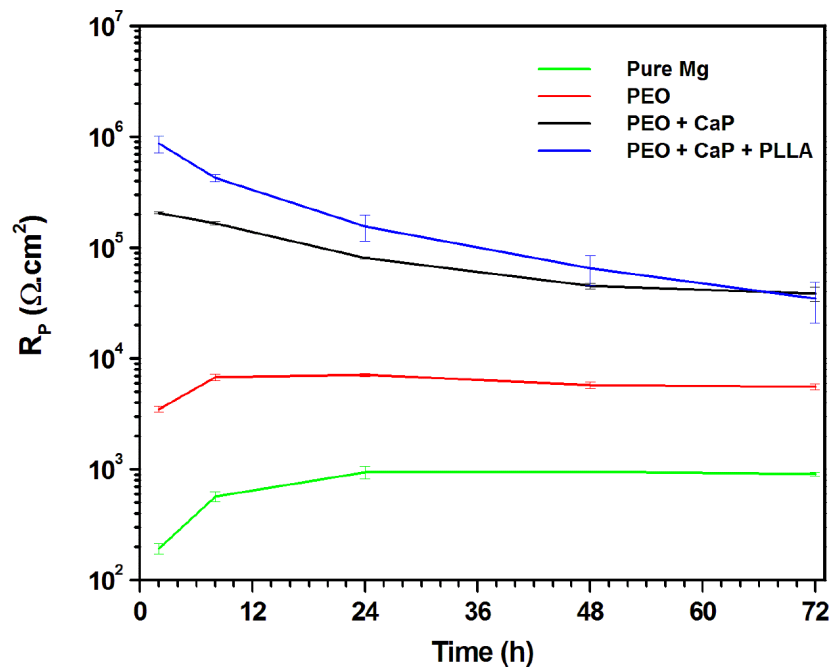


Figure 6.17 R_p vs. Time for bare Mg, PEO, PEO/CaP dual layer, and triple layer hybrid coatings over a 72 h immersion period in SBF ($n=2$).

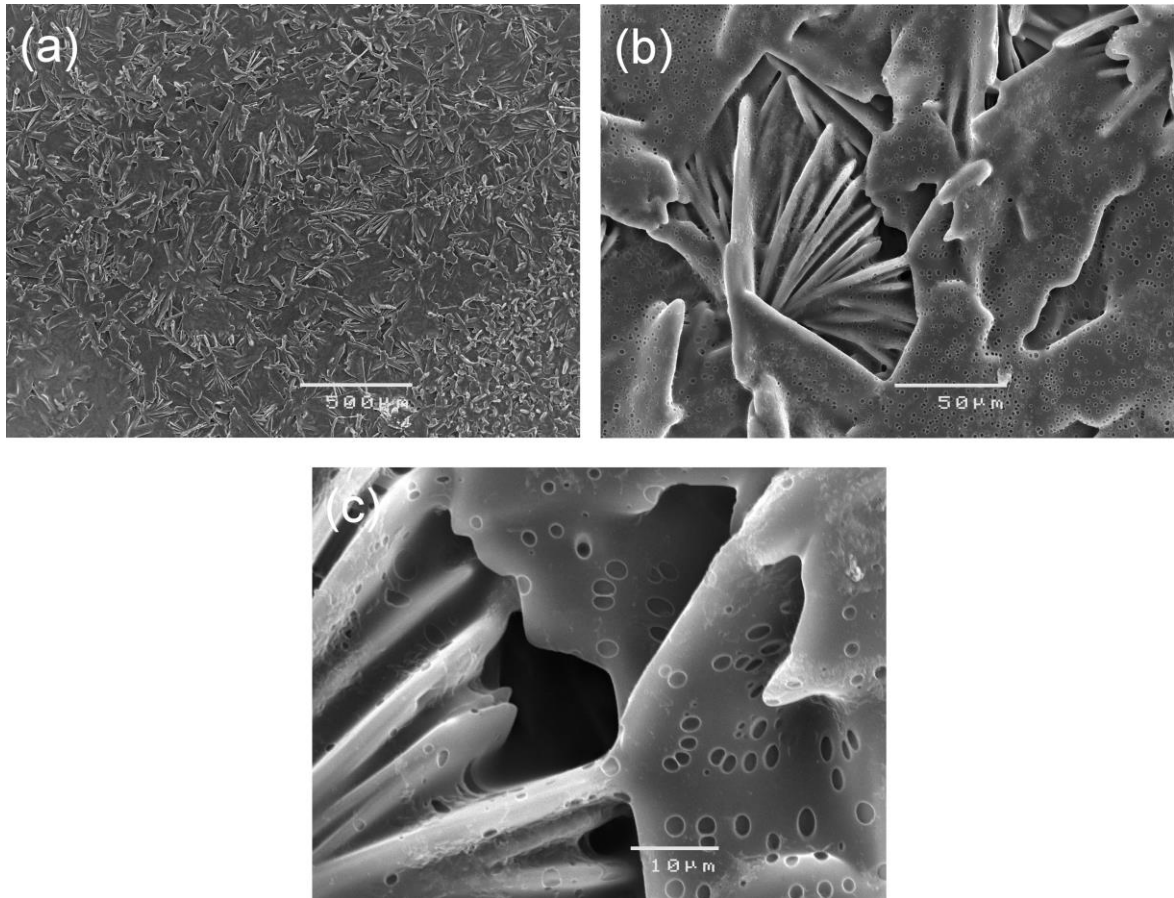


Plate 6.7 SEM images of the triple layer hybrid coatings following 72 h immersion in SBF.

Since the precipitation/dissolution process of the CaP layer is so dependent on pH, a final layer that alters the pH can be used to tailor the overall resistance. In this case, a porous polymer layer (PLLA) was added over the previous hybrid layer. The PLLA layer has a much higher degradation resistance than typical bioceramic materials, and releases acidic degradation products. However, the high porosity allows for rapid permeation, allowing the electrolyte to come into contact with the underlying ceramic layer. Further, since the primary form of degradation is bulk, rather than surface degradation (Nair and Laurencin, 2007), there will be a pH drop throughout the polymer layer. This pH drop close the CaP layer increases the solubility of calcium and phosphate ions, increasing the rate of CaP dissolution (Chow, 2009). This effect is compounded over time since the lactic acid is produced more rapidly than it is removed from the surface, and the overall degradation resistance will decrease more rapidly than that of the dual layer coating alone. While this effect may seem to be detrimental, it

may allow researchers to specifically tailor the over degradation rate of the material by varying certain coating properties such as polymer thickness and porosity, as well as PLLA/CaP ratios.

6.4 Conclusions

This work produced three different coatings on Mg-based substrates: a single layer CaP, a dual layer PEO/CaP, and a triple layer PEO/CaP/PLLA. The single layer CaP coating was electrochemically deposited on an Mg-Ca substrate using a pulse potential waveform. EIS testing showed an initial improvement in the R_P from $\sim 400 \Omega \cdot \text{cm}^2$ to $\sim 6500 \Omega \cdot \text{cm}^2$, approximately 15 times higher. Following 72 h immersion in SBF, the R_P of the bare Mg-Ca increased to $\sim 700 \Omega \cdot \text{cm}^2$ due to partial passive effects, but the R_P of the CaP coating reduced to $\sim 1200 \Omega \cdot \text{cm}^2$, only $\sim 70 \%$ higher than that of the bare alloy. This rapid drop can be attributed to permeation of the electrolyte through the coating rather than coating breakdown, since CaPs have a significantly lower dissolution rate than Mg alloys. This is confirmed by open circuit potential measurements, which showed a relatively constant $\sim 100 \text{ mV}$ difference between the coated and uncoated samples across the entire immersion period, suggesting that the surface of the coating is largely unchanged.

The performance of the coatings was also found to depend on the cathodic activity of the Mg substrate during the electrochemical formation of the CaP coating. SEM analysis showed that the CaP coating on a relatively lower degradation resistant alloy, Mg-Ca, was less densely packed as compared to that on AZ91 alloy, and the coated Mg-Ca exhibited an R_P of $\sim 85 \%$ lower than that of the coated AZ91 alloy. This can be attributed to the higher cathodic charge density, which is due to the hydrogen evolution, during the coating process on Mg-Ca alloy as compared to that of the AZ91 alloy.

To reduce the porosity of the single layer CaP, a dual layer coating was produced, with a PEO coating acting as a scaffold for an electrochemically deposited CaP coating. This dual layer coating showed a much higher degradation resistance than either layer did separately. The single PEO layer improved the R_P of the pure Mg by an order of magnitude, and the addition of the second CaP layer added another order of magnitude improvement. This was attributed to the pores of the PEO acting as nucleation sites for

the CaP, allowing for a tight packing of the CaP particles, and thereby reducing the rate of electrolyte penetration through the coating.

A third, PLLA layer was then added to further improve the degradation resistance of the coating. The PLLA layer was able to improve the R_p by three orders of magnitude for low immersion times when compared to pure Mg. However, from ~60-72 h immersion, the triple layer coating displayed an average R_p lower than that of the dual layer. While the polymer did appear to have an effect in regards to sealing the pores of the underlying ceramic, due to the highly porous nature of the PLLA layer, which allowed the electrolyte to penetrate through over time. The subsequent bulk erosion of the PLLA released acidic products that damaged the CaP/PEO layer, hence slightly reducing the overall degradation resistance.

Chapter. 7 Conclusions and Recommendations

7.1 Outcomes

7.1.1 *Influence of surface roughness*

Surface roughness was found to play a critical role in the corrosion behaviour of AZ91 Mg alloy in chloride-containing environment by influencing the initiation of pitting attack. The electrochemical experiments showed that an increase in the surface roughness of the alloy affects the passivation tendency and consequently increases the pitting susceptibility of the alloy. However, when the passivity of the alloy is disturbed then the influence of surface roughness on the pitting degradation susceptibility becomes less significant. Although the surface roughness of AZ91 Mg alloy did not show any significant effect on its general degradation resistance under long-term exposure in SBF, it played a critical role on the localised degradation behaviour of the alloy. A rougher surface reduced the incubation time for pitting degradation of the alloy. Moreover, the severity of the localised degradation of the alloy was also high in the rough surface alloy as compared to the smooth surface alloy.

7.1.2 *Influence of the microgalvanic effect*

Since pure magnesium is always anodic to its secondary precipitates, microgalvanic effects are known to influence the degradation behaviour of Mg alloys, potentially resulting in semi-stable secondary phases. This work found that while microgalvanic effects will accelerate dissolution of the α matrix, the β precipitates will degrade acceptably rapidly once these effects are removed. Galvanic coupling of β -phase ($\text{Mg}_{17}\text{Al}_{12}$) with pure Mg in SBF resulted in the formation of carbonated calcium phosphate on the β -phase. While the calcium phosphate layer initially increased the degradation resistance of the β -phase, the layer rapidly degraded once the galvanic coupling was removed. Within 48 h immersion in SBF, the degradation resistance of the β -phase began to approach that of pure Mg. The results suggest that under long-term immersion period in SBF, the degradation resistance of the β -phase will decrease and eventually the β -phase will dissolve in body fluid as the micro-galvanic effects are reduced due to complete dissolution of the Mg matrix around the β -phase.

7.1.3 Degradation behavior of single layer CaP coatings

A CaP coating was electrochemically deposited on an Mg-Ca substrate using a pulse potential waveform. EIS testing showed an initial improvement of approximately 15 times in the R_p . Following 72 h immersion in SBF, the R_p of the CaP coating reduced to $\sim 1200 \Omega \cdot \text{cm}^2$, only $\sim 70\%$ higher than that of the bare alloy. This decrease can be attributed to penetration of the electrolyte through the porous structure. This is confirmed by open circuit potential measurements, which showed a relatively constant ~ 100 mV difference between the coated and uncoated samples across the entire immersion period, suggesting that the surface of the coating is largely unchanged.

7.1.4 Influence of the cathodic activity of Mg alloys on the electrochemical deposition of calcium phosphate

The cathodic activity of Mg alloys was found to play a critical role on the electrochemical formation of CaP coatings. The CaP coating on a relatively lower degradation resistant alloy, Mg-Ca, was less densely packed as compared to that on AZ91 alloy. As a result, the coated Mg-Ca exhibited an R_p of $\sim 85\%$ lower than that of the coated AZ91 alloy. This can be attributed to the higher cathodic charge density, which is due to the hydrogen evolution, during the coating process on Mg-Ca alloy as compared to that of the AZ91 alloy.

7.1.5 Degradation behaviour of multilayer coatings on Mg

This study also investigated the in vitro degradation performance of dual and triple layer hybrid coatings on Mg in order to reduce the porosity of the single layer CaP and improve the overall performance. A dual layer coating was produced, with a PEO coating acting as a scaffold for an electrochemically deposited CaP coating. The single PEO layer improved the R_p of the pure Mg by an order of magnitude, and the addition of the second CaP layer added another order of magnitude improvement. This was attributed to the pores of the PEO acting as nucleation sites for the CaP, allowing for a tight packing of the CaP particles, and thereby reducing the rate of electrolyte penetration through the coating.

Potentiodynamic polarisation of the triple layer coating showed a $\sim 40\%$ decrease in the corrosion current compared to a previously examined dual layer coating, and a $\sim 99\%$

reduction compared to pure Mg. EIS revealed that the R_p was significantly higher for low immersion times, due to the high surface resistance of the polymeric layer. During the immersion period, the electrolyte was able to penetrate the highly porous polymer layer, allowing for the bulk erosion to take place. The subsequent release of the acidic products accelerated the dissolution of the underlying CaP layer. This resulted in the triple layer coating having a lower R_p than the dual layer coating after 60-72 h immersion in SBF.

7.2 Recommendations for Future Work

This work has provided a platform for the development of a novel multilayer coating for the improvement of an Mg substrate for use as a biodegradable biomaterial. However, there is more work required. The following are avenues for future research required in order to achieve this.

- (1) Optimisation of coating parameters, in particular the polymer layer. The triple layer showed that the PLLA layer can be utilised to modify the long-term degradation behaviour of the dual ceramic layer. Optimisation of polymer parameters such as composition, molecular weight and porosity require further investigation.
- (2) Post-degradation mechanical testing. This work focussed completely on the electrochemical degradation behaviour without consideration to the mechanical integrity of the implants. Since Mg is particularly susceptible to localised degradation, it is imperative that this work be coupled with an evaluation of the mechanical integrity of the material over longer immersion times.
- (3) Biocompatibility and cytocompatibility testing and *in vivo* experimentation. Biocompatibility was outside the scope of this work, but it is a vital step in producing novel biomaterials.

References

- Abidin, N. Z., Martin, D., Atrens, A. (2011). "Corrosion of high purity Mg, Mg₂Zn_{0.2}Mn, ZE41 and AZ91 in Hank's solution at 37° C." *Corrosion Science*, 53, 3542-3556.
- Alabbasi, A., Liyanaarachchi, S., Kannan, M. B. (2012). "Polylactic acid coating on a biodegradable magnesium alloy: An in vitro degradation study by electrochemical impedance spectroscopy." *Thin Solid Films*, 520, 6841-6844.
- Alabbasi, A., Kannan, M. B.; Walter, R., Störmer, M., Blawert, C. (2013). "Performance of pulsed constant current silicate-based PEO coating on pure magnesium in simulated body fluid." *Materials Letters*, 106, 18-21.
- Alabbasi, A., Kannan, M. B., Blawert, C. (2014). "Dual layer inorganic coating on magnesium for delaying the biodegradation for bone fixation implants." *Materials Letters*, 124, 188-191.
- Alvarez, R. B., Martin, H. J., Horstemeyer, M. F., Chandler, M. Q., Williams, N., Wang, P. T., Ruiz, A. (2010). "Corrosion relationships as a function of time and surface roughness on a structural AE44 magnesium alloy." *Corrosion Science*, 52, 1635-48.
- Ambat, R., Aung, N., Zhou, W. (2000). "Evaluation of microstructural effects on corrosion behaviour of AZ91D magnesium alloy." *Corrosion Science*, 42, 1433-1455.
- Arrabal, R., Matykina, E., Viejo, F., Skeldon, P., Thompson, G. (2008). "Corrosion resistance of WE43 and AZ91D magnesium alloys with phosphate PEO coatings." *Corrosion Science*, 50, 1744-1752.
- Arrabal, R., Mota, J., Criado, A., Pardo, A., Mohedano, M., Matykina, E. (2012). "Assessment of duplex coating combining plasma electrolytic oxidation and polymer layer on AZ31 magnesium alloy." *Surface and Coatings Technology*, 206, 4692-4703.
- Athanasίου, K. A., Agrawal, C. M., Barber, F. A., Burkhart, S. S. (1998). "Orthopaedic applications for PLA-PGA biodegradable polymers." *Arthroscopy: The Journal of Arthroscopic & Related Surgery*, 14, 726-737.

Atrens, A., Song, G., Liu, M., Shi, Z., Cao, F., Dargusch, M. S. (2015). "Review of recent developments in the field of magnesium corrosion." *Advanced Engineering Materials*, 17, 400-453.

Avedesian, M. M., Baker, H., (1999). "ASM specialty handbook: magnesium and magnesium alloys." ASM international.

Barrère, F., Layrolle, P., Van Blitterswijk, C., De Groot, K. (1999). "Biomimetic calcium phosphate coatings on Ti6Al4V: a crystal growth study of octacalcium phosphate and inhibition by Mg^{2+} and HCO_3^- ." *Bone*, 25, 107S-111S.

Barrère, F., Layrolle, P., Van Blitterswijk, C., De Groot, K. (2001). "Biomimetic coatings on titanium: a crystal growth study of octacalcium phosphate." *Journal of Materials Science: Materials in Medicine*, 12, 529-534.

Barrère, F., Van Blitterswijk, C., De Groot, K. (2002). "Layrolle P. Nucleation of biomimetic Ca-P coatings on Ti6Al4V from a SBF× 5 solution: influence of magnesium." *Biomaterials*, 23, 2211-2220.

Barrère, F., Van der Valk, C., Meijer, G., Dalmeijer, R., De Groot, K., Layrolle, P. (2003). "Osteointegration of biomimetic apatite coating applied onto dense and porous metal implants in femurs of goats." *Journal of Biomedical Materials Research Part B: Applied Biomaterials*, 67, 655-665.

Barrere, F., Van Der Valk, C., Dalmeijer, R., Van Blitterswijk, C., De Groot, K., Layrolle, P. (2003a). "In vitro and in vivo degradation of biomimetic octacalcium phosphate and carbonate apatite coatings on titanium implants." *Journal of Biomedical Materials Research Part A*, 64, 378-387.

Barrère, F., Van Blitterswijk, C. A., De Groot, K. (2006). "Bone regeneration: molecular and cellular interactions with calcium phosphate ceramics." *International Journal of Nanomedicine*, 1, 317-332.

Bergsma, J., Rozema, F., Bos, R., Boering, G., De Bruijn, W., Pennings, A. (1995). "In vivo degradation and biocompatibility study of in vitro pre-degraded as-polymerized polylactide particles." *Biomaterials*, 16, 267-274.

- Berzina-Cimdina, L., Borodajenko, N. (2012). "Research of calcium phosphates using fourier transform infrared spectroscopy." in: *Infrared Spectroscopy- Materials Science, Engineering and Technology*, InTech, 123-149.
- Berthon, G. (2002). "Aluminium speciation in relation to aluminium bioavailability, metabolism and toxicity." *Coordination Chemistry Reviews*, 228, 319-341.
- Best, S., Porter, A., Thian, E., Huang, J. (2008). "Bioceramics: past, present and for the future." *Journal of the European Ceramic Society*, 28, 1319-1327.
- Bi, Y., Van De Motter, R. R., Ragab, A. A., Goldberg, V. M., Anderson, J. M., Greenfield, E. M. (2001) "Titanium particles stimulate bone resorption by inducing differentiation of murine osteoclasts." *The Journal of Bone and Joint Surgery*, 83, 501-501.
- Bigi, A., Boanini, E., Botter, R., Panzavolta, S., Rubini, K. (2002). "α-Tricalcium phosphate hydrolysis to octacalcium phosphate: effect of sodium polyacrylate" *Biomaterials*, 23, 1849-1854.
- Bigi, A., Bracci, B., Cuisinier, F., Elkaim, R., Fini, M., Mayer, I., Mihailescu, I., Socol, G., Sturba, L., Torricelli, P. (2005). "Human osteoblast response to pulsed laser deposited calcium phosphate coatings." *Biomaterials*, 26, 2381-2389.
- Boanini, E., Gazzano, M., Bigi, A. (2010). "Ionic substitutions in calcium phosphates synthesized at low temperature" *Acta Biomaterialia*, 6, 1882-1894.
- Boinet, M., Verdier, S., Maximovitch, S., Dalard, F. (2005). "Plasma electrolytic oxidation of AM60 magnesium alloy: Monitoring by acoustic emission technique. Electrochemical properties of coatings." *Surface and Coatings Technology*, 199, 141-149.
- Bogdanski, D., Epple, M., Esenwein, S., Muhr, G., Petzoldt, V., Prymak, O., Weinert, K., Köller, M. (2004). "Biocompatibility of calcium phosphate-coated and of geometrically structured nickel--titanium (NiTi) by in vitro testing methods." *Materials Science and Engineering: A*, 378, 527-531.

Brown, W., Eidelman, N., Tomazic, B. (1987). "Octacalcium phosphate as a precursor in biomineral formation." *Advances in Dental Research*, 1, 306-313.

Von Burkersroda, F., Schedl, L., Göpferich, A. (2002) "Why degradable polymers undergo surface erosion or bulk erosion." *Biomaterials*, 23, 4221-4231.

Cabrini, M., Cigada, A., Rondelli, G., Vicentini, B. (1997). "Effect of different surface finishing and of hydroxyapatite coatings on passive and corrosion current of Ti6Al4V alloy in simulated physiological solution." *Biomaterials*, 18, 783-7.

Cai, Y., Zhang, S., Zeng, X., Wang, Y., Qian, M., Weng, W. (2009) "Improvement of bioactivity with magnesium and fluorine ions incorporated hydroxyapatite coatings via sol-gel deposition on Ti6Al4V alloys." *Thin Solid Films*, 517, 5347-5351.

Chandrasekar, M., Pushpavanam, M. (2008). "Pulse and pulse reverse plating—Conceptual, advantages and applications." *Electrochimica Acta*, 53, 3313-3322.

Chang, J., Guo, X., He, S., Fu, P., Peng, L., Ding, W. (2008). "Investigation of the corrosion for Mg-xGd-3Y-0.4 Zr (x= 6, 8, 10, 12wt%) alloys in a peak-aged condition." *Corrosion Science*, 50, 166-177.

Chen, Y., Song, Y., Zhang, S., Li, J., Zhao, C., Zhang, X. (2011) "Interaction between a high purity magnesium surface and PCL and PLA coatings during dynamic degradation." *Biomedical Materials*, 6, 025005.

Chen, Y., Xu, Z., Smith, C., Sankar, J. (2014). "Recent advances on the development of magnesium alloys for biodegradable implants." *Acta Biomaterialia*, 10, 4561-4573.

Chia, T. L., Easton, M., Zhu, S., Gibson, M., Birbilis, N., Nie, J. (2009). "The effect of alloy composition on the microstructure and tensile properties of binary Mg-rare earth alloys." *Intermetallics*, 17, 481-490.

Chow, L. (2009). "Next generation calcium phosphate-based biomaterials." *Dental Materials Journal*, 28, 1-10.

Chu, T. G., Orton, D. G., Hollister, S. J., Feinberg, S. E., Halloran, J. W. (2002). "Mechanical and in vivo performance of hydroxyapatite implants with controlled architectures." *Biomaterials*, 23, 1283-1293.

- Chun-Yan, Z., Rong-Chang, Z., Cheng-Long, L., Jia-Cheng, G. (2010). "Comparison of calcium phosphate coatings on Mg--Al and Mg--Ca alloys and their corrosion behavior in Hank's solution." *Surface and Coatings Technology*, 204, 3636-3640.
- Coy A., Viejo F., Skeldon P., Thompson G. (2010). "Susceptibility of rare-earth-magnesium alloys to micro-galvanic corrosion." *Corrosion Science*, 52, 3896-3906.
- Cui, F., Yang, J., Jiao, Y., Yin, Q., Zhang, Y., Lee, I. (2008). "Calcium phosphate coating on magnesium alloy for modification of degradation behaviour." *Frontiers of Materials Science in China*, 2, 143-148.
- De Groot, K., Wolke, J., Jansen, J. (1998). "Calcium phosphate coatings for medical implants." *Proceedings of the Institution of Mechanical Engineers, Part H: Journal of Engineering in Medicine*, 212, 137-147.
- Deshpande K. B. (2011). "Numerical modeling of micro-galvanic corrosion." *Electrochimica Acta*, 56, 1737-174.
- Dickens, B., Schroeder, L., Brown, W. (1974). "Crystallographic studies of the role of Mg as a stabilizing impurity in β -Ca₃(PO₄)₂. The crystal structure of pure β -Ca₃(PO₄)₂." *Journal of Solid State Chemistry*, 10, 232-248.
- Ding, Y., Wen, C., Hodgson, P., Li, Y. (2014). "Effects of alloying elements on the corrosion behavior and biocompatibility of biodegradable magnesium alloys: a review." *Journal of Materials Chemistry B*, 2, 1912-1933.
- Dorozhkin, S. V., Epple, M. (2002). "Biological and medical significance of calcium phosphates." *Angewandte Chemie International Edition*, 41, 3130-3146.
- Drlessen, A., Klein, C, & Groot, K. (1982). "Preparation and some properties of sintered β -whitiokite" *Biomaterials*, 3, 113-116.
- Duan, H., Yan, C., Wang, F. (2007). "Growth process of plasma electrolytic oxidation films formed on magnesium alloy AZ91D in silicate solution." *Electrochimica Acta*, 52, 5002-5009.

- Dumelie, N., Benhayoune, H., Richard, D., Laurent-Maquin, D., Balossier, G. (2008). "In vitro precipitation of electrodeposited calcium-deficient hydroxyapatite coatings on Ti6Al4V substrate." *Materials Characterization*, 59, 129-133.
- Erdmann, N., Angrisani, N., Reifenrath, J., Lucas, A., Thorey, F., Bormann, D., Meyer-Lindenberg, A. (2011). "Biomechanical testing and degradation analysis of MgCa0.8 alloy screws: a comparative in vivo study in rabbits." *Acta Biomaterialia*, 7, 1421-1428.
- Feil, F., Fürbeth, W., Schütze, M. (2009). "Purely inorganic coatings based on nanoparticles for magnesium alloys." *Electrochimica Acta*, 54, 2478-2486.
- Fujishiro, Y., Yabuki, H., Kawamura, K., Sato, T., Okuwaki, A. (1993). "Preparation of needle-like hydroxyapatite by homogeneous precipitation under hydrothermal conditions." *Journal of Chemical Technology and Biotechnology*, 57, 349-353.
- Fujishiro, Y., Sato, T., Okuwaki, A. (1995). "Coating of hydroxyapatite on metal plates using thermal dissociation of calcium-EDTA chelate in phosphate solutions under hydrothermal conditions." *Journal of Materials Science: Materials in Medicine*, 6, 172-176.
- Geng, F., Tan, L., Jin, X., Yang, J., Yang, K. (2009). "The preparation, cytocompatibility, and in vitro biodegradation study of pure β -TCP on magnesium." *Journal of Materials Science: Materials in Medicine*, 20, 1149-1157.
- Ghali, E., Dietzel, W., Kainer, K. (2004). "General and localized corrosion of magnesium alloys: A critical review." *Journal of Materials Engineering and Performance*, 13, 7-23.
- Ghasemi, A., Raja, V., Blawert, C., Dietzel, W., Kainer, K. (2008). "Study of the structure and corrosion behavior of PEO coatings on AM50 magnesium alloy by electrochemical impedance spectroscopy." *Surface and Coatings Technology*, 202, 3513-3518.
- Gnedenkova, S., Khrisanfova, O., Zavidnaya, A., Sinebryukhov, S., Egorkin, V., Nistratova, M., Yerokhin, A., Matthews, A. (2010). "PEO coatings obtained on an Mg--

- Mn type alloy under unipolar and bipolar modes in silicate-containing electrolytes.” *Surface and Coatings Technology*, 204, 2316-2322.
- Gray-Munro, J., Strong, M. (2008). “The mechanism of deposition of calcium phosphate coatings from solution onto magnesium alloy AZ31.” *Journal of Biomedical Materials Research Part A*, 90, 339-350.
- Gray-Munro, J., Seguin, C., Strong, M. (2009). “Influence of surface modification on the in vitro corrosion rate of magnesium alloy AZ31.” *Journal of Biomedical Materials Research Part A*, 91, 221-230.
- Gu, X., Zheng, Y., Cheng, Y., Zhong, S., Xi, T. (2009), “In vitro corrosion and biocompatibility of binary magnesium alloys.” *Biomaterials*, 30, 484-498.
- Gu, X., Zheng, Y., Zhong, S., Xi, T., Wang, J., Wang, W. (2010). “Corrosion of, and cellular responses to Mg--Zn--Ca bulk metallic glasses.” *Biomaterials*, 31, 1093-1103.
- Gu, X., Zhou, W., Zheng, Y., Cheng, Y., Wei, S., Zhong, S., Xi, T., Chen, L. (2010). “Corrosion fatigue behaviors of two biomedical Mg alloys-AZ91D and WE43 in simulated body fluid.” *Acta Biomaterialia*, 6, 4605-4613.
- Gu, Y., Chen, C., Bandopadhyay, S., Ning, C., Zhang, Y., Guo, Y. (2012). “Corrosion mechanism and model of pulsed DC microarc oxidation treated AZ31 alloy in simulated body fluid.” *Applied Surface Science*, 258, 6116-6126.
- Gu, X., Li, S., Li, X., Fan, Y. “Magnesium based degradable biomaterials: A review.” *Frontiers of Materials Science*, 8, 200-218.
- Gunatillake, P., Mayadunne, R., Adhikari, R. (2006). “Recent developments in biodegradable synthetic polymers.” *Biotechnology Annual Review*, 12, 301-347.
- Guo, H., An, M., Xu, S., Huo, H. (2005). “Formation of oxygen bubbles and its influence on current efficiency in micro-arc oxidation process of AZ91D magnesium alloy.” *Thin Solid Films*, 485, 53-58.
- Guo, L. F., Yue, T. M., Man, H. C. (2005). “Excimer laser surface treatment of magnesium alloy WE43 for corrosion resistance improvement.” *Journal of Materials Science Letters*, 40, 3531-3.

- Guo, H., An, M., Huo, H., Xu, S., Wu, L. (2006). "Microstructure characteristic of ceramic coatings fabricated on magnesium alloys by micro-arc oxidation in alkaline silicate solutions." *Applied Surface Science*, 252, 7911-791.
- Guo, H., Su, J., Wei, J., Kong, H., Liu, C. (2009). "Biocompatibility and osteogenicity of degradable Ca-deficient hydroxyapatite scaffolds from calcium phosphate cement for bone tissue engineering." *Acta Biomaterialia*, 5, 268-278.
- Habibovic, P., Barrere, F., Blitterswijk, C. A., Groot, K., Layrolle, P. (2002). "Biomimetic hydroxyapatite coating on metal implants." *Journal of the American Ceramic Society*, 85, 517-522.
- Habibovic, P., Van der Valk, C., Van Blitterswijk, C., De Groot, K., Meijer, G. (2004). "Influence of octacalcium phosphate coating on osteoinductive properties of biomaterials." *Journal of Materials Science: Materials in Medicine*, 15, 373-380.
- Habibovic, P., Li, J., Van Der Valk, C. M., Meijer, G., Layrolle, P., Van Blitterswijk, C. A., De Groot, K. (2005). "Biological performance of uncoated and octacalcium phosphate-coated Ti6Al4V." *Biomaterials*, 26, 23-36.
- Hänzi, A., Gunde, P., Schinhammer, M., Uggowitzer, P. (2009). "On the biodegradation performance of an Mg-Y-RE alloy with various surface conditions in simulated body fluid." *Acta Biomaterialia*, 5, 162-171.
- Hartwig, A. (2001). "Role of magnesium in genomic stability." *Mutation Research/Fundamental and Molecular Mechanisms of Mutagenesis*, 475, 113-121.
- Hong, T., Nagumo, M. (1997). "Effect of surface roughness on early stages of pitting corrosion of Type 301 stainless steel." *Corrosion Science*, 39, 1665-72.
- Hong, J., Park, H. (2011). "Fabrication and characterization of block copolymer micelle multilayer films prepared using dip-, spin- and spray-assisted layer-by-layer assembly deposition." *Colloids and Surfaces A: Physicochemical and Engineering Aspects*, 381, 7-12.
- Hornberger, H., Virtanen, S., Boccaccini, A. (2012). "Biomedical coatings on magnesium alloys--A review." *Acta Biomaterialia*, 8, 2442-2455.

- Huang, Y., Min, Q., Zhang, M., Liu, H., Yang, D. (2006). "Degradation mechanisms of poly (lactic-co-glycolic acid) films in vitro under static and dynamic environment." *Transactions of Nonferrous Metals Society of China*, 16, s293-s297.
- Hwang, I., Hwang, D., Ko, Y., Shin, D. (2012). "Correlation between current frequency and electrochemical properties of Mg alloy coated by micro arc oxidation." *Surface and Coatings Technology*, 206, 3360-3365.
- Jacobs, J., Gilbert, J., Urban, R. (1998). "Current concepts review-Corrosion of metal orthopaedic implants." *The Journal of Bone and Joint Surgery*, 80, 268-282.
- Jacobs, J., Hallab, N., Skipor, A., Urban, R. (2003). "Metal degradation products: a cause for concern in metal-metal bearings?" *Clinical Orthopaedics and Related Research*, 417, 139-147.
- Jain, R. A. (2000). "The manufacturing techniques of various drug loaded biodegradable poly (lactide-co-glycolide)(PLGA) devices." *Biomaterials*, 21, 2475-2490.
- Jamesh, M., Kumar, S., Narayanan, T. S. (2012). "Electrodeposition of hydroxyapatite coating on magnesium for biomedical applications." *Journal of Coatings Technology and Research*, 9, 495-502.
- Jin, F., Chu, P. K., Xu, G., Zhao, J., Tang, D., Tong, H. (2006). "Structure and mechanical properties of magnesium alloy treated by micro-arc discharge oxidation using direct current and high-frequency bipolar pulsing modes." *Materials Science and Engineering: A*, 435, 123-12.
- Jin, S., Amira, S., Ghali, E. (2007). "Electrochemical impedance spectroscopy evaluation of the corrosion behavior of die cast and thixocast AXJ530 magnesium alloy in chloride solution." *Advanced Engineering Materials*, 9, 75-83.
- Jonášová, L., Muller, F. A., Helebrant, A., Strnad, J., Greil, P. (2004). "Biomimetic apatite formation on chemically treated titanium." *Biomaterials*, 25, 1187-1194.

Jönsson, M., Persson, D. (2010). "The influence of the microstructure on the atmospheric corrosion behaviour of magnesium alloys AZ91D and AM50." *Corrosion Science*, 52, 1077-1085.

Kalb, H., Rzany, A., Hensel, B. (2012). "Impact of Micro-Galvanic Corrosion on the Degradation Morphology of WE43 and Pure Magnesium under Exposure to Simulated Body Fluid." *Corrosion Science*, 57, 122-130.

Kannan, M. B., Dietzel, W., Blawert, C., Atrens, A., Lyon, P. (2008). "Stress corrosion cracking of rare-earth containing magnesium alloys ZE41, QE22 and Elektron 21 (EV31A) compared with AZ80." *Materials Science and Engineering: A*, 480, 529-539.

Kannan M. B., Raman, R. (2008). "In vitro degradation and mechanical integrity of calcium-containing magnesium alloys in modified-simulated body fluid." *Biomaterials*, 29, 2306-2314.

Kannan M. B. (2010). "Influence of microstructure on the in-vitro degradation behaviour of magnesium alloys." *Materials Letters*, 64, 739-742.

Kannan M. B., Singh, R. (2010). "A mechanistic study of in vitro degradation of magnesium alloy using electrochemical techniques." *Journal of Biomedical Materials Research Part A*, 93, 1050-1055.

Kannan, M. B., Orr, L. (2011). "In vitro mechanical integrity of hydroxyapatite coated magnesium alloy." *Biomedical Materials*, 6, 1-11.

Kannan, M. B. (2012). "Enhancing the performance of calcium phosphate coating on a magnesium alloy for bioimplant applications." *Materials Letters*, 76, 109-112.

Kannan M. B., Koc, E., Unal, M. (2012). "Biodegradability of β -Mg₁₇Al₁₂ phase in simulated body fluid." *Materials Letters*, 82, 54-56.

Kannan, M. B., Dietzel, W. (2012). "Pitting-induced hydrogen embrittlement of magnesium-aluminium alloy." *Materials & Design*, 42, 321-326.

Kannan, M. B., Wallipa, O. (2013). "Potentiostatic pulse-deposition of calcium phosphate on magnesium alloy for temporary implant applications-An in vitro corrosion study." *Materials Science and Engineering: C*, 33, 675-679.

- Kannan, M. B. (2013). "Improving the packing density of calcium phosphate coating on a magnesium alloy for enhanced degradation resistance." *Journal of Biomedical Materials Research Part A*, 101A, 1248-1254.
- Kim, H. (2003). "Ceramic bioactivity and related biomimetic strategy." *Current Opinion in Solid State and Materials Science*, 7, 289-299.
- Kim, K. H., Nam, N. D., Kim, J. G., Shin, K. S., Jung, H. C. (2011). "Effect of calcium addition on the corrosion behavior of Mg-5Al alloy." *Intermetallics*, 19, 1831-1838.
- Klammert, U., Reuther, T., Jahn, C., Kraski, B., Kübler, A., Gbureck, U. (2009) "Cytocompatibility of brushite and monetite cell culture scaffolds made by three-dimensional powder printing." *Acta Biomaterialia*, 5, 727-734.
- Klein, C., Patka, P., Wolke, J., de Blieck-Hogervorst, J., De Groot, K. (1994). "Long-term in vivo study of plasma-sprayed coatings on titanium alloys of tetracalcium phosphate, hydroxyapatite and α -tricalcium phosphate." *Biomaterials*, 15, 146-150.
- Koerten, H., Van der Meulen, J. (1999). "Degradation of calcium phosphate ceramics." *Journal of Biomedical Materials Research*, 44, 78-86.
- Kokubo, T., Ito, S., Huang, Z., Hayashi, T., Sakka, S., Kitsugi, T., Yamamuro, T., "Ca, P-rich layer formed on high-strength bioactive glass-ceramic A-W." *Journal of Biomedical Materials Research*, 24, 331-343.
- Kokubo, T. (1996). "Formation of biologically active bone-like apatite on metals and polymers by a biomimetic process." *Thermochimica Acta*, 280, 479-490.
- Krishna, L. R., Poshal, G., Sundararajan, G. (2010). "Influence of electrolyte chemistry on morphology and corrosion resistance of micro arc oxidation coatings deposited on magnesium." *Metallurgical and Materials Transactions A*, 41, 3499-3508.
- Krishna, L. R., Sundararajan, G. (2014). "Aqueous corrosion behavior of micro arc oxidation (MAO)-coated magnesium alloys: a critical review." *Journal of The Minerals, Metals & Materials Society*, 66, 1045-1060.

- Kumar, M., Xie, J., Chittur, K., Riley, C. (1999). "Transformation of modified brushite to hydroxyapatite in aqueous solution: effects of potassium substitution." *Biomaterials*, 20, 1389-1399.
- Kumar, M., Dasarathy, H., Riley, C. (1999a). "Electrodeposition of brushite coatings and their transformation to hydroxyapatite in aqueous solutions." *Journal of Biomedical Materials Research*, 45, 302-310.
- Kuo, M., Yen, S. (2002). "The process of electrochemical deposited hydroxyapatite coatings on biomedical titanium at room temperature." *Materials Science and Engineering: C*, 20, 153-160.
- Lee, Y., Dahle, A., StJohn, D. (2000). "The role of solute in grain refinement of magnesium." *Metallurgical and Materials Transactions A*, 31, 2895-2906.
- Lee, S., Hsu, C., Hsu, F., Chou, C., Lin, C., Weng, C. (2011). "Effects of Ni addition on hydrogen storage properties of Mg₁₇Al₁₂ alloy." *Materials Chemistry and Physics*, 126, 319-324.
- LeGeros, R., Parsons, J. R., Daculsi, G., Driessens, F., Lee, D., Liu, S., Metsger, S., Peterson, D., Walker, M. (1988). "Significance of the Porosity and Physical Chemistry of Calcium Phosphate Ceramics Biodegradation." *Bioresorption Annals of the New York Academy of Sciences*, 523, 268-271.
- Le Guéhennec, L., Soueidan, A., Layrolle, P., Amouriq, Y. (2007). "Surface treatments of titanium dental implants for rapid osseointegration." *Dental Materials*, 23, 844-854.
- Levinskas, G. J., Neuman, W. F. (1955). "The solubility of bone mineral. I. Solubility studies of synthetic hydroxylapatite." *The Journal of Physical Chemistry*, 59, 164-168.
- Li, W., Li, D. Y. (2006). "Influence of surface morphology on corrosion and electronic behaviour." *Acta Materiala*, 54, 445-52.
- Li, Z., Gu, X., Lou, S., Zheng, Y. (2008). "The development of binary Mg-Ca alloys for use as biodegradable materials within bone." *Biomaterials*, 29, 1329-1344.

- Li, J., Cao, P., Zhang, X., Zhang, S., He, Y. (2010). "In vitro degradation and cell attachment of a PLGA coated biodegradable Mg--6Zn based alloy." *Journal of Materials Science*, 45, 6038-6045.
- Liu, N., Wang, J., Wu, Y., Wang, L. (2008). "Electrochemical corrosion behavior of cast Mg--Al--RE--Mn Alloys in NaCl solution." *Journal of Materials Science*, 43, 2550-2554.
- Liu, G., Hu, J., Ding, Z., Wang, C. (2011). "Bioactive calcium phosphate coating formed on micro-arc oxidized magnesium by chemical deposition." *Applied Surface Science*, 257, 2051-2057.
- Liang, J., Guo, B., Tian, J., Liu, H., Zhou, J., Xu, T. (2005). "Effect of potassium fluoride in electrolytic solution on the structure and properties of microarc oxidation coatings on magnesium alloy." *Applied Surface Science*, 252, 345-351.
- Liang, J., Hu, L., Hao, J. (2007). "Improvement of corrosion properties of microarc oxidation coating on magnesium alloy by optimizing current density parameters." *Applied Surface Science*, 253, 6939-6945.
- Liang, J., Hu, L., Hao, J. (2007a). "Characterization of microarc oxidation coatings formed on AM60B magnesium alloy in silicate and phosphate electrolytes." *Applied Surface Science*, 253, 4490-4496.
- Liang, J., Srinivasan, P., Blawert, C., Störmer, M., Dietzel, W. (2009). "Electrochemical corrosion behaviour of plasma electrolytic oxidation coatings on AM50 magnesium alloy formed in silicate and phosphate based electrolytes." *Electrochimica Acta*, 54, 3842-3850.
- Liang, J., Srinivasan, P. B., Blawert, C., Dietzel, W. (2010). "Influence of chloride ion concentration on the electrochemical corrosion behaviour of plasma electrolytic oxidation coated AM50 magnesium alloy." *Electrochimica Acta*, 55, 6802-6811.
- Liu, Q., Ding, J., Mante, F., Wunder, S., Baran, G. (2002). "The role of surface functional groups in calcium phosphate nucleation on titanium foil: a self-assembled monolayer technique." *Biomaterials*, 23, 3103-3111.

Liu, C., Xin, Y., Tang, G., Chu, P. (2007). "Influence of heat treatment on degradation behavior of bio-degradable die-cast AZ63 magnesium alloy in simulated body fluid." *Materials Science and Engineering: A*, 456, 350-357.

Liu, Y., Wang, Q., Song, Y., Zhang, D., Yu, S., Zhu, X. (2009). "A study on the corrosion behavior of Ce-modified cast AZ91 magnesium alloy in the presence of sulfate-reducing bacteria." *Journal of Alloys and Compounds*, 473, 550-556.

Liu, M., Uggowitzer, P. J., Nagasekhar, A., Schmutz, P., Easton, M., Song, G., Atrens, A. (2009a). "Calculated phase diagrams and the corrosion of die-cast Mg--Al alloys." *Corrosion Science*, 51, 602-619.

Lunt, J. (1998). "Large-scale production, properties and commercial applications of polylactic acid polymers." *Polymer Degradation and Stability*, 59, 145-152.

Luo, H., Cai, Q., Wei, B., Yu, B., Li, D., He, J., Liu, Z. (2008). "Effect of $(\text{NaPO}_3)_6$ concentrations on corrosion resistance of plasma electrolytic oxidation coatings formed on AZ91D magnesium alloy." *Journal of Alloys and Compounds*, 464, 537-543.

Makar, G. L., Kruger, J. (1993). "Corrosion of magnesium." *International Materials Reviews*, 38, 138-53.

Manso, M., Jimenez, C., Morant, C., Herrero, P., Martinez-Duart, J. (2000). "Electrodeposition of hydroxyapatite coatings in basic conditions." *Biomaterials*, 21, 1755-1761.

Mathieu, S., Rapin, C., Steinmetz, J., Steinmetz, P. A. (2003). "A corrosion study of the main constituent phases of AZ91 magnesium alloys." *Corrosion Science*, 45, 2741-2755.

Maurus, P. B., Kaeding, C. C. (2004). "Bioabsorbable implant material review." *Operative Techniques in Sports Medicine*, 12, 158-160.

McCafferty, E. (2003). "Sequence of steps in the pitting of aluminum by chloride ions." *Corrosion Science*, 45, 1421-1438.

Middleton, J. C., Tipton, A. J. (2000). "Synthetic biodegradable polymers as orthopedic devices." *Biomaterials*, 21, 2335-2346.

- Mihailescu, I., Torricelli, P., Bigi, A., Mayer, I., Iliescu, M., Werckmann, J., Socol, G., Miroiu, F., Cuisinier, F., Elkaim, R., ... Hildebrand, G. (2005). "Calcium phosphate thin films synthesized by pulsed laser deposition: Physico-chemical characterization and in vitro cell response." *Applied Surface Science*, 248, 344-348.
- Miller, R. A., Brady, J. M., Cutright, D. E. (1977). "Degradation rates of oral resorbable implants (polylactates and polyglycolates): rate modification with changes in PLA/PGA copolymer ratios." *Journal of Biomedical Materials Research*, 11, 711-719.
- Nagels, J., Stokdijk, M., Rozing, P. (2003). "Stress shielding and bone resorption in shoulder arthroplasty." *Journal of Shoulder and Elbow Surgery*, 12, 35-39.
- Nair, L. S., Laurencin, C. T. (2007). "Biodegradable polymers as biomaterials." *Progress in Polymer Science*, 32, 762-798.
- Nakatsugawa, I., Takayasu, H., Araki, K., Tsukeda, T. (2003). "Electrochemical corrosion studies of thixomolded AZ91D alloy in sodium chloride solution." *Materials Science Forum*, 419, 845-850.
- Nam, N., Kim, W., Kim, J., Shin, K., Jung, H. (2011). "Corrosion resistance of Mg--5Al--xSr alloys." *Journal of Alloys and Compounds*, 509, 4839-4847.
- Nam, N. D., Mathesh, M., Forsyth, M., Jo, D. S. (2012). "Effect of manganese additions on the corrosion behavior of an extruded Mg--5Al based alloy." *Journal of Alloys and Compounds*, 542, 199-206.
- Narayanan, R., Seshadri, S., Kwon, T., Kim, K. (2008). "Calcium phosphate-based coatings on titanium and its alloys." *Journal of Biomedical Materials Research Part B: Applied Biomaterials*, 85, 279-299.
- Niki, Y., Matsumoto, H., Suda, Y., Otani, T., Fujikawa, K., Toyama, Y., Hisamori, N., Nozue, A. (2003). "Metal ions induce bone-resorbing cytokine production through the redox pathway in synoviocytes and bone marrow macrophages." *Biomaterials*, 24, 1447-1457.
- Ohtsu, N., Hiromoto, S., Yamane, M., Satoh, K., Tomozawa, M. (2013). "Chemical and crystallographic characterizations of hydroxyapatite-and octacalcium phosphate-

coatings on magnesium synthesized by chemical solution deposition using XPS and XRD.” *Surface and Coatings Technology*, 218, 114-118.

Okuma, T. (2001). “Magnesium and bone strength.” *Nutrition*, 17, 679-680.

Ong, J., Lucas, L., Lacefield, W., Rigney, E. (1992). “Structure, solubility and bond strength of thin calcium phosphate coatings produced by ion beam sputter deposition.” *Biomaterials*, 13, 249-254.

Ostrowski, N. J., Lee, B., Roy, A., Ramanathan, M., Kumta, P. N. (2013). “Biodegradable poly (lactide-co-glycolide) coatings on magnesium alloys for orthopedic applications.” *Journal of Materials Science: Materials in Medicine*, 24, 85-96.

Oyane, A., Kim, H., Furuya, T., Kokubo, T., Miyazaki, T., Nakamura, T. (2003). “Preparation and assessment of revised simulated body fluids.” *Journal of Biomedical Materials Research Part A*, 65, 188-195.

Pardo, A., Merino, M., Coy, A., Arrabal, R., Viejo, F., Matykina, E. (2008). “Corrosion behaviour of magnesium/aluminium alloys in 3.5 wt. % NaCl.” *Corrosion Science*, 50, 823-834.

Pecheva, E. V., Pramatarova, L. D., Maitz, M. F., Pham, M. T., Kondyuirin, A. V. (2004). “Kinetics of hydroxyapatite deposition on solid substrates modified by sequential implantation of Ca and P ions: Part I. FTIR and Raman spectroscopy study.” *Applied Surface Science*, 235, 176-181.

Peppas, N., Huang, Y., Torres-Lugo, M., Ward, J., Zhang, J. (2000). “Physicochemical foundations and structural design of hydrogels in medicine and biology.” *Annual Review of Biomedical Engineering*, 2, 9-29.

Pramatarova, L., Pecheva, E., Presker, R., Pham, M. T., Maitz, M. F., Stutzmann, M., *European Cells Materials*, 9, 9-12.

Qiao, Z., Shi, Z., Hort, N., Abidin, N. I. Z., Atrens, A. Corrosion behaviour of a nominally high purity Mg ingot produced by permanent mould direct chill casting.” *Corrosion Science*, 61, 185-207.

- Qu, H., Wei, M. (2008). "The effect of temperature and initial pH on biomimetic apatite coating." *Journal of Biomedical Material Research B: Applied Biomaterials*, 87, 204-212.
- Rad, H., Idris, M., Kadir, M., Farahany, S. (2012). "Microstructure analysis and corrosion behavior of biodegradable Mg-Ca implant alloys." *Materials & Design*, 33, 88-97.
- Redepenning, J., Schlessinger, T., Burnham, S., Lippiello, L., Miyano, J. (1996). "Characterization of electrolytically prepared brushite and hydroxyapatite coatings on orthopedic alloys." *Journal of Biomedical Materials Research*, 30, 287-294.
- Reiner, T., Gotman, I. (2010). "Biomimetic calcium phosphate coating on Ti wires versus flat substrates: structure and mechanism of formation." *Journal of Materials Science: Materials in Medicine*, 21, 515-523.
- Rettig, R., Virtanen, S. (2009). "Composition of corrosion layers on a magnesium rare-earth alloy in simulated body fluids." *Journal of Biomedical Materials Research Part A*, 88, 359-369.
- Rosalbino, F., Angelini, E., De Negri, S., Saccone, A., Delfino, S. (2005). "Effect of erbium addition on the corrosion behaviour of Mg-Al alloys." *Intermetallics*, 13, 55-60.
- Rosalbino, F., Angelini, E., De Negri, S., Saccone, A., Delfino, S. (2006). "Electrochemical behaviour assessment of novel Mg-rich Mg-Al-RE alloys (RE= Ce, Er)." *Intermetallics*, 14, 1487-1492.
- Rosalbino, F., De Negri, S., Saccone, A., Angelini, E., Delfino, S. (2010). "Bio-corrosion characterization of Mg-Zn-X (X= Ca, Mn, Si) alloys for biomedical applications." *Journal of Materials Science: Materials in Medicine*, 21, 1091-1098.
- Roy, A., Singh, S. S., Datta, M. K., Lee, B., Ohodnicki, J., Kumta, P. N. (2011). "Novel sol-gel derived calcium phosphate coatings on Mg4Y alloy." *Materials Science and Engineering: B*, 176, 1679-1689.

Sanchez, C., Nussbaum, G., Azavant, P., Octor, H. (1996). "Elevated temperature behaviour of rapidly solidified magnesium alloys containing rare earths." *Materials Science and Engineering: A*, 221, 48-57.

Sandeman, S. R., Jeffery, H., Howell, C. A., Smith, M., Mikhalovsky, S. V., Lloyd, A. W. (2009). "The in vitro corneal biocompatibility of hydroxyapatite coated carbon mesh." *Biomaterials*, 30, 3143-3149.

Saris, N., Mervaala, E., Karppanen, H., Khawaja, J., Lewenstam, A. (2000). "Magnesium: An update on physiological, clinical and analytical aspects." *Clinica Chimica Acta*, 294, 1-26.

Sasaki, K., Burstein, G. T. (1996). "The generation of surface roughness during slurry erosion-corrosion and its effect on the pitting potential." *Corrosion Science*, 38, 2111-20.

Shadanbaz, S., Dias, G. J. (2012). "Calcium phosphate coatings on magnesium alloys for biomedical applications: a review." *Acta Biomaterialia*, 8, 20-30.

Shadanbaz, S., Walker, J., Staiger, M. P., Dias, G. J., Pietak, A. (2013). "Growth of calcium phosphates on magnesium substrates for corrosion control in biomedical applications via immersion techniques." *Journal of Biomedical Materials Research Part B: Applied Biomaterials*, 101, 162-172.

Shahryari, A., Kamal, W., Omanovic, S. (2008). "The effect of surface roughness on the efficiency of the cyclic potentiodynamic passivation (CPP) method in the improvement of general and pitting corrosion resistance of 316LVM stainless steel." *Materials Letters*, 62, 3906-9.

Shelton, R., Liu, Y., Cooper, P., Gbureck, U., German, M., Barralet, J. (2006). "Bone marrow cell gene expression and tissue construct assembly using octacalcium phosphate microscaffolds." *Biomaterials*, 27, 2874-2881.

Sivakumar, G., Girija, E., Narayana Kalkura, S., Subramanian, C. (1998). "Crystallization and characterization of calcium phosphates: brushite and monetite." *Crystal Research and Technology*, 33, 197-205.

- Socol, G., Torricelli, P., Bracci, B., Iliescu, M., Miroiu, F., Bigi, A., Werckmann, J., Mihailescu, I. (2004). "Biocompatible nanocrystalline octacalcium phosphate thin films obtained by pulsed laser deposition." *Biomaterials*, 25, 2539-2545.
- Song, G., Atrens, A., Wu, X., Zhang, B. (1998). "Corrosion behaviour of AZ21, AZ501 and AZ91 in sodium chloride." *Corrosion Science*, 40, 1769-179.
- Song, G., Atrens, A. (1999). "Corrosion mechanisms of magnesium alloys." *Advanced Engineering Materials*, 1, 11-33.
- Song, G., Atrens, A., Dargusch, M. (1999). "Influence of microstructure on the corrosion of diecast AZ91D." *Corrosion Science*, 41, 249-273.
- Song, G., Atrens, A. (2003). "Understanding magnesium corrosion - a framework for improved alloy performance." *Advanced Engineering Materials*, 5, 837-858.
- Song, G., Atrens, A. (2007). "Recent insights into the mechanism of magnesium corrosion and research suggestions." *Advanced Engineering Materials*, 9, 177-183.
- Song, Y., Shan, D., Han, E. (2008). "Electrodeposition of hydroxyapatite coating on AZ91D magnesium alloy for biomaterial application." *Materials Letters*, 62, 3276-327.
- Song, Y., Liu, Y., Yu, S., Zhu, X., Wang, Q. (2008). "Plasma electrolytic oxidation coating on AZ91 magnesium alloy modified by neodymium and its corrosion resistance." *Applied Surface Science*, 254, 3014-3020.
- Song, Y., Shan, D., Chen, R., Zhang, F., Han, E. (2009). "Biodegradable behaviors of AZ31 magnesium alloy in simulated body fluid." *Materials Science and Engineering C*, 29, 1039-1045.
- Song, Y., Zhang, S., Li, J., Zhao, C., Zhang, X. (2010). "Electrodeposition of Ca--P coatings on biodegradable Mg alloy: in vitro biomineralization behaviour." *Acta Biomaterialia*, 6, 1736-1742.
- Song, Y., Han, E., Shan, D., Yim, C. D., You, B. S. (2012). "The role of second phases in the corrosion behavior of Mg--5Zn alloy." *Corrosion Science*, 60, 238-245.

- Song, Y., Han, E. H., Shan, D., Yim, C. D., You, B. S. (2012). "The effect of Zn concentration on the corrosion behavior of Mg-xZn alloys." *Corrosion Science*, 65, 322-330.
- Staiger, M., Pietak, A., Huadmai, J., Dias, G. (2006). "Magnesium and its alloys as orthopedic biomaterials: A review." *Biomaterials*, 27, 1728-173.
- Strates, B. S., Neuman, W., Levinskas, G. J. (1957). "The Solubility of Bone Mineral. II. Precipitation of Near-Neutral Solutions of Calcium and Phosphate." *The Journal of Physical Chemistry*, 61, 279-282.
- Srinivasan, P. B., Liang, J., Blawert, C., Störmer, M., Dietzel, W. (2009). "Effect of current density on the microstructure and corrosion behaviour of plasma electrolytic oxidation treated AM50 magnesium alloy." *Applied Surface Science*, 255, 4212-4218.
- Srinivasan, P. B., Liang, J., Blawert, C., Störmer, M., Dietzel, W. (2010). "Characterization of calcium containing plasma electrolytic oxidation coatings on AM50 magnesium alloy." *Applied Surface Science*, 256, 4017-4022.
- Srinivasan, P., Scharnagl, N., Blawert, C., Dietzel, W. (2010). "Enhanced corrosion protection of AZ31 magnesium alloy by duplex plasma electrolytic oxidation and polymer coatings." *Surface Engineering*, 26, 354-360.
- Štulajterová, R., Medveck, L. (2008). "Effect of calcium ions on transformation brushite to hydroxyapatite in aqueous solutions." *Colloids and Surfaces A: Physicochemical and Engineering Aspects*, 316, 104-109.
- Sun, Y., Zhang, B., Wang, Y., Geng, L., Jiao, X. (2011). "Preparation and characterization of a new biomedical Mg-Zn-Ca alloy." *Materials and Design*, 34, 58-64.
- Sun, Y., Kong, M., Jiao, X. (2011). "In-vitro evaluation of Mg-4.0 Zn-0.2 Ca alloy for biomedical application." *Transactions of Nonferrous Metals Society*, 21, s252-s257.
- Sun, T., Wang, Z., Li, J., Zhang, T., "Effect of ultrasonic vibration solidification treatment on the corrosion behavior of AZ80 magnesium alloy." *International Journal of Electrochemical Science*, 8, 7298-7319.

- Sundararajan, G., Krishna, L. R. (2003). "Mechanisms underlying the formation of thick alumina coatings through the MAO coating technology." *Surface and Coatings Technology*, 167, 269-277.
- Tamai, N., Myoui, A., Tomita, T., Nakase, T., Tanaka, J., Ochi, T., Yoshikawa, H. (2002). "Novel hydroxyapatite ceramics with an interconnective porous structure exhibit superior osteoconduction in vivo." *Journal of Biomedical Materials Research*, 59, 110-117.
- TenHuisen, K. S., Brown, P. W. (1998). "Formation of calcium-deficient hydroxyapatite from α -tricalcium phosphate." *Biomaterials*, 19, 2209-2217.
- Tie, D., Feyerabend, F., Hort, N., Willumeit, R., Hoeche, D. (2010). "XPS studies of magnesium surfaces after exposure to Dulbecco's modified eagle medium, Hank's buffered salt solution, and simulated body fluid." *Advanced Engineering Materials*, 12, B699-B704.
- Timoshenko, A., Magurova, Y. V. (2005). "Investigation of plasma electrolytic oxidation processes of magnesium alloy MA2-1 under pulse polarisation modes." *Surface and Coatings Technology*, 199, 135-140.
- Tsui, Y., Doyle, C., Clyne, T. (1998). "Plasma sprayed hydroxyapatite coatings on titanium substrates Part 1: Mechanical properties and residual stress levels." *Biomaterials*, 19, 2015-2029.
- Viswanath, B., Raghavan, R., Gurao, N., Ramamurty, U., Ravishankar, N. (2008). "Mechanical properties of tricalcium phosphate single crystals grown by molten salt synthesis." *Acta Biomaterialia*, 4, 1448-1454.
- Vormann, Jü. (2003). "Magnesium: nutrition and metabolism." *Molecular Aspects of Medicine*, 24, 27-37.
- Walter, R., Kannan, M. B. (2011). "In-vitro degradation behaviour of WE54 magnesium alloy in simulated body fluid." *Materials Letters*, 65, 748-750.

- Walsh, F., Low, C., Wood, R., Stevens, K., Archer, J., Poeton, A., Ryder, A. (2009). "Plasma electrolytic oxidation (PEO) for production of anodised coatings on lightweight metal (Al, Mg, Ti) alloys." *Transactions of the IMF*, 87, 122-135.
- Wan, Y., Xiong, G., Luo, H., He, F., Huang, Y., Zhou, X. (2008). "Preparation and characterization of a new biomedical magnesium--calcium alloy." *Materials and Design*, 29, 2034-2037.
- Wang, J. Y., Wicklund, B. H., Gustilo, R. B., Tsukayama, D. T. (1996). "Titanium, chromium and cobalt ions modulate the release of bone-associated cytokines by human monocytes/macrophages in vitro." *Biomaterials*, 17, 2233-2240.
- Wang, Y., Wei, M., Gao, J., Hu, J., Zhang, Y. (2008). "Corrosion process of pure magnesium in simulated body fluid." *Materials Letters*, 62, 2181-2184.
- Wang, H., Guan, S., Wang, X., Ren, C., Wang, L. (2010). "In vitro degradation and mechanical integrity of Mg-Zn-Ca alloy coated with Ca-deficient hydroxyapatite by the pulse electrodeposition process." *Acta Biomaterialia*, 6, 1743-1748.
- Waterman, J, Pietak, A., Birbilis, N., Woodfield, T., Dias, G., Staiger, M. (2011). "Corrosion resistance of biomimetic calcium phosphate coatings on magnesium due to varying pretreatment time." *Materials Science and Engineering: B*, 176, 1756-1760.
- Wen, Z., Wu, C., Dai, C., Yang, F. (2009). "Corrosion behaviors of Mg and its alloys with different Al contents in a modified simulated body fluid." *Journal of Alloys and Compounds*, 488, 392-399.
- Winzer, N., Atrens, A., Song, G., Ghali, E., Dietzel, W., Kainer, K., Hort, N., Blawert, C. (2005). "A critical review of the stress corrosion cracking (SCC) of magnesium alloys." *Advanced Engineering Materials*, 7, 659-693.
- Winzer, N., Atrens, A., Dietzel, W., Song, G., Kainer, K. (2007). "Evaluation of the delayed hydride cracking mechanism for transgranular stress corrosion cracking of magnesium alloys." *Materials Science and Engineering: A*, 466, 18-31.

- Witte, F., Kaese, V., Haferkamp, H., Switzer, E., Meyer-Lindenberg, A., Wirth, C., Windhagen, H. (2005). "In vivo corrosion of four magnesium alloys and the associated bone response." *Biomaterials*, 26, 3557-3563.
- Witte, F., Fischer, J., Nellesen, J., Crostack, H., Kaese, V., Pisch, A., Beckmann, F., Windhagen, H. (2006). "In vitro and in vivo corrosion measurements of magnesium alloys." *Biomaterials*, 27, 1013-1018.
- Witte, F., Hort, N., Vogt, C., Cohen, S., Kainer, K., Willumeit, R., Feyerabend, F. (2008). "Degradable biomaterials based on magnesium corrosion." *Current Opinion in Solid State and Materials Science*, 12, 63-72.
- Witte, F. (2010). "The history of biodegradable magnesium implants: a review." *Acta Biomaterialia*, 6, 1680-1692.
- Wu, L., Ding, J. (2004). "In vitro degradation of three-dimensional porous poly (D, L-lactide-co-glycolide) scaffolds for tissue engineering." *Biomaterials*, 25, 5821-5830.
- Xie, J., Riley, C., Chittur, K. (2001). "Effect of albumin on brushite transformation to hydroxyapatite." *Journal of Biomedical Materials Research*, 57, 357-36.
- Xin, Y., Liu, C., Zhang, X., Tang, G., Tian, X., Chu, P. K. (2007). "Corrosion behavior of biomedical AZ91 magnesium alloy in simulated body fluids." *Journal of Materials Research*, 22, 2004-2011.
- Xu, L., Pan, F., Yu, G., Yang, L., Zhang, E., Yang, K. (2009). "In vitro and in vivo evaluation of the surface bioactivity of a calcium phosphate coated magnesium alloy." *Biomaterials*, 30, 1512-1523.
- Xu, L., Yamamoto, A. (2012). "Characteristics and cytocompatibility of biodegradable polymer film on magnesium by spin coating." *Colloids and Surfaces B: Biointerfaces*, 93, 67-74.
- Yamada, S., Heymann, D., Bouler, J., Daculsi, G. (1997). "Osteoclastic resorption of calcium phosphate ceramics with different hydroxyapatite/ β -tricalcium phosphate ratios." *Biomaterials*, 18, 1037-1041.

- Yang, Y., Kim, K., Ong, J. L. (2005). "A review on calcium phosphate coatings produced using a sputtering process—an alternative to plasma spraying." *Biomaterials*, 26, 327-337.
- Yerokhin, A.; Nie, X.; Leyland, A.; Matthews, A. & Dowey, S. Plasma electrolysis for surface engineering *Surface and Coatings Technology*, Elsevier, 1999, 122, 73-93
- Zhang, X., Wyss, U. P., Pichora, D., Goosen, M. F. (1994). "An investigation of poly (lactic acid) degradation." *Journal of Bioactive and Compatible Polymers*, 9, 80-100.
- Zhang, Y., Yan, C., Wang, F., Li, W. (2005). "Electrochemical behavior of anodized Mg alloy AZ91D in chloride containing aqueous solution." *Corrosion Science*, 47, 2816-2831.
- Zhang, T., Li, Y., Wang, F. (2006) Roles of β phase in the corrosion process of AZ91D magnesium alloy." *Corrosion Science*, 48, 1249-1264.
- Zhang, E., Yin, D., Xu, L., Yang, L., Yang, K. (2009). "Microstructure, mechanical and corrosion properties and biocompatibility of Mg-Zn-Mn alloys for biomedical application." *Materials Science and Engineering: C*, 29, 987-993.
- Zhang, Y., Zhang, G., Wei, M. (2009). "Controlling the biodegradation rate of magnesium using biomimetic apatite coating." *Journal of Biomedical Materials Research Part B*, 89: 408-414.
- Zhang, E., Yang, L., Xu, J., Chen, H. (2010). "Microstructure, mechanical properties and bio-corrosion properties of Mg-Si (-Ca, Zn) alloy for biomedical application." *Acta Biomaterialia*, 6, 1756-1762.
- Zhang, X., Yuan, G., Mao, L., Niu, J., Ding, W. (2012). "Biocorrosion properties of as-extruded Mg-Nd-Zn-Zr alloy compared with commercial AZ31 and WE43 alloys." *Materials Letters*, 66, 209-211.
- Zhang, W., Li, M., Chen, Q., Hu, W., Zhang, W., Xin, W. (2012). "Effects of Sr and Sn on microstructure and corrosion resistance of Mg-Zr-Ca magnesium alloy for biomedical applications." *Materials and Design*, 39, 379-383.

Zhao, M., Liu, M., Song, G., Atrens, A. (2008). "Influence of the β -phase morphology on the corrosion of the Mg alloy AZ91." *Corrosion Science*, 50, 1939-1953.

Zhou, W., Shen, T., Aung, N. (2010). "Effect of heat treatment on corrosion behaviour of magnesium alloy AZ91D in simulated body fluid." *Corrosion Science*, 52, 1035-1041.

Zong, Y., Yuan, G., Zhang, X., Mao, L., Niu, J., Ding, W. (2012). "Comparison of biodegradable behaviors of AZ31 and Mg-Nd-Zn-Zr alloys in Hank's physiological solution." *Materials Science and Engineering: B*, 177, 395-401.

Zucchi, F., Grassi, V., Frignani, A., Monticelli, C., Trabanelli, G. (2006). "Electrochemical behaviour of a magnesium alloy containing rare earth elements." *Journal of Applied Electrochemistry*, 36, 195-204.

Zuo, Y., Wang, H., Xiong, J. (2002). "The aspect ratio of surface grooves and metastable pitting of stainless steel." *Corrosion Science*, 44, 25-35.